8-2021

Constraining Deformation Mechanisms of Fault Damage Zones: A Case Study of the Shallow San Andreas Fault at Elizabeth Lake, Southern California.

Caroline Studnicky
Utah State University

CONSTRAINING DEFORMATION MECHANISMS OF FAULT DAMAGE ZONES: A CASE STUDY OF THE SHALLOW SAN ANDREAS FAULT AT ELIZABETH LAKE, SOUTHERN CALIFORNIA.

by

Caroline Studnicky

A thesis submitted in partial fulfillment
of the requirements for the degree

of

MASTER OF SCIENCE

in

Geology

Approved:

_____	_____
James Evans, Ph.D Major Professor	Alexis Ault, Ph.D Committee Member
_____	_____
Tamara Jeppson, Ph.D Committee Member	D. Richard Cutler, Ph.D Interim Vice Provost of Graduate Studies

UTAH STATE UNIVERSITY
Logan, Utah

2021

ABSTRACT

Constraining Deformation Mechanisms of Fault Damage Zones: A Case Study of the Shallow San Andreas Fault at Elizabeth Lake, Southern California.

by

Caroline Studnicky, Master of Science

Utah State University, 2021

Major Professor: Dr. Jim Evans
Department: Geosciences

We performed macroscopic, optical petrographic, scanning electron microscopy, and geochemical analyses on rock core acquired across the San Andreas Fault at Elizabeth Lake, California, in order to understand the distribution and accommodation of fault-related slip and energy within the shallow damage zone of this continental scale strike-slip fault. We characterized the deformation structures, alteration textures, and elemental variabilities to constrain the properties of the uppermost ~2 km fault-related damage zone at this site. We identified evidence for coseismic slip in the form of pulverized rocks, injection veins, clay-clast aggregates, and pseudotachylyte, and aseismic slip through calcite twins, dilatant vein fills, and possibly by a network of aligned chlorite, biotite, and muscovite cleavages. Alteration assemblages indicate a temperature range of ~50-250°C with calcite, zeolite, chlorite, and pseudomorphic plagioclase as the most common mineral alterations. The geochemical data do not exhibit trends as a function of distance from the fault core but pointed to distinct

geochemical signatures for fault-rock types including the Si-rich pulverized rocks and a relative enrichment in the fault gouge Fe concentrations as compared to the quartzo-feldspathic protolith. The cross-cutting relationships of deformation microstructures and the distribution of the observed deformation and alteration textures indicate that coseismic and aseismic slip mechanisms are active throughout the shallow fault zone at this site. We document brittle-plastic cross cutting relationships within thin sections indicating that the slip mechanisms vary in their nature and style over multiple earthquake cycles. We show that the fault zone at Elizabeth Lake consists of a complex of superimposed fault strands that recycle and rework fault-related products and likely distribute the seismically generated energy throughout the damage zone through a combination of brittle and semi-brittle processes, and geochemical alterations. The observed deformation and alteration textures decrease the seismic velocities and reduce the overall rheologic strength of the fault-related rocks, and likely enable seismically radiated energy to be distributed throughout the fault damage zone. The distribution, nature, and degree of deformation and alteration found here may help explain how fault-related low-velocity zones form, and characterize the rocks within which shallow co-seismic slip deficits, if real, may develop.

(125 pages)

PUBLIC ABSTRACT

Constraining Deformation Mechanisms of Fault Damage Zones: A Case Study of the Shallow San Andreas Fault at Elizabeth Lake, Southern California.

Caroline Studnicky

Earthquakes nucleate at depth and rupture along the fault plane up to the Earth's surface releasing seismic energy as the fault propagates. This energy creates the shaking we feel on the surface. Some faults do not rupture and create shaking but deform slowly and smoothly accommodating fault slip over extended time periods. This process is referred to as aseismic slip or creep. Whether a fault ruptures or creeps depends on the properties of the rocks through which the fault plane extends. In order to model seismic hazards correctly, we need to characterize the composition, deformation structures, and alteration materials of the fault-related rocks. In this project, we analyze rocks which have experienced deformation and alteration in the uppermost 2 km of the Earth's crust along the San Andreas Fault at Elizabeth Lake, CA. We investigate the mechanisms which facilitate slip and energy distribution and accommodation within the fault-related damage zone in order to understand how the upper crust responds to deformation events. We identify deformation structures which indicate that slip is accommodated by both earthquake rupture and aseismic creep processes. The alteration we observe in these rocks provide evidence for fluid-assisted processes which serve to decrease the overall rock strength over multiple earthquake cycles, partially heal the damage structures between deformation events, and accommodate some aseismic fault displacement. From our data, we conclude that the rocks within the San Andreas Fault upper damage zone at Elizabeth Lake, CA are distributing deformation throughout the damage zone via a complex of multiple

fault strands and microscopic-slip events within the entire volume of impacted rock. We find that most of the fault motion is likely accommodated by brittle rupture mechanisms but also has a component of aseismic slip which may function concurrently over multiple deformation events. Our characterization of the fault damage zone will help to improve seismic modelling, may help to explain the formation of fault-zone low seismic velocities, and describes the upper fault zone structure's distribution of energy as voluminous, rather than purely localized deformation.

ACKNOWLEDGMENTS

Thank you to everyone who has supported me over the past three years as I pursued my masters and worked on this project. To Jim Evans, thank you so much for giving me the opportunity to come to USU and for being in my corner throughout this entire process. You always encouraged me to make this project my own, to take it down the path that most interested me, and to reach out to those who could contribute insight and help me push this work further. To my committee, Alexis Ault and Tamara Jeppson, thank you for the conversations that led to more questions, the edits that made me clarify and strengthen my ideas, and for providing your perspectives to this work. I truly appreciate you both. To my unofficial committee, Christie Rowe and Randy Williams, this project would not be what it is without your continued collaboration, support, and insights. You both helped me keep my head on my shoulders and brought new ideas and techniques to this project.

I would like to acknowledge the contributions of the Los Angeles Department of Water and Power including Chris Heron and James Chestnut, Scott Lindvall of Lettis Consultants, Scott Kerwin of AMECFosterWheeler, Kate Scharer of the USGS, and Skadi Kobe, Chris Ballard, and Sarah Wigginton for assistance with sample collection and preparation.

Thank you to everyone I have had the opportunity to meet and interact with at Utah State University and within the Geoscience Department, to the friends I made and those I met during my time at McGill University, and to the friends I made and the mentors I gained through my internships with Chevron Corp.

I would like to give a special thank you to the organizations that provided the funding, which made this project possible: Fonds du Recherche Nature et Technologies – International Research Internship Grant Fall 2019; Geological Society of America – Continental Scientific

Drilling Division Grant Spring 2019; Geological Society of America – Graduate Student Research Grant 2020; Utah State University – J. Stewart Williams Graduate Fellowship Spring 2019 and Summit Scholarship Spring 2020; Association of Women Geologists – Salt Lake Chapter Research Grant Winter 2019; National Science Foundation grant #EAR-1824852; and the Southern California Earthquake Center Grant #18077.

CONTENTS

LIST OF TABLES

LIST OF FIGURES

1. INTRODUCTION

Earthquakes within the continental strike-slip margin of southern California nucleate at depths of ~3-15 km (Hauksson and Meier, 2019) and the resulting slip and energy propagate to the surface through seismic and aseismic mechanisms (Marone and Saffer, 2007). The earthquake cycle is the repeated rupture of a fault segment over time (Scholz, 2019) and this cycle encompasses three main rate-phases: coseismic slip, aseismic slip, and post-seismic healing. Faults may experience a combination of different slip mechanisms over both their depth extents and their active lifespans (Sibson, 1986; Chester et al., 1993; Holdsworth, 2004). Coseismic slip and aseismic creep are end members of the range of velocity driven slip behavior on faults (Harris and Abrahamson, 2014; Bürgmann, 2018; Jolivet and Frank, 2020). Coseismic, brittle rupture dominates the cool upper crust to form faults and fractures and creates the radiated energy that we feel as earthquakes (Scholz, 2019). The interseismic period may refer to both fault healing and the aseismic processes of afterslip and/or interseismic creep (Marone et al., 1991, Roten et al., 2017). Aseismic slip, or creep, processes may span the entirely of the earthquake cycle. The velocity of aseismic slip is approximately $\leq 10^{-10}$ m/s (Rowe and Griffith, 2015), but is also more broadly classified as a deformation event that is not observed by humans at the surface (Kamei et al., 2015). Creep has been documented on the San Andreas Fault (SAF) as early as the mid-1950s (Steinbrugge and Zacher, 1960) and functions above and below the brittle seismic zone, in both steady state and episodic manners, and temporally as a component of pre-seismic, co-seismic and post-seismic events (Sylvester, 1988; Fialko et al., 2005). It is believed to be controlled by differences in host rock composition, fault zone geometry, or the effective stress regime (Ryder and Bürgmann, 2008). The behavior of creep is highly variable in

terms of depth, occurrence, and timing and its mechanisms continue to be studied today (Collettini et. al., 2009; Schleicher et. al., 2010, 2012; Lockner et. al., 2011).

Understanding the distribution of energy within a fault zone has major implications for determining how earthquake-related slip is accommodated, how earthquake rupture propagation occurs, and how seismic energy is radiated away from a fault versus consumed within a fault zone. The seismic energy released during an earthquake may be localized around a main fault strand or be distributed among multiple slip surfaces within fault damage zones. The manner and timing of slip accommodation impact the total energy reaching, rupturing, and shaking the surface. Recent studies have identified a shallow slip deficit, which suggests that earthquakes achieve a maximum coseismic slip at depths of ~3-5 km with decreasing slip propagating towards the surface (Fialko et al., 2005; Kaneko and Fialko, 2011; Dolan and Haravitch, 2014). Without uniform motion over the range of the fault zone, we suggest the shallow crust may be recovering this slip deficit through both coseismic and aseismic deformation mechanisms. Some researchers question if the deficit is real or an artifact of flawed inversions due to model simplifications (Marchandon et al., 2021), however detailed characterizations of the deformation structures and alteration textures provide the opportunity for improved modeling results.

We characterize fault-related deformation and alteration in the shallow SAF at Elizabeth Lake, California to evaluate how coseismic and aseismic slip are accommodated in the fault zone. We consider the possibility that slip is variable throughout the upper crust and differences reflect disparate deformation mechanisms, rheologies, and/or hydrothermally induced alteration within fault-related rocks. These processes may lead to the formation of an upper crustal, seismic-aseismic transition and be preserved in the rock record of fault zones (Marone

and Saffer, 2007). To accomplish this, we examine the relationship between meso- and microscale structural textures and deformation mechanisms, and whole-rock mineralogy and geochemistry of rocks acquired from a geotechnical investigation of the SAF. This segment of the SAF experienced over 5 Myr of fault activity, and thus the damage zone at this locality contains evidence for a complex reworking of previously damaged, altered, and healed fault-rocks. The deformation and alteration textures we identify result from multiple earthquake cycles that have progressively changed the rheologic properties of the fault zone over time.

2. BACKGROUND

2.1 Geologic Setting

2.1.1 The San Andreas Fault

The SAF extends from the Gulf of California to the Mendocino triple junction as a large, right-lateral transform fault marking the boundary between the Pacific and the North American plates (Wallace, 1990). A major rupture on this fault has huge societal implications as millions of people will be affected with over 1,800 deaths, 50,000 injuries, and over $200 billion of economic losses estimated (Jones et al., 2008). Understanding the rupture behavior in the upper crust directly impacts how current seismic hazard models replicate ground shaking and surficial energy propagation. On average, the SAF system accommodates a plate motion rate of ~49 mm/yr over its entire trace (DeMets et al., 1994; Ye and Liu, 2017). This motion is distributed through fault segments, which are generally defined by recurrence interval, slip rate, and average displacement per rupture event. These segment characteristics serve as useful metrics in determining possible future rupture locations.

In southern California, segment slip rates vary, reaching a maximum rate of > 30 mm/yr on the Carrizo segment and a minimum rate of ~1-2 mm/yr (Weldon II. et al., 2008; Scharer and Yule, 2020). The Mojave segment, which is highlighted in this project, is separated into north and south segments. The northern segment has an average slip rate of 28 ± 7 mm/yr with a recurrence interval of M 7 or greater earthquakes ~155 yr and an average horizontal displacement of ~6-7 m per earthquake (Weldon II. et al., 2008; Young et al., 2019). The southern segment maintains the same slip rate but exhibits a recurrence interval of ~130 yr and an average horizontal displacement of ~4 m per earthquake (Weldon II. et al., 2008). The

Elizabeth Lake site is located on the southern segment but is close to the northern segment boundary (Weldon II. et al., 2008; Bemis et al., 2021; Scharer and Streig, 2019). An earthquake is capable of rupturing both Mojave segments as seen in the most recent M_o = 7.9 (Zielke et al., 2010) 1857 Fort Tejon earthquake that extended from Parkfield, CA to Wrightwood, CA (Weldon II. et al., 2008). Recent terrestrial laser scanning of the Elizabeth Lake tunnel (Fig. 1) identified ~14 cm of horizontal offset which has occurred in the last 100 years since the tunnels completion in 1911 (Tayyebi et al., 2017). Having surpassed the recurrence interval for both segments, another large rupture is likely in the near future.

2.1.2 San Andreas Fault Subsurface Structure and Properties

The SAF changes dip directions along its trace (Fuis et al., 2012, 2017). For the majority of the Mojave segment, the SAF is nearly vertical which has historically been the predicted geometry of strike-slip faults and is used in theoretical models (Sylvester, 1988; Fuis et al., 2012, 2017). The Mojave segment may accommodate a change in dip direction from ~55° S at the Big Bend to the northwest to ~37° NW in the San Bernardino Mountains to the southeast (Fuis et al., 2012). The SAF has been imaged as a positive, transpressive flower structure in Parkfield, CA (Sylvester, 1988) and as a negative, transtensional flower structure at Wrightwood, CA (Weldon II. et al., 2002), with the Mojave segment possibly functioning as a transition between them.

The Los Angeles Department of Water and Power (LADWP) completed a geotechnical study at Elizabeth Lake that identified a ~75-80° southwest-dipping main fault strand with a ~50 m wide damage zone as well as two secondary fault damage zones with smaller subsidiary faults (LADWP Final Report 2019). Within the primary damage zone, more than one fault-core was identified, each with its own secondary branches. During the construction of the Elizabeth Lake

Tunnel, drillers encountered zones of highly deformed and altered rocks spanning over ~900 m (~3000 ft) with evident fluid seepage, “mud seams”, and an oriented, valley-parallel “piano key” deformation structure (Mullholland, 1918). This ~900 m deformed zone is expected to encompass to the Elizabeth Lake drill site which sampled a total of ~165 m (~550 ft) across the valley.

2.1.3 Geologic Framework

This study is focused within the Leona Valley northwest of Elizabeth Lake, CA, which contains a portion of the Southern Mojave Segment of the San Andres Fault (Fig. 1) (Dibblee, 2002; Hernandez, 2011). The Pacific Plate side of the fault is comprised of Cretaceous (~90 Ma) quartzo-feldspathic and amphlibolite gneiss (Dibblee, 2002; Hernandez, 2011), which are characterized by feldspar, quartz, biotite, hornblende and accessory garnet. The metasedimentary rocks exhibit internal-isoclinal folding and localized quartz-rich and biotite schist layers (Hernandez, 2011). The North American Plate side of the fault comprises Late Cretaceous quartz diorite to granodiorite (Ross, 1984; Dibblee, 2002; Hernandez, 2011), which in outcrop appear moderately to weakly coherent, are slightly gneissic with sodic plagioclase feldspar, biotite mica, and minor quartz and potassium feldspar (Dibblee, 2002). There is a possibility for other rock types at depth that may have been incorporated through multiphase deformation over the >200 km slip history of the fault. The regional exhumation of the Mojave Segment is ~2 km over the past ~6 Ma, based on low-temperature thermochronology (Spotila et al., 2002), with a maximum of ~2-4 km exhumation for the SAF within the San Bernardino Mountains to the southeast (Dor et al., 2006). Due to intra-fault exhumation, some rocks may have exhumed from greater depths. Based on regional exhumation studies, we reasonably

assume that at 2 km depth, the rocks within this fault zone reach a maximum overburden pressures of ~50-60 MPa lithostatic and ~20 MPa hydrostatic, and with an assumed geothermal gradient of 30°C/km, achieve a maximum ambient temperature of ~60 °C (Lachenbruch et. al, 1985; Buscher and Spotila, 2007).

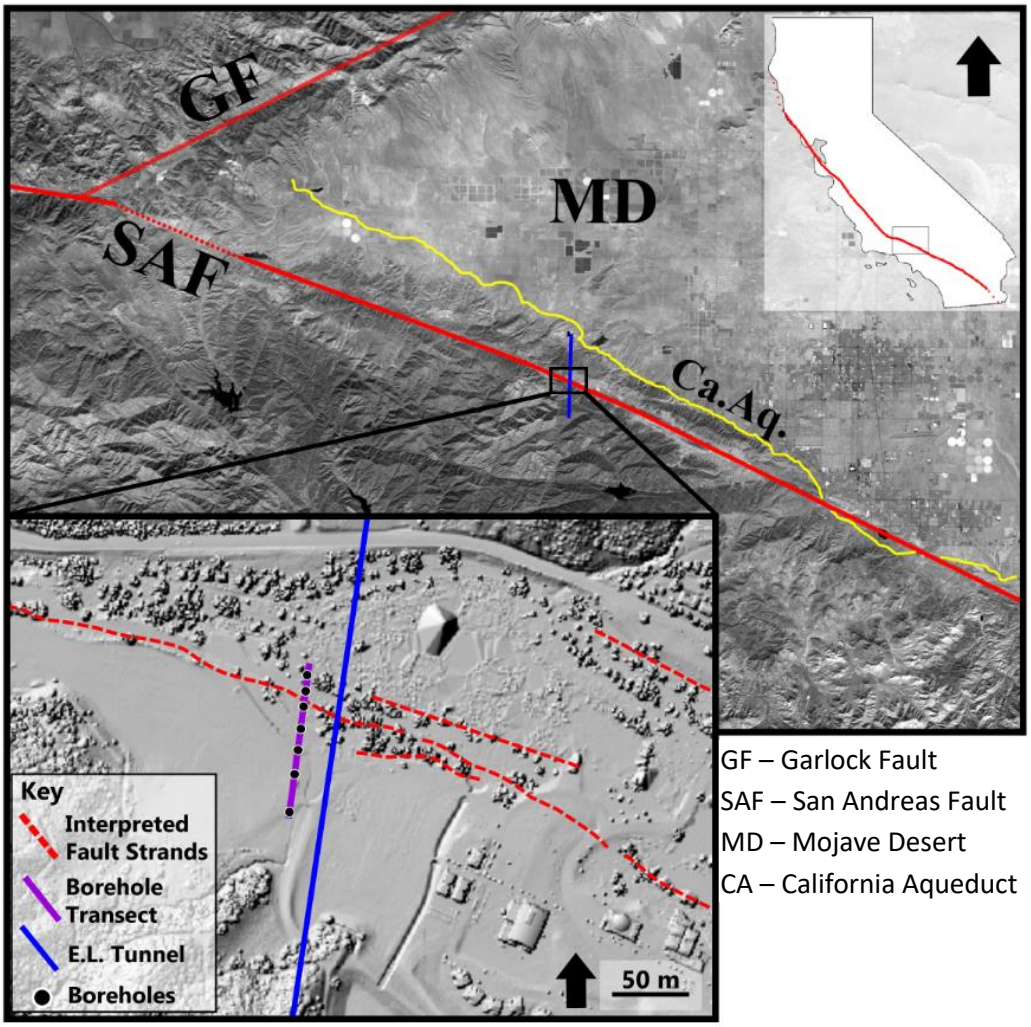

GF – Garlock Fault
SAF – San Andreas Fault
MD – Mojave Desert
CA – California Aqueduct

Figure 1. Location and LiDAR imagery of the Elizabeth Lake drill site. Modified from LADWP Final Report (2019).

2.2 Shallow Slip Deficit

Recent studies have proposed the concept of a shallow, coseismic slip deficit in which only a portion of the slip produced at depth is observed at the surface (Fig. 2) (Fialko et al., 2005; Kaneko and Fialko, 2011; Roten et al., 2017; Scott et al., 2019). Slip inversions on a number of faults indicate that coseismic slip associated with large-magnitude earthquakes on large strike-slip faults reaches a maximum within the upper ~3-6 km of a fault and may dissipate to ~50% of the maximum in the upper most ~3 km (Fig. 2) (Kaneko and Fialko, 2011; Dolan and Haravitch, 2014; Scott et al., 2019). Geodetic inversions indicate aseismic slip along creeping segments of large faults may accommodate a rate of a few mm/yr with a decreased slip rate in the shallower portions of faults (Ryder and Bürgmann, 2008). Although some averaged creep rates can accommodate an ~M 6 earthquake each year (Ryder and Bürgmann, 2008), in many major M ≥ 7.0, earthquakes, the observed recovery is insufficient (Kaneko and Fialko, 2011; Roten et al., 2017).

The slip deficit may be recovered through post-seismic afterslip or interseismic creep (Marone et al., 1991; Rice, 1993; Ryder and Bürgmann, 2008; Roten et al., 2017). Current hypotheses to explain how the slip deficit is accommodated relate to off-fault deformation or the distribution of slip as plastic deformation (Roten et al., 2017). Support for these hypotheses stems from the observations of the crust's uppermost few kilometers exhibiting a greater proportion of cracks, voids and pores, a lower coefficient of friction in damage zone rocks (Dolan and Haravitch, 2014) and the likelihood of a velocity strengthening behavior (Fialko et al., 2005) relative to intermediate depths. Fault damage zones tend to be characterized by low seismic velocities (Unsworth and Bedrosian, 2004; Cochran et al., 2009; Jeppson et al., 2010; Zoback et al., 2010), and other geophysical properties such as low electrical resistivities (Unsworth and

Bedrosian, 2004; Jeppson et al., 2010). These low velocity zones (LVZ) form in three dimensions and their widths generally diminish with increased depth and distance from the fault creating a volume of damage (Ben-Zion and Sammis, 2003; Griffith et al., 2012). Within the San Jacinto Fault Zone, this velocity structure is observed within the uppermost ~3-5 km and extends up to 100 m across (Dor et al., 2006). Lower seismic velocities within damage zones result from an increase in fracture density, induced mineral alteration (Schulz and Evans, 1998; Isaacs et al., 2008; Zoback et al., 2010), and/or increased pore fluid pressures (Unsworth and Bedrosian, 2004), similar to the mechanisms hypothesized for creating the slip deficit. The most pronounced effect of the LVZ is concentrated within the upper ~5 km (Fig. 2) (Allam and Ben-Zion, 2012) and has been recognized as more apparent within bands of highly deformed fault gouge (Jeppson and Tobin, 2015; Roten et al., 2017). A multitude of micro-seismic events accommodating small amounts of slip throughout the entire damage zone and/or mechanical and chemical processes utilizing a larger proportion of energy within the upper crust may recover the slip deficit (Dolan and Haravitch, 2014). With relatively few observational studies on shallow-bedrock fault rocks, determining the deformation and alteration textural relationships of these rocks is difficult.

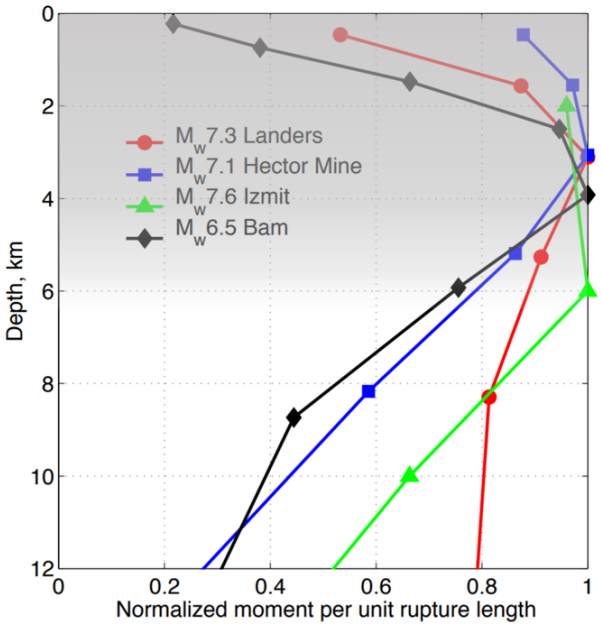

Figure 2. Graphical representation of the evidenced shallow slip deficit for strike-slip faults. The maximum slip for large earthquakes is concentrated at ~3-5 Km depth and decreases towards the surface (modified from Fialko et al., 2005). Shaded region shows the pronounced low velocity zone extent (Allam and Ben Zion, 2012).

2.3 Note On Terminology

Understanding the temporal evolution of a damage zone is complicated as very few fault-related textures have their formative rates well constrained, especially within the context of a mature fault damage zone. Each earthquake rupture is accommodated by seismic, or a combination of seismic and aseismic slip mechanisms (Poley et al., 1987; Ryder and Burgmann, 2008) and the transition between mechanisms is represented by a change in both slip behavior and slip rate. Coseismic deformation in the brittle crust occurs at rates ≥ ~10^{-4} m/s, aseismic deformation occurs at rates ~10^{-10} m/s (Rowe and Griffith, 2015), and post-seismic healing may occur as early as the termination of coseismic rupture and continue until the onset of the next earthquake event. Although these rates are not hard boundaries, they do provide a general basis for categorizing and identifying slip mechanisms. The variable styles and degrees of damage and alteration identified within our rocks makes it unlikely for us to be able to form any direct temporal relationships within a single earthquake cycle, which we identify as the time period between the onset of earthquake ruptures. We are sometimes able to classify individual deformation structures as coseismic or aseismic, but we cannot say that these processes occurred within the same earthquake cycle. For the purposes of this study, time is therefore understood at two distinct scales; seismic rate and multi-cycle processes. Seismic rate refers to the velocity at which a fault related process is known to, or expected to occur. This is identified on the time scale of a single earthquake cycle and will be referred to as its earthquake cycle phase categorization; coseismic with slip rates ≥ ~10^{-4} m/s, aseismic with rates ≤ 10^{-10} m/s, or healing. Fault healing will refer to alteration, fluid or heat processes which occur throughout the interseismic period. When a slip rate is ambiguous, the term deformation event will be used. Deformation and rupture events will be used to record the expected minimum number of earthquake cycles required to create the observed damage zone structure or texture. Where

possible, we will use the textural identifiers of seismic rates to characterize individual deformation events and use their cross cutting relationships to make inferences about the interactions of the observed deformation and alteration processes over multiple earthquake cycles.

The classically accepted fault rock classification scheme (Sibson, 1977) is currently being reexamined (Rowe, Williams, Kirkpatrick Pers. Comm. 09/2019; see also Holdsworth, 2004) and in this work, we use selected terms from Sibson (1977) that hold true for my observations and provide definitions for terms that more completely describe our fault rocks.

3. METHODS

3.1 Hard Rock Sampling

Core samples were collected from seven inclined boreholes drilled by Ruen Drilling with site geology and core analyses performed by staff geologists at Amec Foster Wheeler and Lettis Consultants International, Inc. under contract with the Los Angeles Department of Water and Power (LADWP) at Elizabeth Lake, Ca (Fig. 3). The inclined boreholes were drilled to a maximum of ~140 m total vertical depth (Tvd) (~ 450 ft Tvd) reaching a lowest elevation of 845 m (2770 ft) above sea level (Fig. 3). In total, approximately 752 m (2,468 ft) of bedrock (HQ) core, measuring 6.35 cm (2.4 in) in diameter, was recovered. Additional information about data acquisition and analyses conducted by the LADWP can be found in Appendix 1. At Utah State University, we have 18 core boxes containing approximately 54 m (175 ft) of selected core from all seven cores (Appendix 2). Ten additional samples were provided by Dr. Randy Williams at the University of Wisconsin-Madison to enable us to examine the main fault-core properties. Samples were selected based on on-site qualitative mesoscopic observations in order to provide a representative suite of the textural and rheological properties within the fault system. A first set of samples was collected by Dr. Evans in June 2017, and a second set was acquired in February 2019 by Studnicky and Evans. Initial geologic observations were summarized by Dr. Kate Scharer of the U. S. Geological Survey, and by Scott Lindvall of LCI. Core selections for this project were based on four main criteria: 1) Sample distribution through depth for each individual borehole, 2) Rock type variability, 3) Degree of deformation, e.g. brittle cataclasite, and/or undeformed host rock, and 4) Colors and textures indicative of mineral phases, alteration, and deformation. These core samples were analyzed through qualitative mesoscopic logging, microscopic structural and mineralogical classification, and whole rock and trace mineral identification.

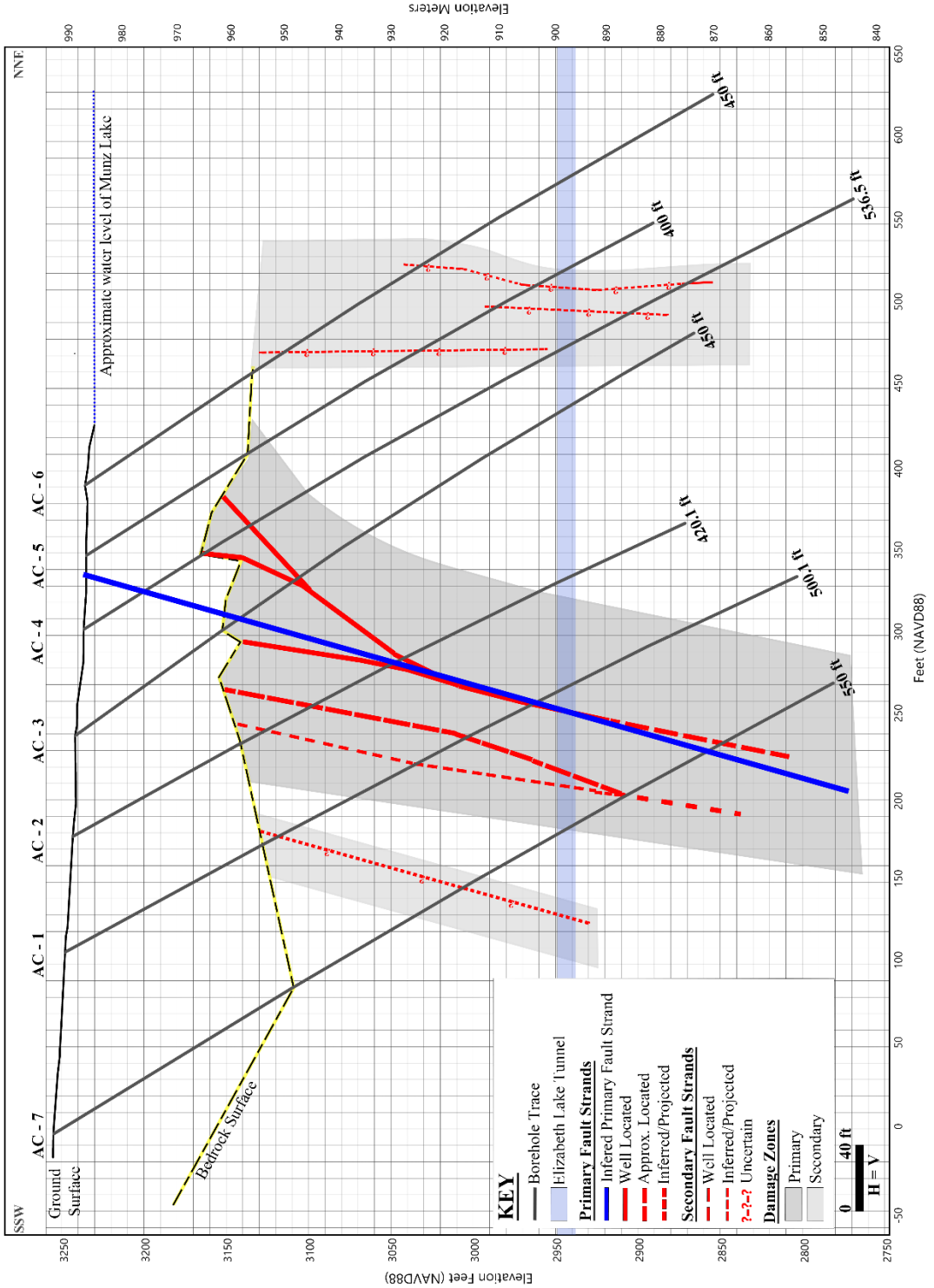

Figure 3. Cross Section of inferred fault structure and associated damage zones. Blue dashed line indicates the trajectory of the single fault trace used for sample normalization. Modified from the LADWP Final Report 2019.

3.2 Petrographic Microscopy

A total of 92 thin sections were created from epoxied core. Thin sections were outsourced with 15 standard (27 x 46 mm x 30 µm), polished thin sections created by Wagner Petrographic and 58 standard, polished and 19 large (51 x 75 mm x 30 µm), polished thin sections created by Spectrum Petrographic. Thin section images were captured for all 92 thin sections using a Zeiss Axioscope with a motorized X-Y stage and stitched together with ZEN (Zeiss) software at McGill University in Montreal, Quebec. All plane-polarized and cross-polarized images can be found in Appendix 3. Standard thin section high resolution scans were photographed at 10x magnification in plane polarized and cross polarized light. Each final image contains approximately 2,000-2,200 stitched photographs. Large unpolished thin sections were photographed at 5x magnification in both plane polarized and cross polarized light. Each final image is comprised of approximately 1,600-1,800 stitched photographs. Standard optical microscopy practices were followed on a Leica microscope for identifying the microstructural features and mineralogic compositions of the thin sections.

Scanning electron microscopy (SEM) and electron dispersive X-ray spectrometer (EDS) analyses were conducted at two laboratories. At McGill University, we used a JEOL 8900 with a PulseTorr SSD EDS detector and at Utah State University, we used a FEI Quanta FEG 650 FE-SEM with a secondary Oxford EDS detector. Thin sections were carbon coated and analyzed under high and low vacuum. SEM imagery can be found in Appendix 5 and EDS data can be found in Appendix 6.

3.3 Mineralogical and Geochemical Analyses

X-ray Diffraction (XRD) analyses of 75 samples were conducted at Utah State University on a Panalytical X'Pert Pro XRD Spectrometer with monochromatic Cu K-alpha radiation, using the High Score software program to index peaks and identify minerals. Samples were run with 0.02° steps per second over 2-75° at 45 kV and 40 mA. At the time of writing this, detailed analyses of the XRD results were prohibited due to equipment malfunction. General results from basic diffraction peak characterization were used to support fine-grained mineral identification (Appendix 7).

X-ray Fluorescence (XRF) analyses for 46 samples were examined by ALS Minerals for major, minor, trace, and rare-earth elements using ICP-MS analyses. Analytical data were checked by duplicate analyses at the ALS labs, and all analyses are in Appendix 8.

In order to standardize our quartzo-feldspathic protolith data, we incorporate quarto-feldspathic protolith geochemical analyses from nearby studies (Ross, 1984; Weschler et al., 2011). The XRF rock samples were categorized into five rock-type groups based on microscopy and macroscopic observational analysis of the lithologies, the style and degree of deformation, and the general trends in composition. For each rock type, we performed bootstrapping statistical analyses on the XRF bulk-rock data with 90% confidence intervals in MatLab. We randomly sampled our data with replacement 1500 times and calculated the mean for each run. We then calculated a 90% error ellipse of the mean and variance for each rock type based on two variables, one being the $\%SiO_2$ and another being the indicated bulk-rock measurement. We plotted the error ellipses to identify any significant differences in geochemical compositions between the rock types. Procedural assistance and code were provided by Dr. Randolph Williams at University of Wisconsin-Madison.

3.4 Data Normalization

For location discussion purposes, sample locations, including thin sections, XRD, and XRF analyses, were normalized to a single inferred main fault plane based on the trace of the well located main strand identified in the LADWP Final Report (2019) (Fig. 3). We calculated the perpendicular distances between the inferred fault plane to each sample to identify trends away from the main fault core.

Core rheologic properties, microstructural and mineralogical observations, and geochemical analyses are normalized to the fault plane. The combination of these data allow for a qualitative analysis of fault zone processes including heat generation and dispersion, fluid flow and alteration, and timing, in terms of both seismic rate and fault zone evolution/overprinting, throughout the damage zone. This combined analysis provides insight into the formation and active processes of the shallow damage zone and fault core of the San Andreas Fault at Elizabeth Lake, CA.

4. RESULTS

4.1 Macroscopic Core Observations

In this section, we present descriptions of key lithologies, deformation textures and mechanisms, and alteration assemblages and textures identified within the Elizabeth Lake core. Due to the wide range of variability within the core, the following samples been chosen as references for terminology used throughout the remainder of the paper. These do not encompass all possible rock types encountered throughout this study. Additional core images and descriptions can be found in Appendix 2.

We examined core at the Elizabeth Lake site and focused on intervals to sample for optical microscopy, X-Ray diffraction, X-Ray fluorescence, and ICP-MS whole -rock geochemical analyses. The sample selection process described in the methods section yielded ~54 m of core from 7 boreholes that we retrieved for further analyses. We classified the rocks based on three mesoscopic criteria for each sample: 1. Lithology, 2. Degree and style of deformation, and 3. Degree and nature of alteration. The SAF at Elizabeth Lake juxtaposes Cretaceous granodiorites on the northeastern flank with amphibolite gneiss on the southwestern flank (Ross, 1984; Dibblee 2002; Hernandez et. al., 2011). Throughout the recovered core, we identified predominantly granodioritic protolith with intervals of mafic amphibolite gneiss, quartzo-feldspathic gneiss, fault-related gouge, cataclasite, and zones of chlorite-rich sheared rock. The degree of deformation and alteration within our samples for all rock types range from lightly damaged/altered to completely damaged/altered with an end member represented by fault gouge. Despite the intense degree of alteration and deformation exhibited in these rocks, the core is moderately to highly indurated and core recovery was ~97% (LADWP Final Report, 2019).

The sample naming convention throughout this paper is defined as Core number_ Measured depth-Range (ft). For example, sample 1_100-101 reading as “Core 1 from 100 to 101 ft measured depth”.

4.1.1 Lithologic Classification

Granodiorite accounts for the majority of the protolith in the core samples. For the remainder of this paper, the term quartzo-feldspathic will be used to encompass the granite, granodiorite, diorite, and quartz-diorite lithologies. In hand samples, the quartzo-feldspathic rocks are composed of quartz, feldspar, plagioclase, biotite, chlorite, and/or iron-oxide (Fig. 4A). We identify the quartzo-feldspathic gneiss as a unique subsect of the quartzo-feldspathic rocks due to its change in protolithic texture. Gneissic banding on the order tens of cm thick is identifiable in amphibolite and quartzo-feldspathic host rocks. The gneissic bands define alternating mostly white felsic bands with green-grey, brown-grey, or red alterations and darker mafic grey-black or green-black bands (Fig. 4B). The quartzo-feldspathic rocks are typically medium- to coarse-grained and range from mostly undamaged protolith to disaggregated and/or altered fault rocks. The black, fine-grained amphibolite is composed of amphibole, biotite, and plagioclase (Fig. 4C). The fault gouge, from which the protolith is no longer identifiable (Fig. 4D), varies from brown to grey, purple, white, or green and often display an oriented shear fabric with remnant quartz, plagioclase, feldspar, and/or opaque mineral grains suspended in the matrix. Gouge zones may be cataclastic and clay-poor, or a combination of cataclasite and altered rocks rich in clay minerals.

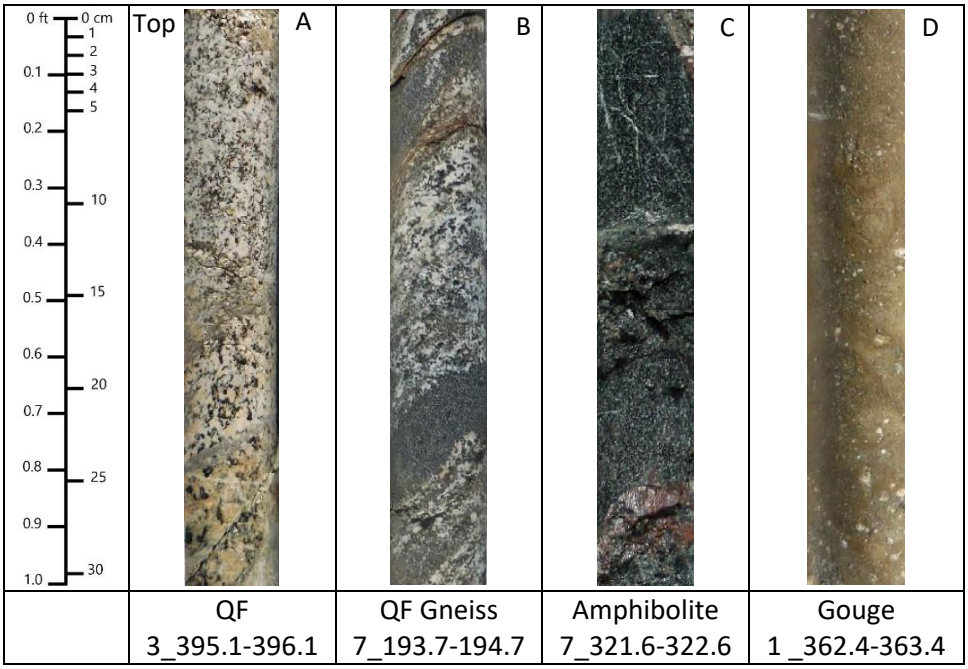

Figure 4. Lithologies identified in drill-core. A) Example of relatively undeformed quartzo-feldspathic rock showing variable grain sizes which generally increase downhole. B) Example of quartzo-feldspathic gneiss with alternating white and grey, medium-grained felsic layers and grey, fine-grained mafic bands. C) Example of a fine-grained, black-green amphibolite gneiss with zeolite veins in the uphole half and an iron-oxide slip surface in the downhole half. D) Example of a tan-brown, fine-grained gouge showing a low proportion of macroscopic clasts.

4.1.2 Alteration Assemblages

Common alteration assemblages include rocks rich in chlorite and iron-oxide, veins, and clay-rich gouge (Fig. 5). Chloritization is expressed as a fine-grained grey-green matrix (Fig. 5A) whereas iron-oxide alteration occurs as red-stained rocks and in fractures (Fig. 5B). It is common for orange rims to form around larger concentrations of oxide minerals. The primary and deformation-induced rock fabrics are frequently cut by white veins composed of either zeolite, calcite, or quartz (Fig. 5C). Gouge zones are fine-grained and lack abundant, remnant protolith clasts. Some portions of gouge contain swelling clays, as noted by the core behavior when in

contact with water, and some of these zones are tinted purple, green, grey, or red-brown (Fig. 5D).

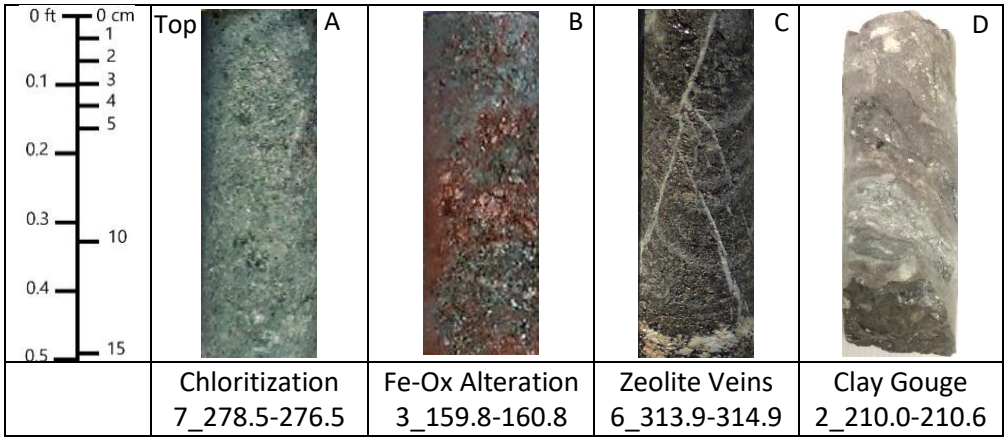

Figure 5. Common alterations at the mesoscopic scale. A) Example of fine grained, green-grey core which has undergone chloritization. B) Example of a red-stained drill-core showing evidence of iron-oxide alteration. C) Example of a gneissic amphibolite with a cross cutting zeolite. D) Example of a clay rich gouge showing a fine-grained, oriented fabric.

4.1.3 Deformation Style

A variety of deformation structures are identified in the samples. We observe fractures, sheared surfaces, and sheared zones that range from millimeter scale sealed veins to cm- to m-scale cataclastically sheared host rock and clay-rich gouge. Here we define cataclasites as those which have experienced mechanically induced grain-size reduction and do not contain ample evidence of clays. Gouge is defined as fault materials which contain clay minerals, likely the result of fluid-mediated alteration, as well as mechanically ground host rock clasts. Fractures are typically filled and the nature of any open space or void is uncertain as it may be connected to core recovery. Sealed fractures often contain zeolites, calcite, iron-oxides, or clays. Fracture density varies and produces sections of core that have oriented fabrics, webbed fracture

patterns, brecciated clasts, and/or cataclasites. Foliated or oriented fabrics are seen throughout the core and can be attributed to dispersed oriented shearing and sometimes to gneissic protolith (Fig. 6A). The oriented fabrics occur within both the host rock and the gouge sections. Webbed fractured sections contain a high density of thin fractures, which are predominantly aligned with secondary cross cutting fractures (Fig. 6B). These are similar to a scaly texture and to foliated cataclasites with a very high density of oriented slip surfaces. Brecciated sections show a network of cross cutting fractures with variable compositions, densities, and thicknesses on the meter scale (Fig. 6C). Some intervals of core appear to be pulverized as the samples crumble with normal handling. Most of the pulverized sections or clasts are quartzo-feldspathic, lacking abundant mafic minerals and appear as a chalky white (Fig. 6D).

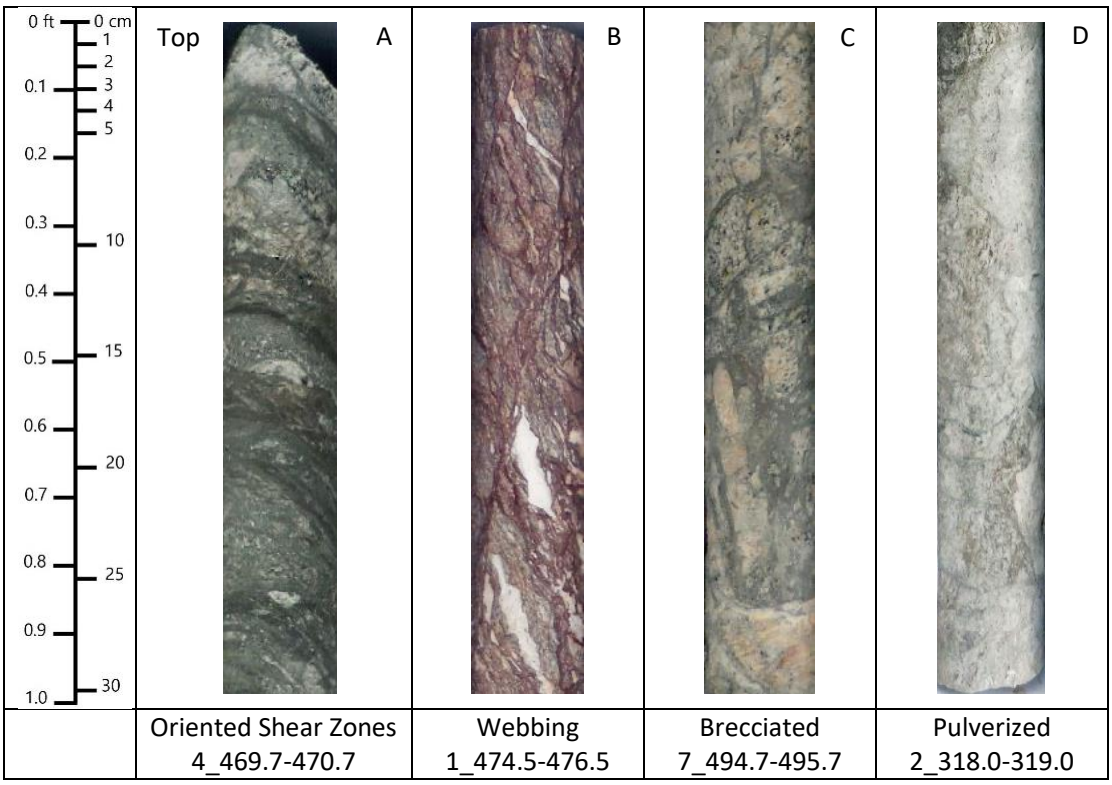

Figure 6. Common deformation styles at the mesoscopic scale. A) A set of oriented, fine-grained, grey-green-black shear surfaces in a fine grained amphibolite drill-core. B) Webbed fractures showing a high density of oriented shear surfaces with evidence of iron-oxide alteration and white clasts of likely leached pulverized rock. C) Brecciated fabric of a quartzo-feldspathic drill core. Protolith clasts are entrained within a set of shear surfaces showing a random orientation. D) Fine-grained pulverized rock likely to disaggregate upon handling.

4.2 Thin Section Petrography

We examined 92 thin sections from 7 boreholes with optical and scanning electron microscopy in order to determine the extent and nature of alteration, and the range and nature of deformation textures and mechanisms present in the fault-related rocks (Fig. 7). In this section, we will provide definitions and examples of the common deformation and alteration textures and assemblages identified through optical microscopy and SEM. These descriptions identify the key features of our optical microscopy work, but many identified textures and

mechanisms exist on a spectrum and may not represent the entirety of the feature variability within the samples. Additional images and descriptions can be found in Appendix 4.

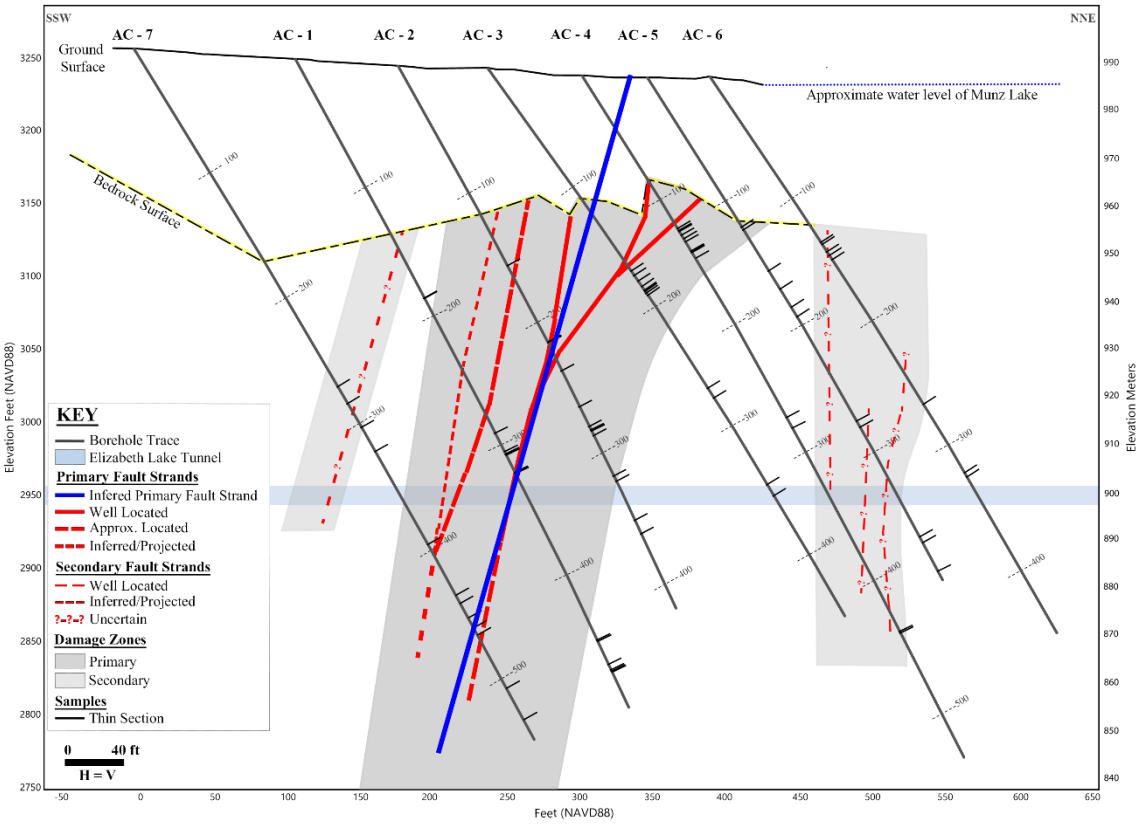

Figure 7. Thin section sample locations. Thin sections were sampled across the fault damage zone, at varying depths within each core and with consideration given to the variety of macroscopically observed deformation and alteration textures throughout the fault damage zone. Boreholes are measured in ft. Adapted from LADWP Final Report (2019).

4.2.1 Petrography

We identify four main rock types within the thin section samples based on microstructures and the degree of alteration: amphibolite, quartzo-feldspathic rocks, pulverized rocks, and gouge. The categorization of a fault damaged rock indicates either an amphibolite or

quartzo-feldspathic protolith that has been fractured or sheared and incorporates zones of cataclasite, pulverized rock, or gouge. Within the quartzo-felspathic classification, rocks were identified within the mineralogic range of diorite to granite. Here we discuss the nature of these rocks and provide a description of each sample.

The amphibolite (Fig. 8A) comprises predominantly sodic plagioclase, clinopyroxene, hornblende, chlorite, and/or iron-oxides with minor quartz and apatite. Alteration minerals include zeolite, calcite, and muscovite veins and the seritization of plagioclase grains. The amphibolite samples are typically less deformed and altered overall.

The quartzo-feldspathic phases (Fig. 8B) consist of quartz, sodic plagioclase, alkali feldspars, hornblende, clinopyroxene, biotite, zeolites, chlorite, and/or iron oxides with less common to minor titanite, epidote, rutile, garnet, muscovite, and apatite. Common alteration minerals include calcite, zeolite, and or quartz veins with feldspars altering to zeolite, sericite, sausserite, and/or calcite.

Although any lithology can be classified with the deformation style of pulverized rocks, within this study we describe these rocks as a single rock class. Pulverized minerals are predominantly quartz, sodic plagioclase, biotite, chlorite, and/or opaque minerals with less frequent to minor muscovite (Fig. 8C). The most common alteration material identified is calcite as a vein/cement.

It is challenging to identify gouge mineralogy due to the fine-grained nature and relatively low clast percentage (Fig. 8D). The most common identifiable clasts consist of quartz, zeolite, calcite, opaque minerals, feldspar, and less commonly clinopyroxene. Calcite and zeolite are often identified as altered or cemented clasts.

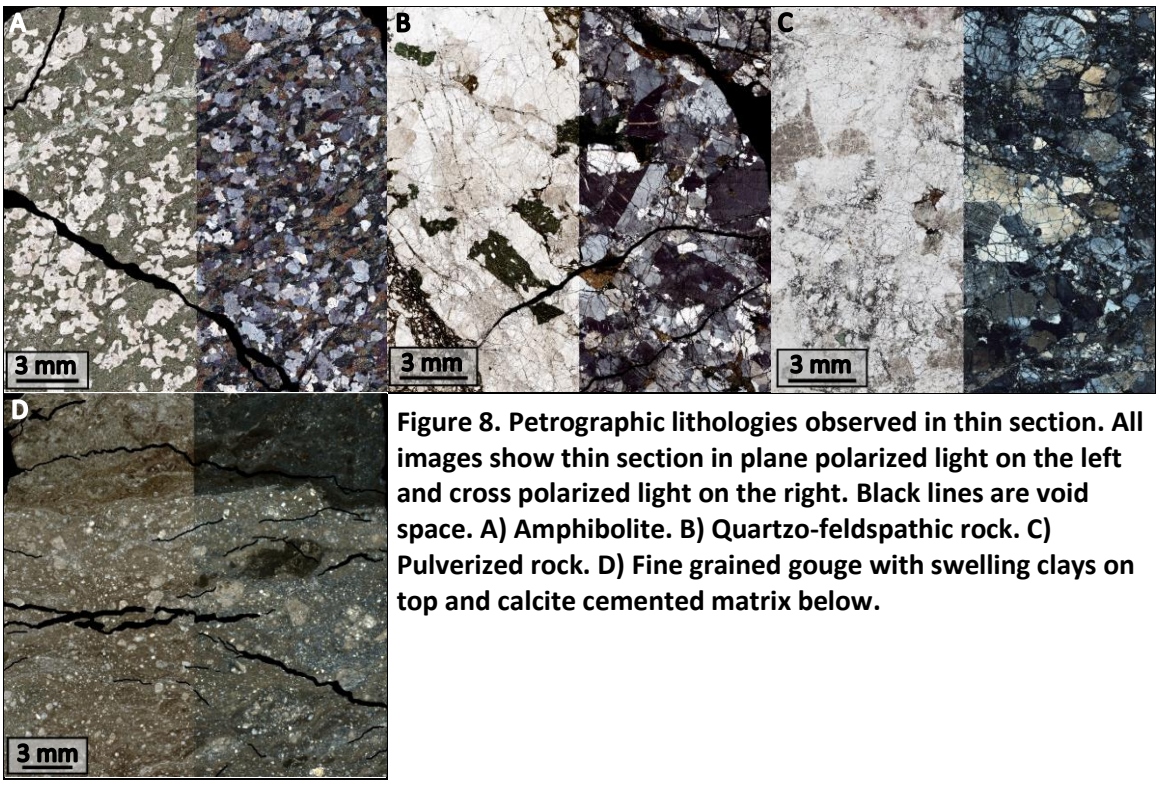

Figure 8. Petrographic lithologies observed in thin section. All images show thin section in plane polarized light on the left and cross polarized light on the right. Black lines are void space. A) Amphibolite. B) Quartzo-feldspathic rock. C) Pulverized rock. D) Fine grained gouge with swelling clays on top and calcite cemented matrix below.

4.2.2 Nature and Style of Deformation

We observe varying degrees of deformation in these rocks ranging from relatively undamaged protolith to fault-related rocks with unrecognizable, completely damaged protolith and gouge.

Relatively undamaged protolith maintains its original host rock textures and may contain a small number of fractures and veins. There is little to no displacement observed on these fractures (Fig. 9A). Lightly damaged fault rocks exhibit a higher proportion of fractures as compared to the undamaged protolith, some of which show small amounts of shear displacement. The original host rock grain texture is still easily identifiable and some grain contacts remain intact (Fig. 9B). Moderately deformed rocks show displacement along small faults and contain a fracture density which has deformed about half of the sample (Fig. 9C).

These rocks may be brecciated but the protolith clasts are still identifiable. Highly damaged rocks have a fracture density of ~10 fractures/cm and show shear displacement which makes identifying original grain textures difficult (Fig. 9D). Rocks that we term completely deformed no longer contain the original textures of the host rock (Fig. 9E). Gouge differs from completely damaged fault rocks in that there are fine-grained, matrix supported clasts which no longer display the original protolith textures (Fig. 9F). The matrix materials in gouge samples show evidence of clay alteration. These categorizations exist on a spectrum and the samples may contain zones of more than one deformation style.

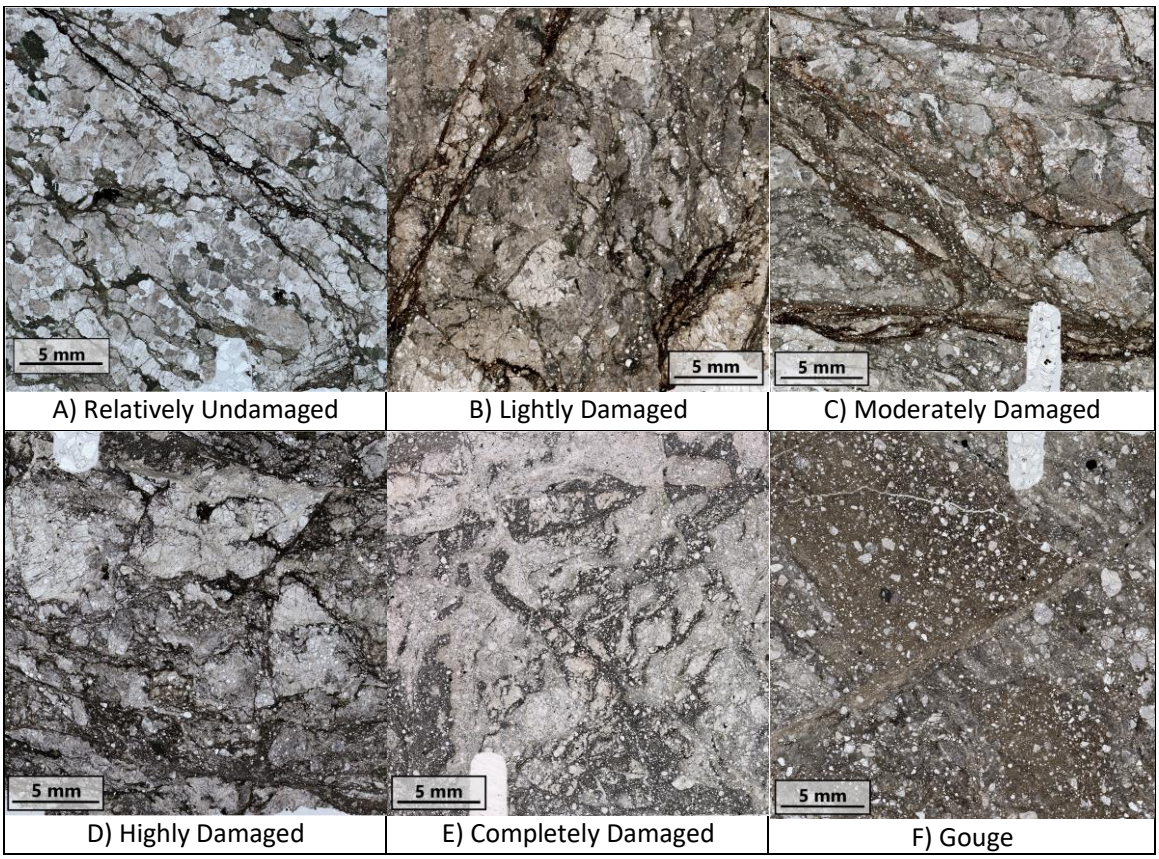

Figure 9. Definition of relative scaling of damage identified within the fault zone. All images are in plane polaraized light. A) A single fracture cuts across grain boundaries with smaller fractures localized along grain contacts showing little evidence of displacement. B) Multiple oriented fractures cut through, and have displaced the host rock which contains a high proportion of intragranular fractures. C) Cross-cutting fractures and foliated cataclasites make up about 50% of the sample and provide good evidence of sustained displacement. Grain boundaries and original protolithic textures and mineralogy are still easily identifiable. D) The sample is composed of predominantly sheared fault rock materials with a few mm scale clasts of the host rock. E) Sheared pulverized rock containing multiple cross cutting orientations. The sample no longer contains evidence of the protolithic host rock textures. F) Clasts suspended in an optically opaque matrix with one predominant orientation cross cut by a secondary shear. There is no evidence of the protolithic host rock textures.

Relic textures. Pre-existing, deformation textures inherited from metamorphism and pre-SAF deformation of the protolith are likely not associated with SAF-related brittle fault processes. Quartz recrystallization textures that reflect subgrain rotation and grain boundary migration are common throughout the quartzo-feldspathic rocks (Fig. 10) and indicate

temperatures of >400 °C (Stipp, 2002). Plagioclase grains co-located with the quartz grains are often twinned and altered to sericite, sausserite, calcite, zeolite, and/or reduced to a pseudomorph, but do not show ample evidence for dynamic recrystallization. This temperature regime indicates formative depths deeper than 2km for rocks containing evidence of plastic deformation in quartz.

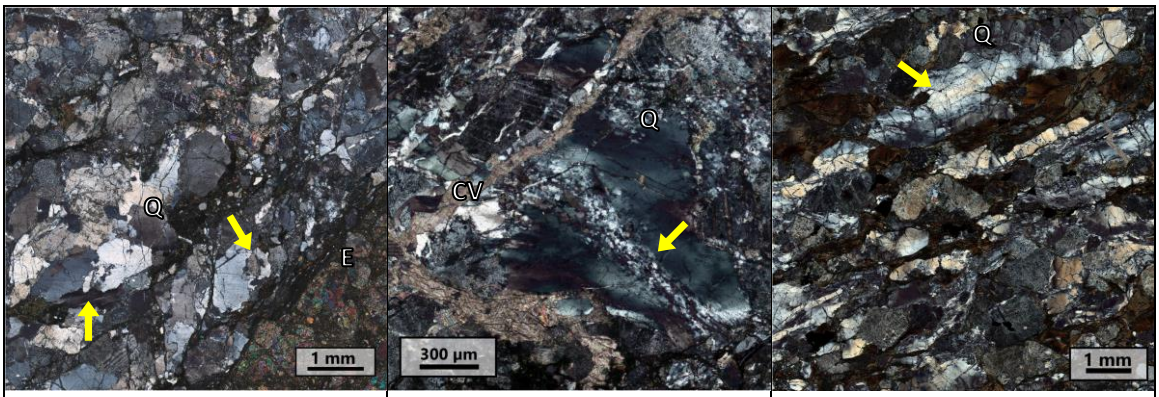

A) Grain Boundary Migration	B) Bulging Recrystallization	C) Dislocation Glide

Figure 10. Relic quartz deformation. All images are in cross polarized light. A) Grain boundary migration identified by bulging, rounded grain boundaries. Fracture in bottom right shows contact between quartzo-feldspathic fault rock and epidote (E) shear. B) Bulging recrystallization identified by throughgoing plastic deformation and formation of small, re-oriented crystals. Quartz grain is cut by calcite vein (CV). C) Dislocation glide identified by grain stretching resulting in smooth, oriented changes in quartz extinction angles.

Fracture geometry. The contacts between the host rocks and the cataclasite and/or gouge zones are either sharp and straight (Fig. 11A), or undulatory (Fig. 11B). Sharp fractures cut directly through wall rocks and maintain a relatively consistent trajectory, whereas undulatory contacts appear to have plucked grains along existing grain weaknesses and often create irregular contacts. Discrete fractures are singular or paired shear zones or fractures which do not heavily damage the surrounding host rock (Fig. 11C). “Soft” shears are those which display obvious elements of displacement over a volume of space but do not show defined slip contacts

and which are identified by changes in grain orientations or mineralogy (Fig. 11D). Distributed shears are identified as a multitude of oriented fractures showing displacement, which deform the host rock over a distance or volume of rock with defined slip surfaces (Fig. 11E). The geometry of fracture contacts is partially dependent upon the local stress regime and the style of the contacts can be used to infer rheologic properties of the fault-rocks prior to the deformation event (Minghe et al., 2019; Scholz, 2019).

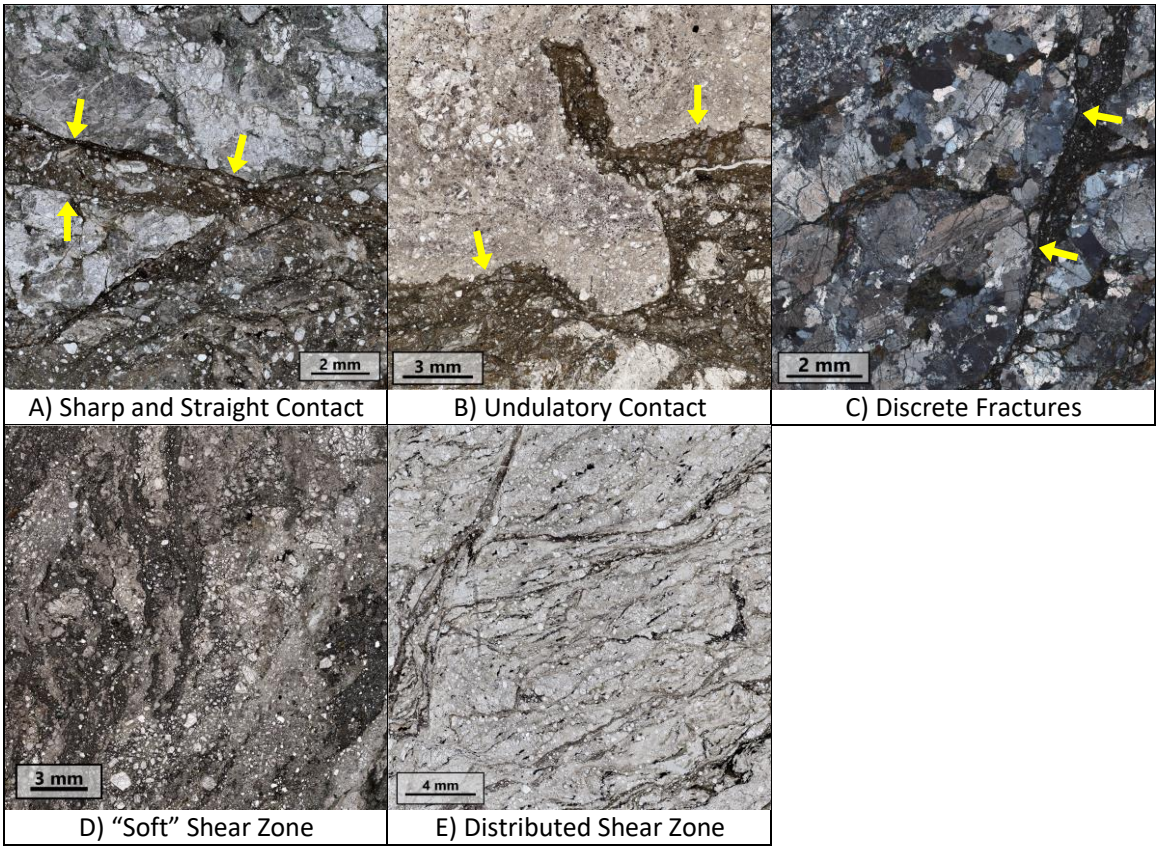

A) Sharp and Straight Contact | B) Undulatory Contact | C) Discrete Fractures

D) "Soft" Shear Zone | E) Distributed Shear Zone

Figure 11. Fracture and shear zone styles identified though optical microscopy. A) Sharp fracture contact between a gneissic quartzo-feldspathic rock and a coarse grained cataclasite. B) Undulatory contact between a fault breccia and a phyllosilicate rich gouge. C) Discrete cataclasite-filled fracture in a Quartzo-feldspathic rock. D) Sheared cataclasite showing displacement without a discrete slip surface. E) High density of discrete, oriented shear surfaces in a quartzo-feldspathic rock. Opaque minerals are localized within shear zones.

Cataclasites and shear zones. Sheared rocks display evidence of displacement and are characterized by banded, asymmetric, and/or random clast distributions. The nature of the sheared fabrics in these rocks result from displacement and mechanical grinding within shear zones. Highly sheared zones commonly exhibit a cataclastic, oriented fabric with a high proportion of fine-grained matrix and variable clast shapes and sizes. These oriented fabrics have been identified over the meter scale in core observations (Appendix 9). Here we delineate different shear zone types based on mineralogy, clast density and/or cataclastic generations (Fig. 12). Mineralogic banding is cataclastic in that there is little evidence of alteration within the individual layers and results from a mechanical shear/grain-size reduction (Fig. 12A). Clast density banding contains layers of similar mineralogy but with differing clast to matrix proportions and/or grain sizes and shapes (Fig. 12B). Generational cataclastic banding is evidence for repeated or sustained deformation within the same shear zone. As displacement and timing are hard to quantify without additional analyses, we cannot say with certainty if these cataclastic generations are the result of extended single deformation events or formed over multiple earthquake cycles (Fig. 12C). Individual generations are identified by their contact geometries and changes in their grain shape, density, and/or mineralogic contents. Shear zones displaying an asymmetric organization have one sharp fracture contact with proximally finer grains and fewer clasts. The clast size and proportion increase away from the sharp contact (Fig. 12D). Random clast distributions display variable grain sizes, shapes, and lack any clast organization within the shear zone (Fig. 12E).

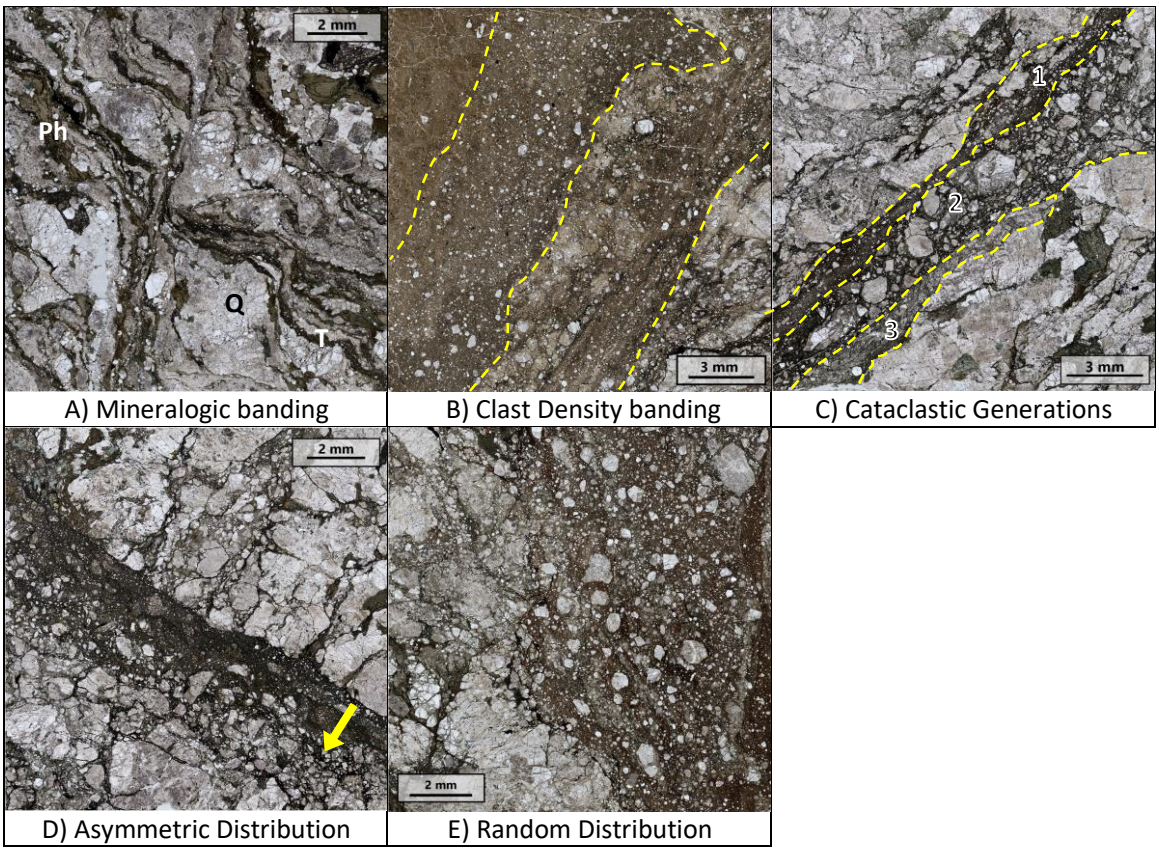

A) Mineralogic banding | B) Clast Density banding | C) Cataclastic Generations

D) Asymmetric Distribution | E) Random Distribution

Figure 12. Examples of clast organization schemes within shear zones. A) Discrete bands of quartz (Q), titanite (T) and phyllosilicates (Ph) in quartzo-feldspathic, moderately damaged rock. B) Cataclastic banding showing increasing clast density from left to right. C) Fine grained cataclasite (1), large clast cataclasite (2), and cemented cataclasite (3) in quartzo-feldspathic rock. D) Quartzo-feldspathic rock with epidote rich cataclasite showing fine grained clasts localized along the fracture contact with larger clasts away from the contact. E) Clasts of variable shapes and size randomly distributed within a cataclasite.

Phyllosilicate deformation. Phyllosilicates are often key components of parts of the SAF, which facilitate fault weakening (Knipe, 1980; Jänecke and Evans, 1988; Schleicher et al., 2006; Colletini et al., 2009; Lockner et al., 2011). Chlorite, biotite, and muscovite line shear surfaces (Fig. 13A, and 13B), contain discrete slip surfaces (Figs. 13C and 13D), and exhibit kink bands (Fig. 13D). Fractures that cut through the host rock appear to connect the preexisting phyllosilicate grains and the shear surface appears to incorporate fragments of the oriented

crystal sheets into the fractures. The ability of phyllosilicate sheets to slide is evident within shear zones as many slip surfaces are characterized by the presence of aligned phyllosilicate crystals connected by through-going fractures (Figs. 13A and 13E). In some cases, the orientations of the phyllosilicates change by up to 60° between largely undisturbed sheets and sheets which are aligned with the fracture (Fig. 13E). In moderately to highly deformed rocks, brittle deformation of preexisting biotite and chlorite grains is expressed by fractured and splayed sheets which are packed into the crevices of the surrounding fractured grains (Fig. 13F). These appear similar to granular injection veins as the secondary chlorite grains are observed as folded and deformed into the fractured rock (Rowe and Griffith, 2015).

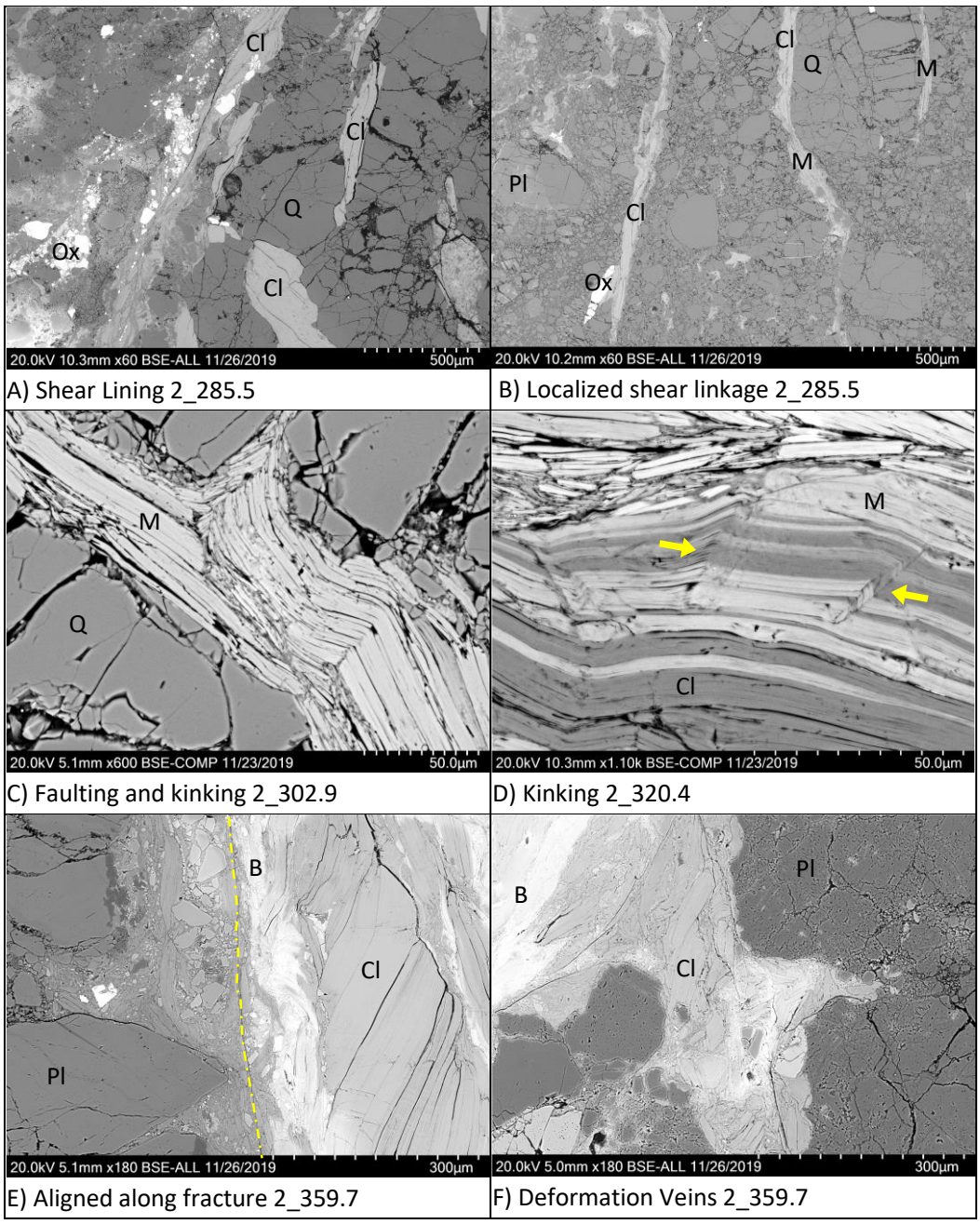

Figure 13. Examples of phyllosilicate deformation. All images are backscatter electron microscope images. A) Chlorite (Cl) lining a fracture with larger quartz (Q) clasts on the right and smaller, more displaced clasts on the left. B) Chlorite and Muscovite (M) sheared within a displaced quartz and plagioclase (Pl) fault breccia. C) A propagation fault and fold within muscovite grains. D) Kinks, identified with yellow arrows, within altered muscovite and chlorite crystals below a localized shear fracture. E) Chlorite rotated and biotite (B) aligned with through-going fracture (yellow dotted line). F) Chlorite displaced and folded into altered plagioclase fault rocks.

4.3 Alteration Assemblages

The nature and degree of alteration within our samples ranges from lightly altered to completely altered (Fig. 14). Lightly altered rocks maintain over 90% of their original mineralogy with alteration localized along fractures or as vein fill (Fig. 14A). Moderately altered rocks maintain up to ~50% of their original mineralogy and the primary lithology is easily identifiable (Fig. 14B). Highly altered rocks have ~75% of their original mineralogy replaced by alteration phases and identifying the original lithology becomes difficult (Fig. 14C). Completely altered rocks have over 90% of their original mineralogy replaced by alteration materials and the remaining unaltered grains are typically quartz (Fig. 14D). The alteration classifications represent a sliding scale and the descriptions are based on observational, not geochemical, analyses.

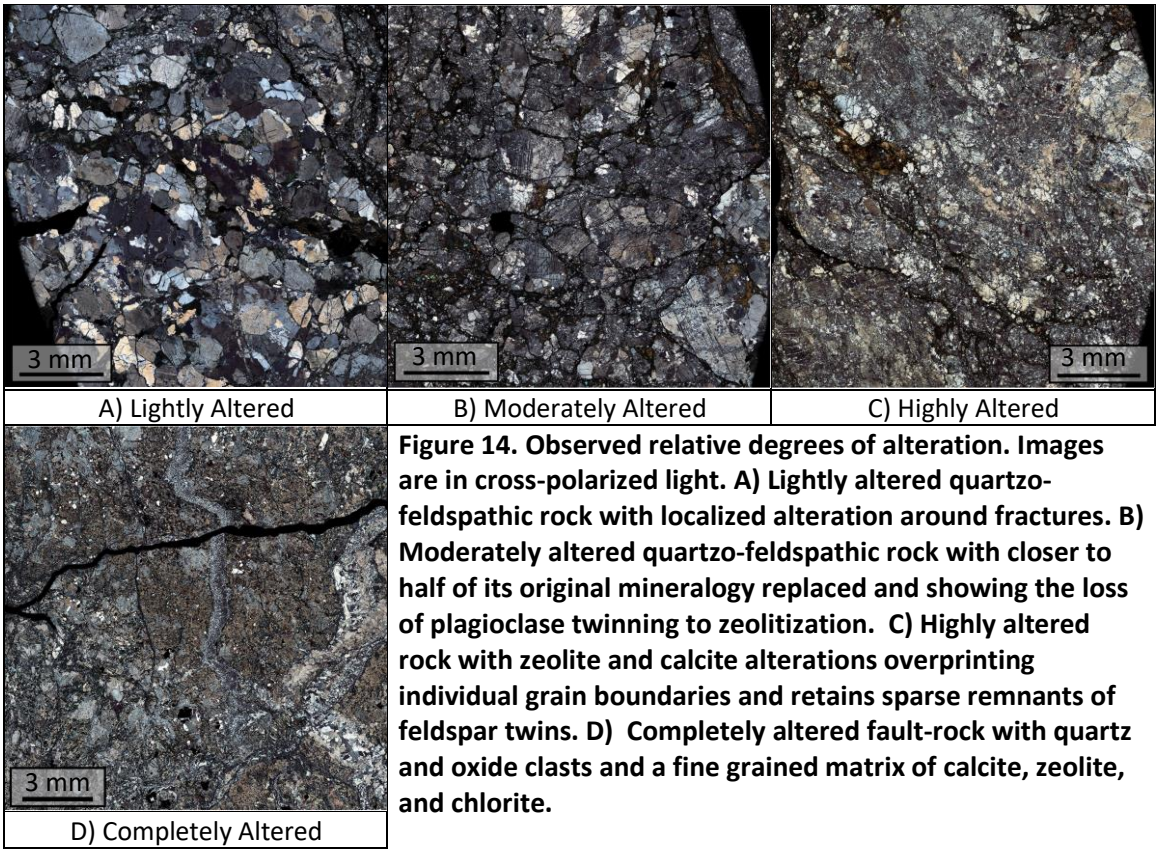

Figure 14. Observed relative degrees of alteration. Images are in cross-polarized light. A) Lightly altered quartzo-feldspathic rock with localized alteration around fractures. B) Moderately altered quartzo-feldspathic rock with closer to half of its original mineralogy replaced and showing the loss of plagioclase twinning to zeolitization. C) Highly altered rock with zeolite and calcite alterations overprinting individual grain boundaries and retains sparse remnants of feldspar twins. D) Completely altered fault-rock with quartz and oxide clasts and a fine grained matrix of calcite, zeolite, and chlorite.

4.3.1 Hydrothermal alteration

Throughout the rock types sampled, evidence of fluid-assisted alteration processes that likely occurred at temperatures above the ambient geothermal gradient exist in the form of mineral alteration, in the presence of veins, and as cementation. Sources of heat above the expected ambient geothermal gradient include short bursts of frictionally generated heat and over longer timescales, heat that is transported within the fault damage zone via advective fluid flow. We identified the most common mineral alteration processes as sericitization (Fig. 15A), sausseritization (Fig. 15A), zeolite precipitation and alteration (Fig. 15A), iron-oxide alteration (Fig. 15B), calcite precipitation, alteration, and twinning (Fig. 15C), chloritization (Fig. 15D), and plagioclase likely altering to clays (Fig. 15E). The optically feldspar-rich altered rocks show a trend of increased alteration within the alkali feldspars in comparison with the plagioclase feldspars. In the quartzo-feldspathic samples, a mesh, or web-like alteration texture, which appears similar to a serpentinization texture, was identified in damaged and altered fault rocks in contact with cataclasite (Fig. 15B).

Fault-rock cementation is due primarily to calcite and zeolite precipitation. Calcite and zeolite cements are identified within large, reworked, brecciated clasts and damaged wall rocks, as well as within fine-grained cataclasites and gouge zones (Fig. 15C). Although calcite and zeolite grains are individually identifiable in thin section, the cement in most samples appears as a fine grained matrix material with optically poor crystal structures. The distinction between the two cements is most obvious in cross-polarized light as the zeolite birefringence reaches up to a muddy yellow.

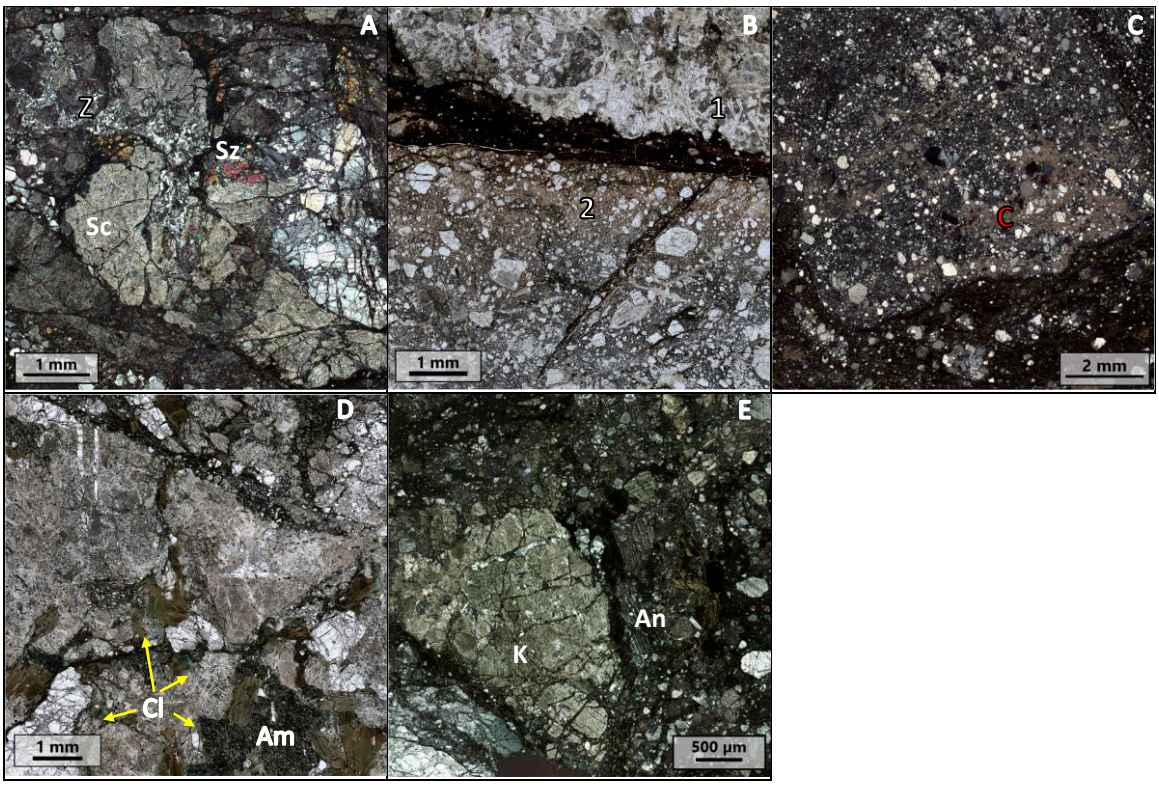

Figure 15. Common alterations identified in thin section. A) Sausseritization (Sz) and zeolite (Z) vein/replacement with sericitized plagioclase (Sc). B) Web-like alteration texture along intragranular fractures (1). Iron-Oxide Alteration entering the brecciated wall rock (2). C) Calcite cementation (C) within a sheared pulverized rock. D) Chloritization (Cl) and biotization (B) of amphiboles (Am) in highly altered feldspar. E) Preferential alteration of Feldspar (K) vs Plagioclase (An).

Veins. The presence of veins, most commonly filled with calcite ± zeolite and minor quartz, are found in proximity to slip surfaces, fractures, and joints. Veins captured in thin section measure up to ~2.5 mm in width but are typically smaller and occur most often as intra-granular fracture fill with well-defined crystals. Zeolite veins are evident throughout the damage zone. These vary in width from the tens of microns as intragranular veins and up to ~2 mm as intergranular veins. The optically macroscopic crystals are typically tabular and equant with well-defined cleavage planes at ~65° although more fibrous crystal forms were also identified (Fig. 14D). Calcite veins are often co-located with the zeolite veins and measure up to ~2 mm in

width. The calcite crystals are equant in shape and exhibit twinning (Fig. 16). Quartz veins typically appear as < 0.5 mm wide intragranular veins and the crystals consistently display undulatory extinction. These veins are often cross cut by secondary fractures with calcite or zeolite vein fill.

Vein relationships and textures (Fig. 16) provide evidence for the development of open fracture systems within the fault damage zone. Interlocking prismatic zeolite grains measure up to ~0.5 mm with larger grains located towards the center of the vein. The grains in vein 1 (Fig. 16) exhibit a vuggy relationship between the secondary calcite fill and the zeolite crystals, whereas mineral relationships in vein 2 shows the opposite formative sequence. Here the calcite vein had grown up to ~3 mm at its widest and shows consistent mechanical twinning. A secondary fracture split the calcite vein and zeolites precipitated into the space with crystal size increasing towards the center of the vein. The relationship between these veins provides evidence for open voids within fractures and alternating fluid events active within the fault damage zone.

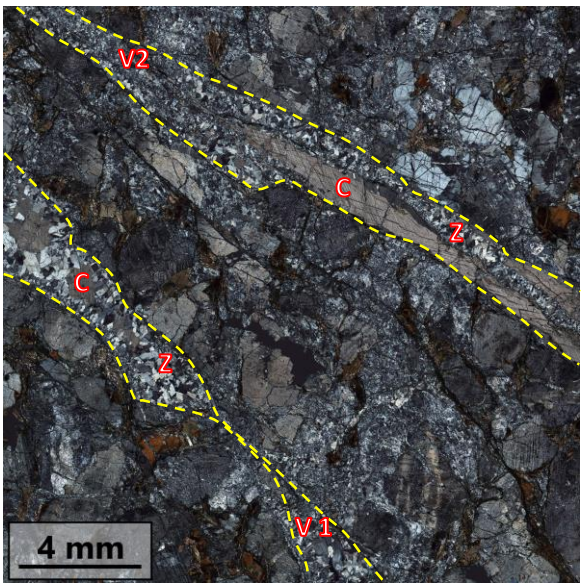

Figure 16. Evidence of open fracture systems. In sample 6_321.6, vein 1 (V1) exhibits prismatic zeolite (Z) crystals with vuggy calcite (C) crystal precipitation exhibiting a singular twinning orientation. Vein 2 (V2) shows a calcite vein with two cleavage directions cut by secondary prismatic zeolite crystals.

Zeolites. Zeolite alteration was identified as mineral replacements (Figs. 17A and 17B), cements (Fig. 17C), and as vein fill (Fig. 17D). Zeolite alteration materials are found near fractures and as the proportion of fractures decreases, so too does the amount of zeolite present in the sample. Host rocks that are relatively undamaged to lightly damaged may contain zeolite veins but often do not show ample zeolite replacement. Within highly damaged rocks, zeolites tend to form as cements or as clast replacements but can also be found as intragranular veins within individual cataclastic clasts. Intragranular zeolite veins often display a dilational texture (Fig. 17D) with asymmetric crystal shapes which increase in size across the vein and the evident lack of rotation in the bounding clasts.

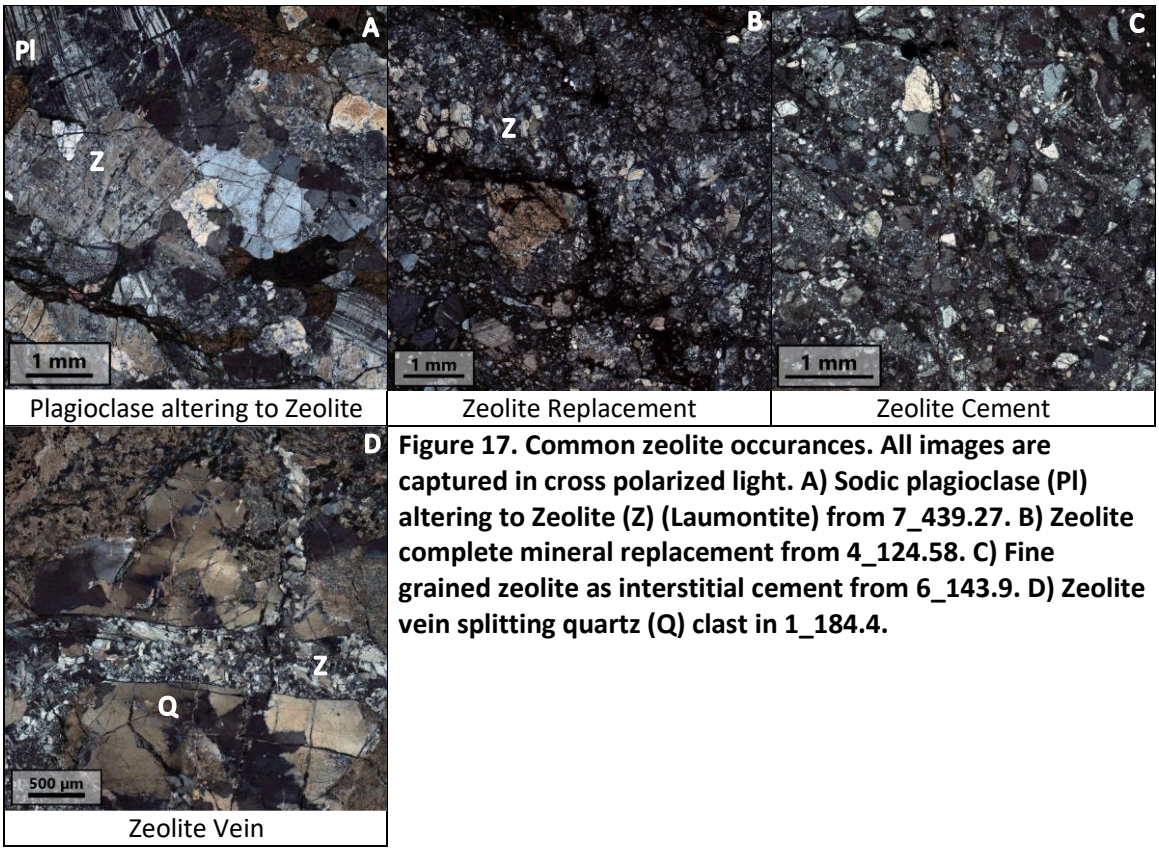

Figure 17. Common zeolite occurances. All images are captured in cross polarized light. A) Sodic plagioclase (Pl) altering to Zeolite (Z) (Laumontite) from 7_439.27. B) Zeolite complete mineral replacement from 4_124.58. C) Fine grained zeolite as interstitial cement from 6_143.9. D) Zeolite vein splitting quartz (Q) clast in 1_184.4.

4.3.2 Phyllosilicate Alteration

The primary phyllosilicate alteration identified is the chloritization of biotite (Fig. 15D) and muscovite (Fig. 13B), which is common both macroscopically and microscopically throughout much of the core. Chlorite group minerals occur in non-deformed and deformed biotite crystals, the largest of which range between 2-4 mm. Chlorite is more abundant in the increasingly fractured host rocks and is often localized around fractures (Fig. 15D). In amphibole-rich rocks, hornblende is commonly altered to biotite and chlorite.

Along with the alteration of phyllosilicates, clays, which appear subhedral and featureless, were identified in gouge materials through SEM imagery (Fig. 18). Scanning electron backscatter analyses identified the likely clay as smectite (Appendix 6), but more work needs to be done to identify the clay mineralogy.

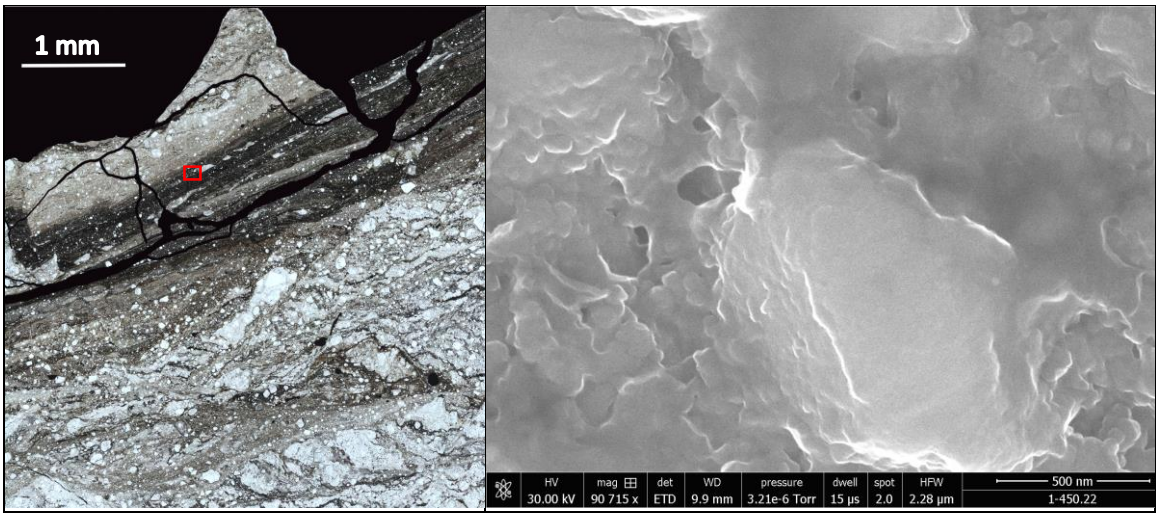

Figure 18. Authigenic clay growth in gouge materials. A) Plane polarized light optical image showing fine-grained, optically opaque matrix and distributed shearing in highly damaged quartzo-feldspathic wall rock. Red box denotes image B location. B) Scanning electron image of authigenic clay showing globular, poorly defined sheets.

4.4 Geochemical Analyses of Fault-Related Rocks

Whole-rock major, minor, and trace elemental geochemical analyses were performed on 46 samples with X-ray fluorescence and ICP-MS methods conducted by ALS, Inc. All samples collected from within the active fault zone and our analyses are supplemented by analyses of protolith to the north by Ross (1984) and to the south by Weschler et. al (2011) in order to provide us with analyses of protolith samples away from the highly deformed rocks. Major and trace element chemistries are expressed in oxide weight percentages and trace elements are in parts per million (ppm). The complete analytical results are in Appendix 8. Samples are classified as protolith, either quartzo-feldspathic or amphibolite, pulverized rock, fault-damaged rock, or gouge based on the macroscopic observations of relative damage previously described.

4.4.1 Quartzo-Feldspathic Protolith Geochemistry

We first establish the composition of protolith samples in our data set and compare our data with results from previous studies in order to verify the protolith classification of our samples. We use these protolith samples to identify the range of geochemical values which may have been incorporated into the fault zone at our site through fault displacement

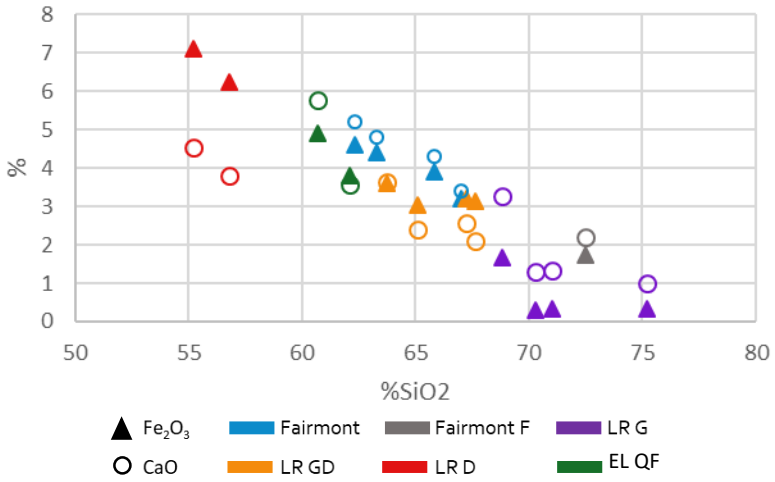

Figure 19. Comparison of quartzo-feldspathic protoliths from surrounding areas and Elizabeth Lake XRF data. Samples from this study (EL QF) are plotted against geochemical analyses of protolith rocks from previous studies conducted in nearby areas. Fairmont – Fairmont Reservoir, F – Felsic intrusion; LR – Littlerock Creek site, G – Granite, GD – Granodiorite, D- Diorite. Auxiliary data acquired from Fairmont Reservoir (Ross, 1984) and Littlerock Creek (Weschler et al., 2011). EL QF – Elizabeth Lake Quartzo-feldspathic protolith.

and fault-zone evolution. Establishing a protolith chemistry is then used as a baseline against which we compare the chemistry of the deformed rocks. The Fairmont data (Fig. 19) are from the Fairmont Reservoir granodiorite located within ~3 Km of our sample site (Ross, 1984) on the N. American plate. These data are split into granodiorites and a felsic intrusion (F) (Fig. 19). The Littlerock data were collected around Littlerock Creek (LR) ~45 Km south-southeast of our sample site (Weschler et al., 2011) on the Pacific plate. The LR data have been split into granite (G), granodiorite (GD), and diorite (D) (Fig. 19). In this project, we did not classify our samples in the same manner and instead grouped the quartzo-feldspathic rocks into one category. In order to match our data classifications, we combine the quartzo-feldspathic rocks into one group for each external site. We calculate the average and standard deviation of the Fairmont data and the Littlerock data without the LR diorite values included and incorporate these averages into our analyses as representative single data points. Protolith samples from the Elizabeth Lake core are most similar to the Fairmont granodiorite samples with the Elizabeth Lake samples containing slightly less silica when compared to the auxiliary data overall (Fig. 19). The bulk geochemical values of our samples fall well within the range of the Fairmont and Littlerock data averages (± 2 standard deviation), i.e. SiO_2 (67.68 ± 7.31), Fe_2O_3 (2.57 ± 2.96) and CaO (2.89 ± 2.59). In order to build a more robust dataset, and to capture protolith signatures from outside of our damage zone, the geochemical values for the Fairmont and Littlerock sites have been averaged by rock type and added to our geochemical analysis for comparison as quartzo-feldspathic protolith data points.

4.4.2 Whole-Rock Geochemistry of Fault-related Rocks

We analyzed our data as functions of both rock type and distance away from the inferred strand of the primary fault (IPFS) (Fig. 20). Samples were split into five rock types for analysis; 1. Quartzo-feldspathic (QF) protolith, 2. Amphibolite protolith, 3. Pulverized rocks, 4. Fault-damaged rocks, and 5. Gouge. These classifications are based on mesoscopic and microscopic observations discussed above. The bulk-rock geochemical compositions are calculated for each of the rock types (Fig. 21). The amphibolite is relatively silica poor, and Fe rich as compared to the other four rock types (Fig. 21). The fault damaged rocks and the gouge are compositionally more similar to the quartzo- feldspathic protolith than the amphibolite. Pulverized rocks have the highest average silica content (79.88 ± 9.69%) which agrees with our optically observed mineralogy (see optical microscopy section). There is a slightly higher abundance of iron-oxides within the fault-damaged rocks and gouge samples than in the quartzo-feldspathic protolith and pulverized rocks (Fig. 21).

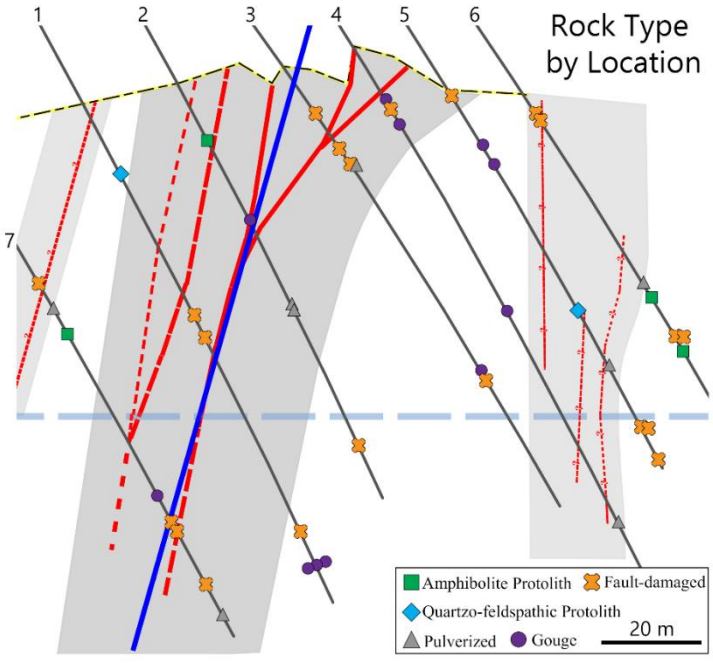

Figure 20. Geochemical sample location and rock type within the fault zone. Dark blue line represents the inferred primary fault strand. Light Blue dashed line is the Approximate Elizabeth Lake Tunnel. Boreholes labeled by core number. For full cross section image see Figure 3.

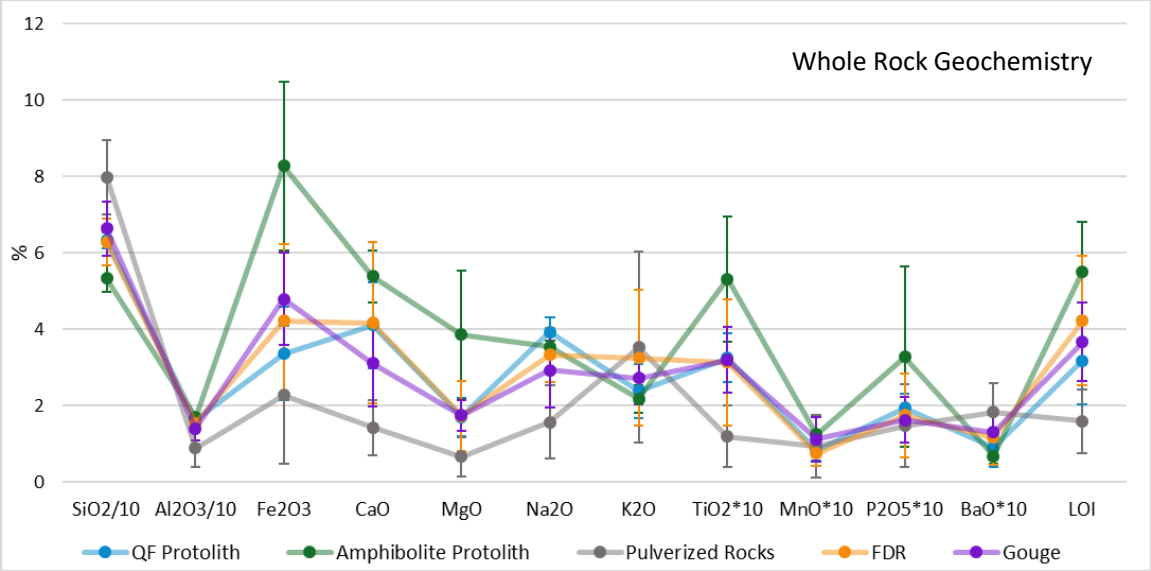

Figure 21. Average compositions of rock types. Bars represent one standard deviation. The QF protolith, FDR, and gouge track most closely to each other while the amphibolite protolith and the pulverized rocks tend to vary more.

Trace and rare earth element data track rather closely for all rock types (Fig. 22). Variations in Ba and Sr concentrations might be related to calcite and/or zeolite mineralization (Forand et al., 2017; Crouch and Evans, 2019) within the deformed rocks. The most prominent deviations are observed within the pulverized rocks but further work is needed to quantify any statistical significance these deviations may represent. The trace elements with the highest measured abundance are barium and strontium followed by tungsten, zirconium, vanadium, and rubidium. Calcite was identified within the samples through optical microscopy and as carbonates often incorporate Ba and Sr within the crystal lattice, may be a source of the elements.

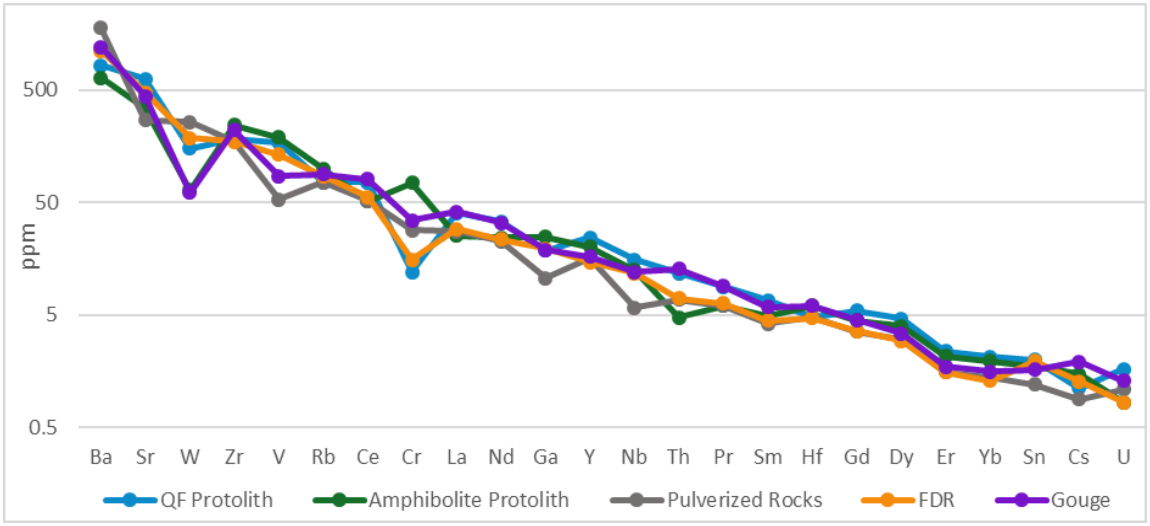

Figure 22. Trace element data for each rock type. Graph shows the average ppm for each trace element by rock type classification. Ppm data are plotted on a logarithmic scale.

4.3 Geochemical Signatures Analyzed as a Function of Distance

We normalized our data to the inferred primary fault strand (Fig. 20) and plotted our samples as a function of distance away from the IPFS to identify any possible spatially related geochemical trends. No clear trend exists between the whole-rock data and the sample distance from the main fault zone (Fig. 23). While individual rock types plot within similar compositional ranges, these variations do not appear to be tied to distance.

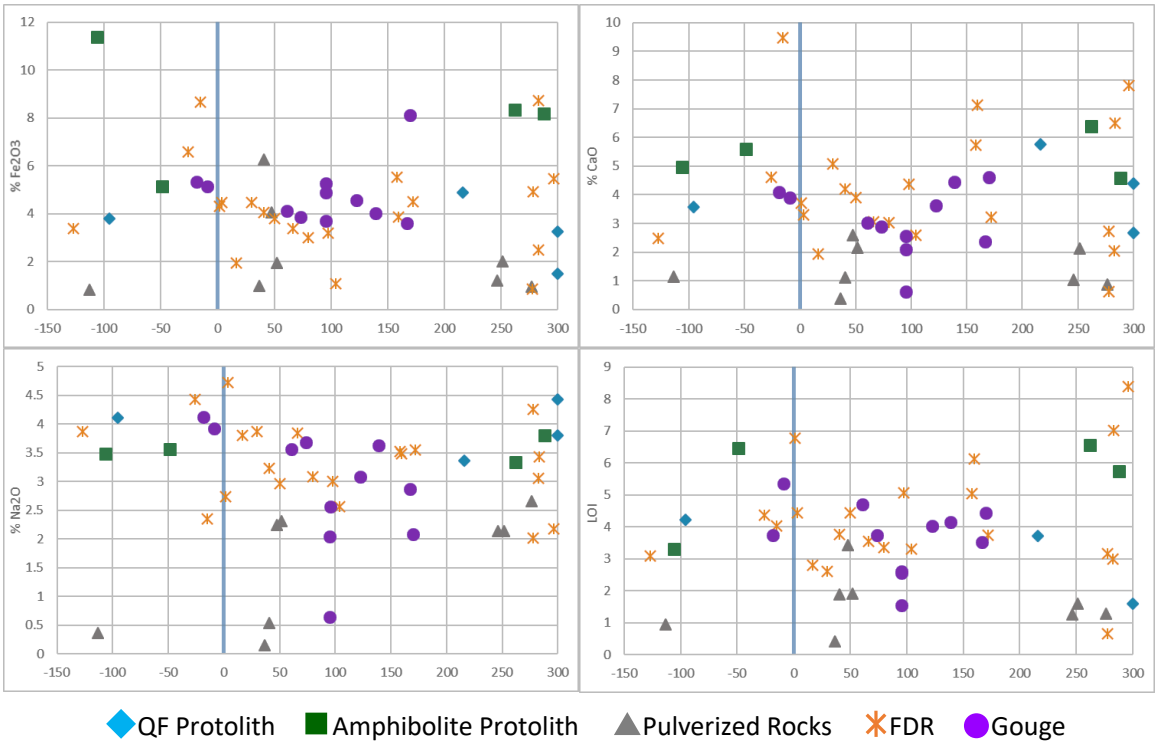

Figure 22. Geochemical data plotted as a function of distance from the IPFS. Negative values reside on the Pacific plate and positive values are from the N. American plate. (Distance is measured in feet). Blue line represents the IPFS.

We plotted the data by sample location within the fault zone in order to analyze the geochemical relationship to the fault damage zones and core (Fig. 24). The Pacific plate side of the fault zone appears to have a relatively higher Na_2O content than the North American plate side (Fig. 24B). There does not appear to be a geochemical signature associated with the sample proximity to the identified faults or the inferred damage zones.

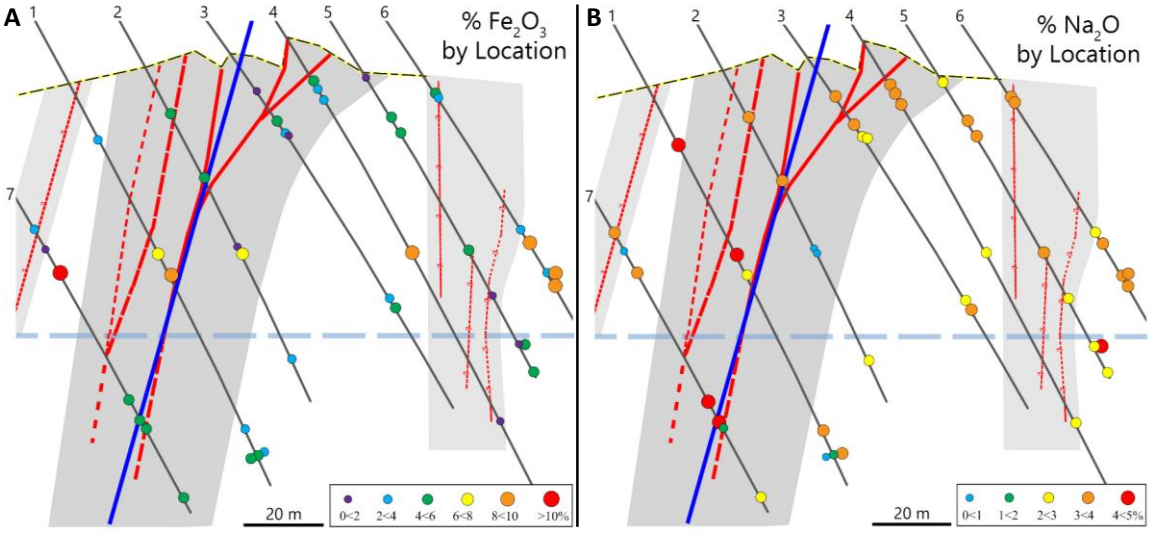

Figure 24. Binned geochemical data distribution within the fault zone. A) Percent Fe_2O_3 by sample location. B) Percent Na_2O by sample location. Circle size increases and colors become warmer with increasing value. See methods section Figure 3 for full cross section key.

4.4.4 Statistical Analyses of Major Element Data

We plotted the major element data as a function of elemental weight percent compared to silica content for each rock type (Fig. 25). Possible trends are the high silica content of the pulverized rocks and the low silica content of the amphibolite rocks. Using a bootstrapping statistical analysis (Sohn and Menke, 2002), we calculated the 90% confidence intervals for the major elements of each rock type (Fig. 26). Compositionally, there is a significant difference between the pulverized rocks and all of the other fault rock groups. The amphibolite protolith is similarly significantly different in composition. Pulverized rocks are unique in their extremely high silica content with some samples as high as 96% resulting in relative depletions of the other major element concentrations. The pulverized rocks also show slight overlap with the gouge samples in Na_2O weight percent and in LOI with the quartzo-feldspathic protolith. Another significant difference is that the Fe_2O_3 content is relatively enriched in the gouge samples as

compared to the quartzo-feldspathic protolith with no overlap at the 90% confidence interval (Fig. 26B).

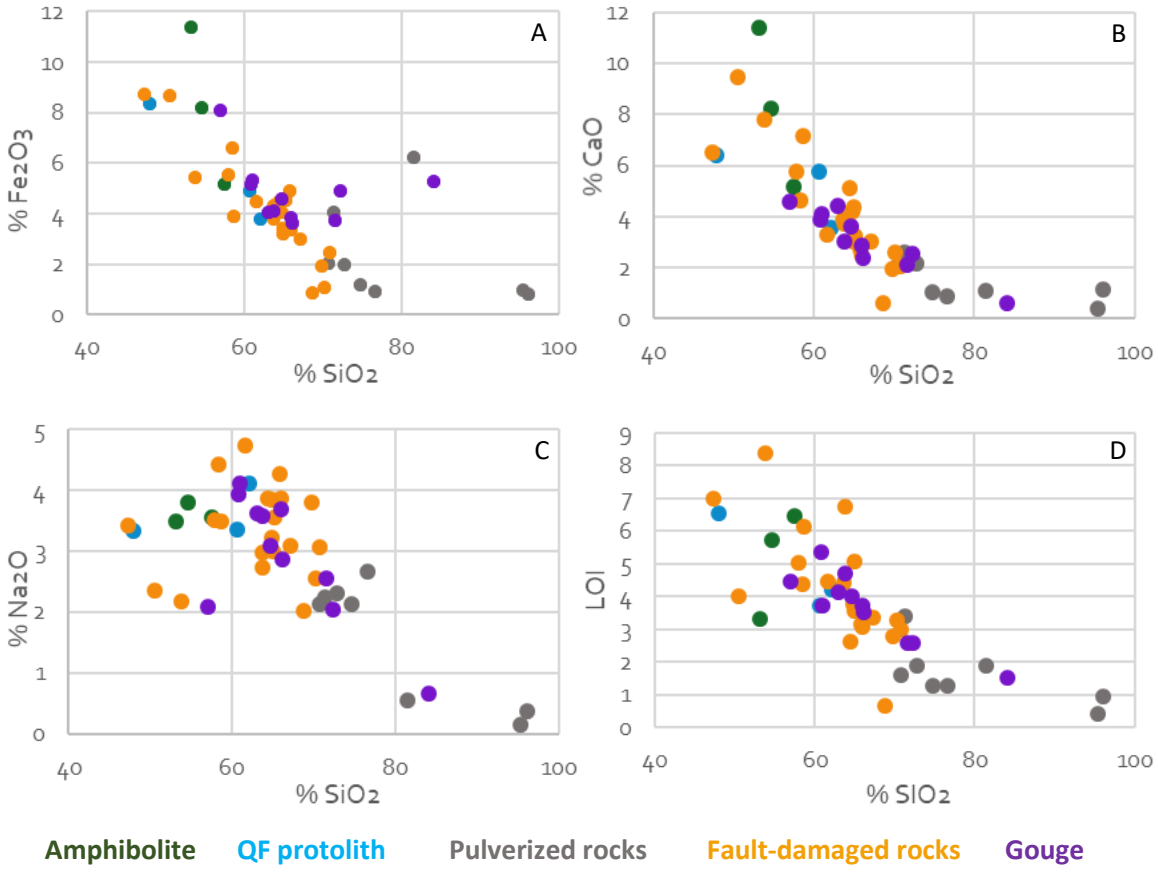

Figure 25. Whole-rock major element data by rock type. Pulverized rocks have relatively high silica contents and amphibolite rocks have relatively low silica contents. A) Fe_2O_3 by SiO_2. B) CaO by SiO_2. C) Na_2O by SiO_2. D) LOI Fe_2O_3 by SiO_2.

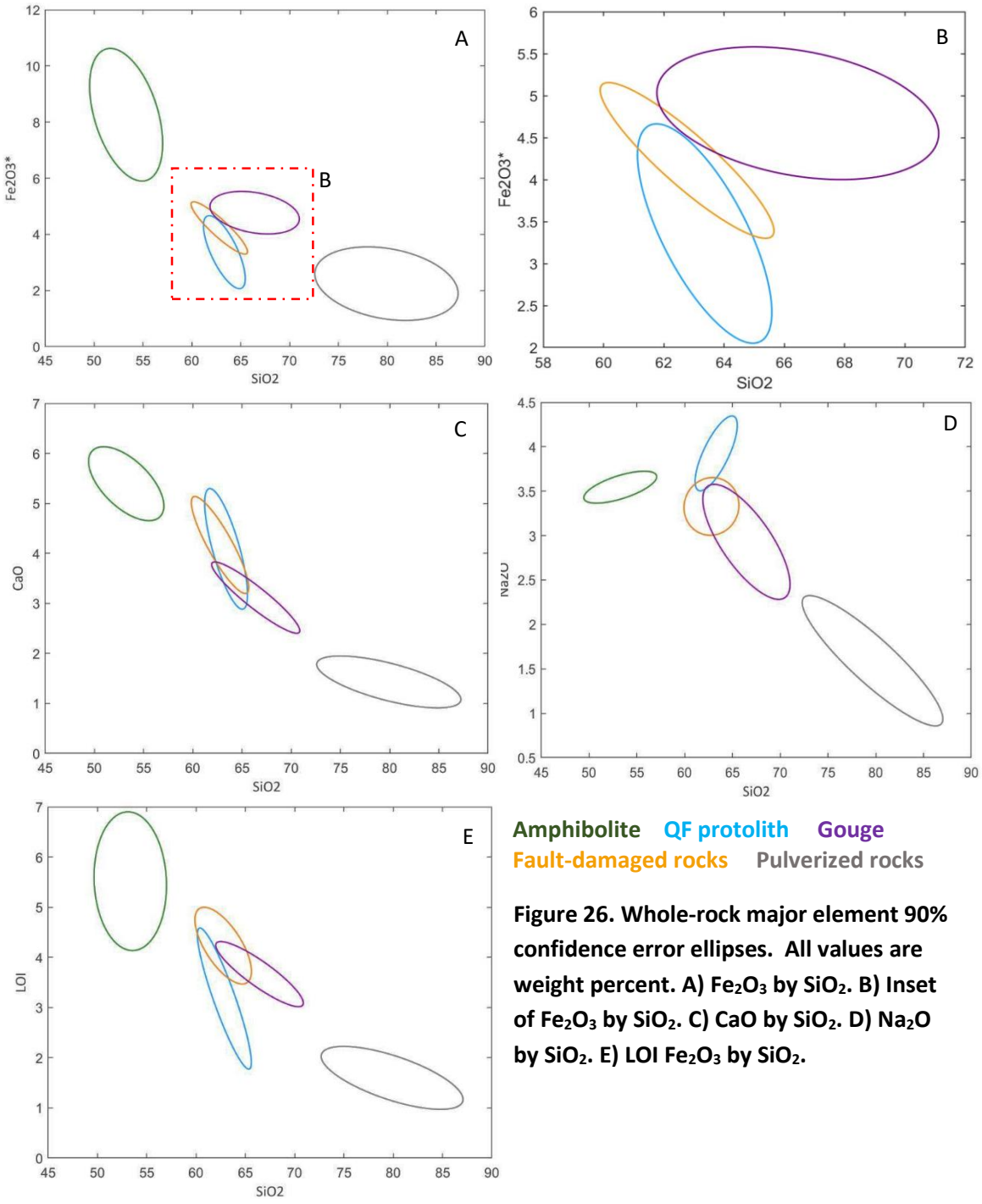

Figure 26. Whole-rock major element 90% confidence error ellipses. All values are weight percent. A) Fe_2O_3 by SiO_2. B) Inset of Fe_2O_3 by SiO_2. C) CaO by SiO_2. D) Na_2O by SiO_2. E) LOI Fe_2O_3 by SiO_2.

Overall, our geochemical analyses do not provide ample evidence of depletion or enrichment in major, minor, or trace elemental compositions with the exception being the

pulverized rocks unique geochemical composition and the Fe_2O_3 composition of the gouge samples as compared to the quartzo-feldspathic protolith. Distance away from the fault does not appear to significantly impact the geochemical signature of the samples as heavily as the degree of deformation and rock type classification.

4.5 Textural Evidence of Slip Rates

4.5.1 Evidence of Coseismic Slip Velocities

We identified four seismically generated textures throughout the fault damage zone. The most common of these is that of pulverized rock which is identifiable at the mesoscopic scale, followed by injection veins, core/clay-clast aggregates, and pseudotachylyte which are identifiable at the microscopic scale. Following the broader classification for pulverized rock laid out by Rempe et al. (2013), pulverized, and or pulverized and sheared rock, was identified in 22 thin sections (Fig. 27A). Fault gouge injection veins were identified in 34 thin sections (Fig. 27B) and core/clay-clast aggregates were identified in 27 thin sections (Fig. 27C). Pseudotachylyte was identified once in thin section 1-289.05 by its distinctive melt texture (Fig. 27D). These features will be discussed in detail in the interpretation sections 5.1.1-5.1.5.

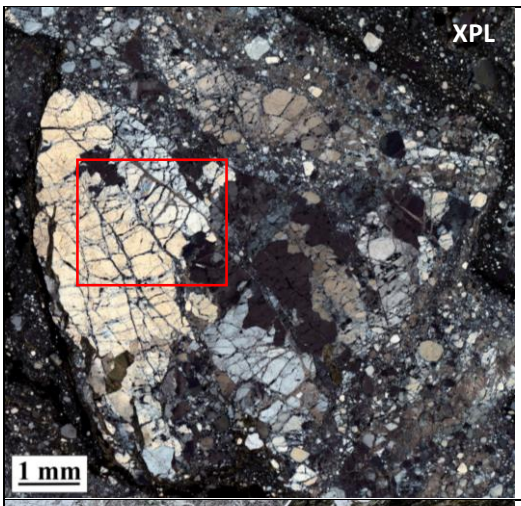

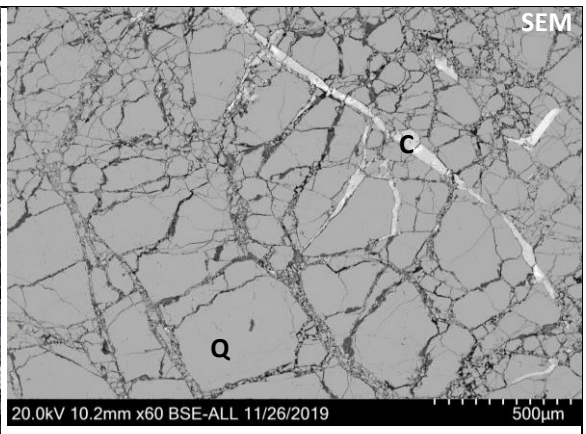

A) Pulverized Rock
2-285.5

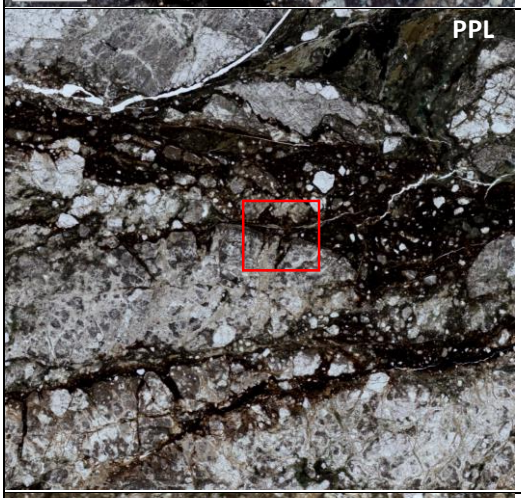

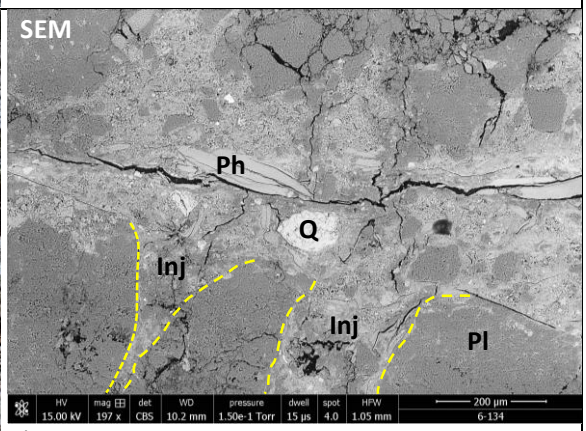

B) Injection Veins
6-134.7

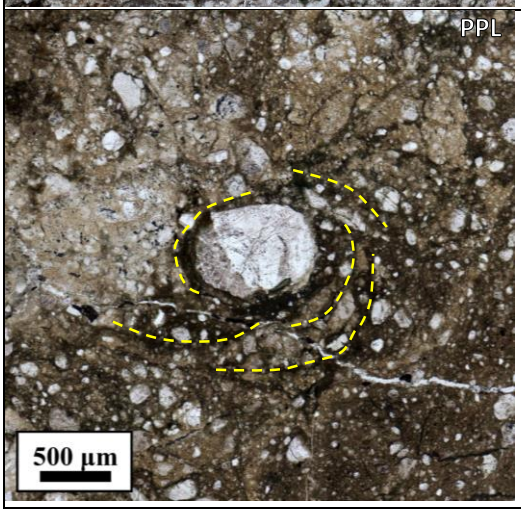

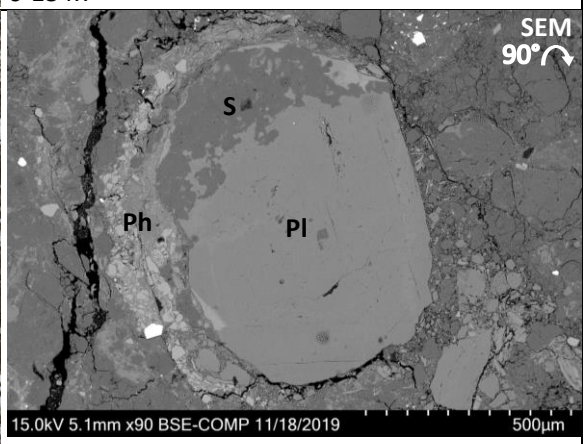

C) Clay-Clast Aggregate
4-140.18

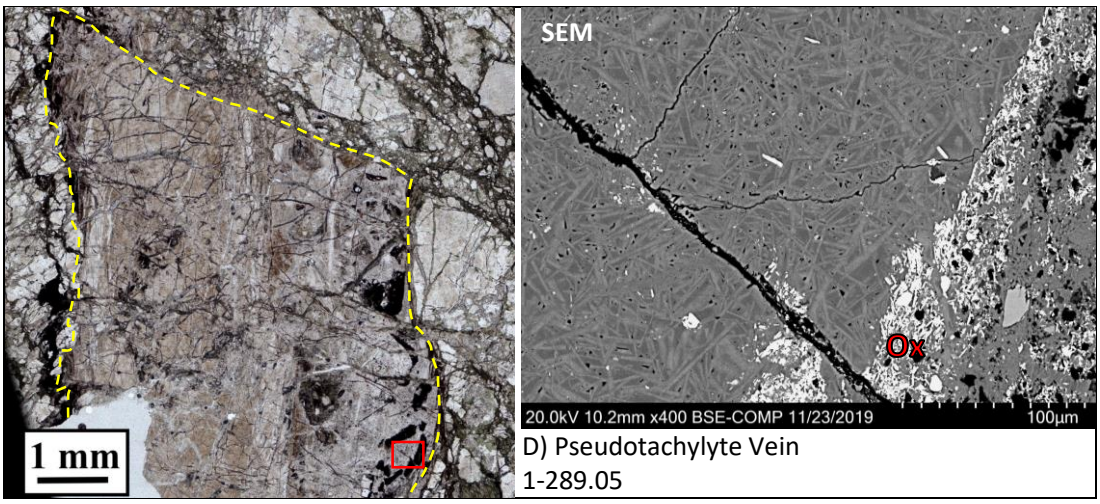

Figure 27. Coseismic indicators identified through optical microscopy. A) Pulverized quartz (Q) clast filled with calcite cement (C) and entrained within a fine grained cataclasite. Red box denotes SEM image location. B) Optically opaque, fine-grained cataclasite injected into altered plagioclase (Pl). SEM image shows granular injection veins (Inj) containing cataclasite comprised of clasts of quartz (Q), phyllosilicates (Ph), and plagioclase (Pl). C) Core Clast Aggregate in fine grained, clast rich cataclasite. Plagioclase core (Pl) altering to sericite (S) with a phyllosilicate (Ph) and auxiliary mineral rim with concentric circles of matrix (yellow dashed). D) Pseudotachylyte vein (dashed yellow lines) displaced by a crosscutting cataclasite. Red box denotes SEM image showing characteristic melt texture and clustered oxides (Ox).

4.5.2 Evidence of Aseismic Slip Velocities

We identified three deformation textures indicative of aseismic slip rates; calcite twinning, dilatant vein fill, and mineral replacements. The twinning of calcite provides evidence for strain accumulation and plastic deformation within the crystal structure (Fig. 28A) (Debreser and Spiers, 1997; Ferrill et al., 2004). Dilatant vein fill, most commonly identified in zeolite (Figs. 28B and 28C) and calcite veins (Fig. 28C), displays a lack of sheared displacement between intragranular fractures with vein fill crystal morphologies indicating progressive, extensional growth (Blenkinsop and Sibson, 1992, Bons et al., 2012). The mineral replacement of plagioclase by zeolite can result in up to a 60% molar volume increase (Blenkinsop and Sibson, 1992) and result in aseismic expansion.

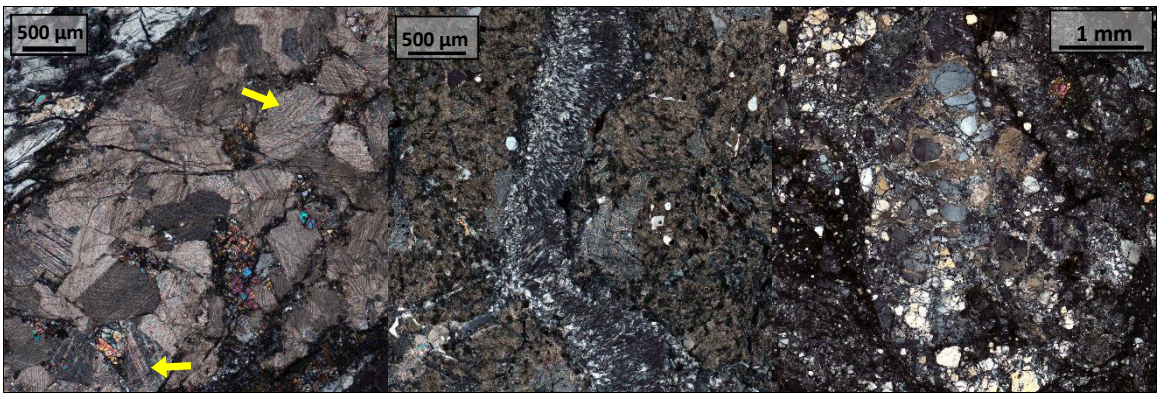

Figure 28. Aseismic indicators identified through optical microscopy. A) Calcite twinning with thick twins identified by yellow arrow. B) Antitaxial, fibrous zeolite vein growth with equant grains along the left side of the vein and elongated grains through the center. C) Calcite and zeolite intragranular, expansion veins. Quartz clasts showing slight rotation and displacement with zeolite veins cross cut by calcite veins.

5. INTERPRETATIONS

5.1 Cross-Cutting Relationships of Key Deformation Structures

In this section, we provide in-depth observations and correlated interpretations of key deformation structures identified primarily through our petrographic work. We provide a brief introduction to each structure to describe the specific deformation textures. These key deformation microstructures are observed commonly throughout our petrographic samples, with the exception of pseudotachylyte. We report the interpreted minimum number of deformation events from the observed cross-cutting relationships in each thin section and comment on the textural evidence these deformation structures provide. We highlight how these key deformation structures are formed and how they are interpreted to impact the fault zone processes. These interpretations are conservative estimates due to the complexity of the observed cross-cutting relationships. It is possible, and likely, that more events have occurred. While we present our interpretations within the resolution of a single, standard thin section and associated core sample, the deformation structures highlighted in this section are common throughout the fault damage zone with the exception of pseudotachylyte. We observe textures indicative of both coseismic and aseismic slip mechanisms within these samples and sometimes within the same thin section. The relationships of the deformation structures and the alteration textures we identify allow us to evaluate the interplay of coseismic and aseismic processes active within the fault zone. Here, we are able to report alternations between coseismic and aseismic slip mechanisms over the mm to cm scale.

5.1.1 Clay-Clast Aggregates

Clay-clast aggregates (CCA), sometimes referred to as clast-cortex or core-clast aggregates, are microstructures that result from coseismic deformation. These form when thermal pressurization increases the pore fluid pressure and dilates the fault (Boutareaud et al., 2010). Dilation creates space for grains to roll within the phyllosilicate rich fault gouge. Within a fluidized granular flow, the rolling clast "snowballs" within the gouge as differential electron charges bind a rim of fine grained material to the clast (Boutareaud et. al., 2010; Rowe and Griffith, 2015). There is some experimental evidence which suggests they may form at slip rates from 1 m/s down to 0.5 mm/s (Han and Hirose, 2012), a range of slip rates that only occurs during earthquakes (Rowe and Griffith, 2015). Han and Hirose (2012) found that CCAs only formed in experiments at low normal stress and suggested that there might be a depth limit to forming them in natural faults. Although these have been more recently referred to as CCA's, they may have been identified previously in the exhumed San Gabriel Fault as conglomerated grains, which were found in relation to other coseismic textural indicators (Chester et al., 1993).

Figure 29. Core image for thin section 4_140.18. Thin section location denoted by yellow box.

Our type example of a CCA comes from a core sample characterized by fine grained, grey-brown gouge with isolated, rounded clasts up to ~5 mm within an oriented shear fabric (Fig. 29). We divide this thin section (Figs. 30A and 30B) into two regions: a fine grained gouge (uphole) and a moderately-damaged, highly-altered wall rock (downhole) (Fig. 30C). To interpret the cross cutting relationships of this thin section, sheared bands within the

uphole gouge are labeled with roman numerals while evidence for interpreted deformation events are labeled with Arabic numerals.

We interpret three to four deformation events recorded in the downhole half of the sample (Fig. 30). The first is an early stage of wall rock fracturing and displacement (clasts colored dark grey in Fig. 30C, 1) followed by an alteration phase as indicated by the zeolite replaced clasts (clasts colored grey blue in Fig. 30C, 1a) and intra-clast calcite veins. A subsequent 1-2 cataclastic shear events, as indicated by the cataclasite which bound both sides of the wall rock clasts (Fig. 30C, 2, 2a), may have facilitated some iron-oxide alteration into the damaged rocks. A cross-cutting fracture displaced the rock fragments and cataclasites (Fig. 30C, 3). Within the downhole half of the thin section, the presence of zeolite replacement textures and cement indicate a hydrothermal alteration event (Fig. 30C, 4). This alteration indicates a healing phase that was crosscut by the banded gouge in the uphole half of the thin section, which is zeolite-free.

The banded gouge in the uphole side of the thin section is comprised of six distinct bands based on changes in clast density and mineralogy, and conservatively represents two rupture events. The finest grained (I) band contains grains measuring < 100 μm at a proportion of < 5%, and a relatively higher proportion of phyllosilicate grains. Band I also appears as a deeper red-brown in plane polarized light. The next band (II) contains a higher proportion (≤ 10%) of grains measuring close to ~100 μm and is a lighter red-brown in plane polarized light. The contact between (I) and (II) is weakly undulatory and gradational with no clear cross-cutting relationship. These two bands are cut by a web of fine, spidery veins of an unidentified colorless mineral. The contact between (II) and (III) is gradational and wavy. A clast proportion closer to ~40% with grains measuring up to ~500 μm characterizes band (III). In plane polarized light, the

matrix of band III is a lighter tan-brown. The contact between (III) and (IV) is sharp and strongly wavy, defined by a change in clast size and the optical matrix color. Band IV contains a clast proportion of ~30% with a similar proportion of larger ~500 µm grains, but fewer 100-200 µm grains as compared to band III. The matrix of IV is also a darker brown in plane polarized light. The next band (V) contains a clast density of ~40% with the largest grains measuring ~ 1 mm and a somewhat disaggregated cemented matrix which appears as a light, tan-brown in plane polarized light (V). This band (V) may record evidence for a paleoearthquake, as it contains a well-defined clay-clast aggregate (Fig. 30D) with a plagioclase core and accreted phyllosilicate and auxiliary mineral rim. The gradational nature of bands I-V conservatively represents a single slip event (5). Band V is sharply cut along a smooth contact by band (VI) which is the only one of the gouge layers to contain a strong parallel fabric defined by color banding in the brown matrix. The oriented fabric, lack of cement, and smaller clast size within VI and its well defined contact with V, as well as the contact with the downhole half of the thin section indicate a final rupture event (6).

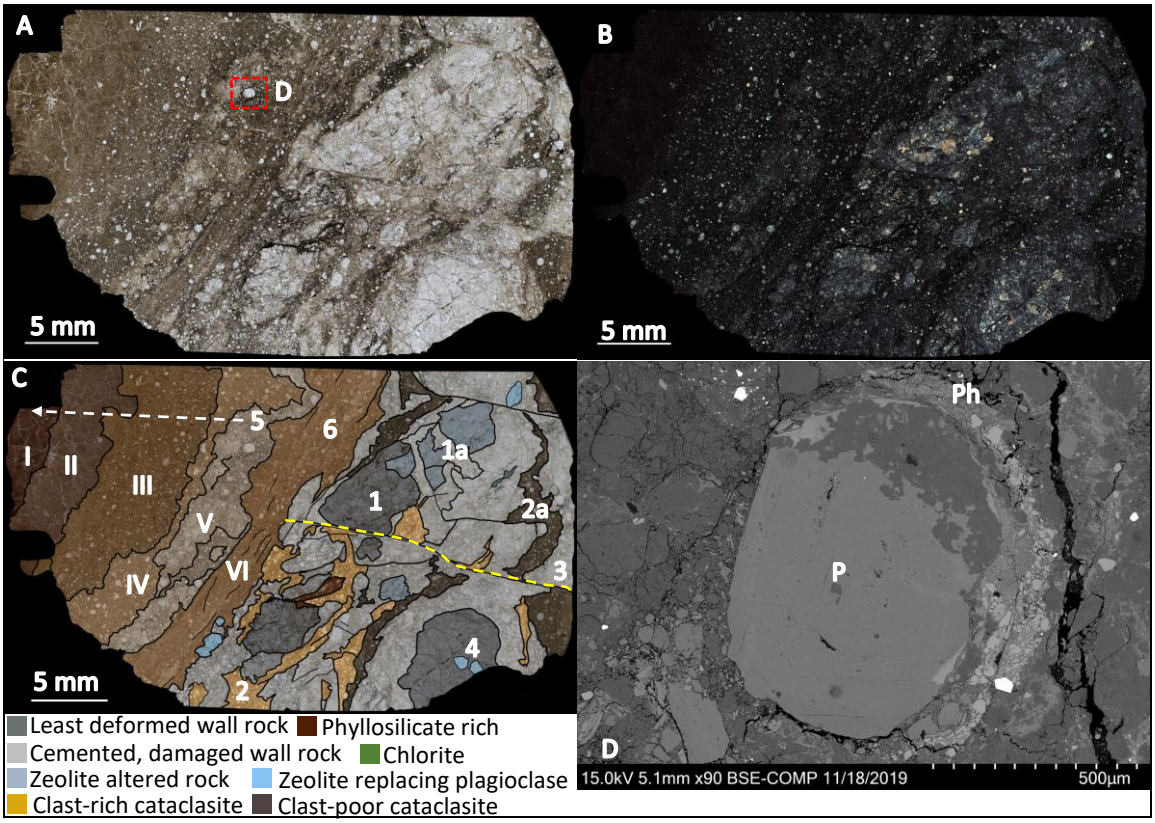

Figure 30. Clay-clast aggregate in banded gouge. A) Thin section in plane polarized light showing fine-grained banded gouge to the left (uphole) and moderately damaged and cemented fault rocks to the right (downhole). Red box denotes image location for D. B) Thin section in cross polarized light. Note: the uphole optically opaque matrix is due to the very fine-grained nature of clasts. Optically yellow clasts are quartz in a grey-blue, zeolite altered clast. C) Mapped thin section showing deformation zones. Color key for downhole half only, uphole cataslcastic bands are shaded only for emphasis. Yellow dashed line indicates shear surface for event 3. White dashed arrow indicates zone of deformation event 5. Roman numerals indicate cataclastic bands classified by clast density and mineralogic changes. Arabic numerals indicate sequential deformation events. D) Scanning electron image of a clay-clast aggregate. The plagioclase (P) core is altered and rimmed by phyllosilicates (Ph) and entrained fine gouge particles.

This sample is located within the primary damage zone on a subsidiary branch of the main fault, ~22 m from the inferred primary fault strand (Fig. 7). The deformation and alteration textures identified in this thin section record variable slip velocities and phases of fault healing processes over multiple earthquake cycles. The CCAs provide evidence of coseismic slip while the banded gouge and cataclastic shear zones record rupture events with non-specific slip rates.

The zeolite mineral replacements, iron-oxide alteration, and observed cementation indicate repeated healing and fluid-assisted mineral alteration phases.

The process of thermal pressurization and fault zone dilation is self-limiting. Coseismic slip rates are required in order to generate the frictional heat that results in the fluid vaporization and fault zone dilation (Boutareaud et al., 2010). As slip and displacement continue, the volume of dilated rock increases which counteracts pressurization and may inhibit continued dilation (Rempel and Rice, 2006). Longer slip distances encourage the dissipation of heat and fluids into the surrounding rocks (Rempel and Rice, 2006). Therefore, with continued displacement along the slip surface, the continued rupture itself possibly prevents the continued formation of clay-clast aggregates.

5.1.2 Injection Veins

Injection veins are off-fault tensile fractures filled with fault-related rock injected at high angles off the slip surface, which formed through dynamic rupture processes; therefore, they serve as indicators of co-seismic slip (Lin, 1996; Ngo et al., 2012; Rowe et al., 2012; Rowe and Griffith, 2015). Fluidized-granular materials injected at high angles into the wall rock have been identified throughout the fault damage zone.

The core from which this thin section sample was taken (Fig. 31) is a medium-grained, moderately to highly damaged quartzo-feldspathic rock cut by a foliated, fine-

Figure 31. Core image for thin section 6_134.7. Arrow points uphole and yellow box denotes thin section location.

grained gouge and multiple oxide-rich shear bands. This thin section (Figs. 32A and 32B) is split into three distinct zones; the uphole unit (U_u), the central unit (C_u), and the downhole unit (D_u) (Fig. 32C). The overall shear direction of the overarching structure, based on the relationships between the foliations within the cataclasite and the angles of the injection veins (Fig. 32D), is that of the top to the left and the bottom to the right.

The upper unit (U_u) is relatively undamaged with oriented phyllosilicates (Fig. 32), and quartz fabrics indicative of dislocation glide which likely formed prior to the onset of brittle faulting and are therefore considered inherited wall rock textures rather than earthquake or recent -related deformation textures. The plagioclase grains exhibit a highly altered sericitic alteration texture but maintain their shape and contacts.

The central unit (C_u) is a fine-grained foliated cataclasite to ultracataclasite with plagioclase clasts that have been replaced by zeolite. This alteration appears to have been facilitated by intra-granular fracturing and an influx of pore fluid as the fractured grain rims are more altered than the grain cores. There are also minor calcite veins within some of the clasts (Fig. 32). The cataclasite has sharp sheared contacts with the upper and lower units and has a matrix that is ultra-fine grained, optically opaque, and can be seen as injected fluidized cataclasite within the foliated clasts (Fig. 32E).

The downhole unit (D_u) is a moderately to highly brecciated granodioritic fault-rock with portions that have been cataclastically sheared (Fig. 32). There is also iron-oxide alteration evident in the plane polarized image as the cataclasite in contact with the central unit is tinted red-brown. This lower zone has minor evidence of zeolite and calcite alteration.

This thin section contains evidence for at least 6 deformation events (Fig. 32D). Within the relatively undamaged uphole unit (U_u), there is evidence for two fracture and vein-fill

events. Overprinting the relic quartz fabrics are zeolite veins (1) which have been subsequently cut by calcite veins (2) representing two different fracturing events in the presence of different pore fluids. The downhole unit (D_u) contains evidence for at least three events. The brecciation and shearing of the wall rock conservatively represent at least one phase of brittle deformation (3). The increased permeability in the brecciated wall rocks allowed for small amounts of mineral precipitations, which helped the clasts to regain some inter-grain strength and for the iron-oxide alteration to occur. The sharpness of the fracture contact between the cataclastic shear zone (4) and the brecciated fabric (3) indicates a cemented matrix within D_u. Event 4 is bound within the brecciated and cataclastically sheared D_u and is partially sheared into the fine-grained, optically opaque matrix of the C_u's foliated cataclasite. In the C_u, there was an early stage of deformation (5) and subsequent zeolite alteration along the intra-granular fractures. This zeolite alteration likely acted as a cementation or healing phase as indicated by the presence of injection veins filled with oxide-rich ultracataclasite along the uphole rims of the altered clasts (Fig. 32E). The injection veins cut through the altered plagioclase and zeolite cements and do not appear to have utilized pre-existing fractures. A final slip event (6) is identified in the C_u by the foliated cataclasite and related injection veins. The foliated cataclasite cuts all other observed fabrics and is interpreted as the final deformation event recorded in this thin section which juxtaposed the three units and likely created the sharp fracture which cuts into the center of D_u. Top to the left shearing allowed for the formation of the foliations within the cataclasite as P shears and the formation of the injection veins as high angle T shears.

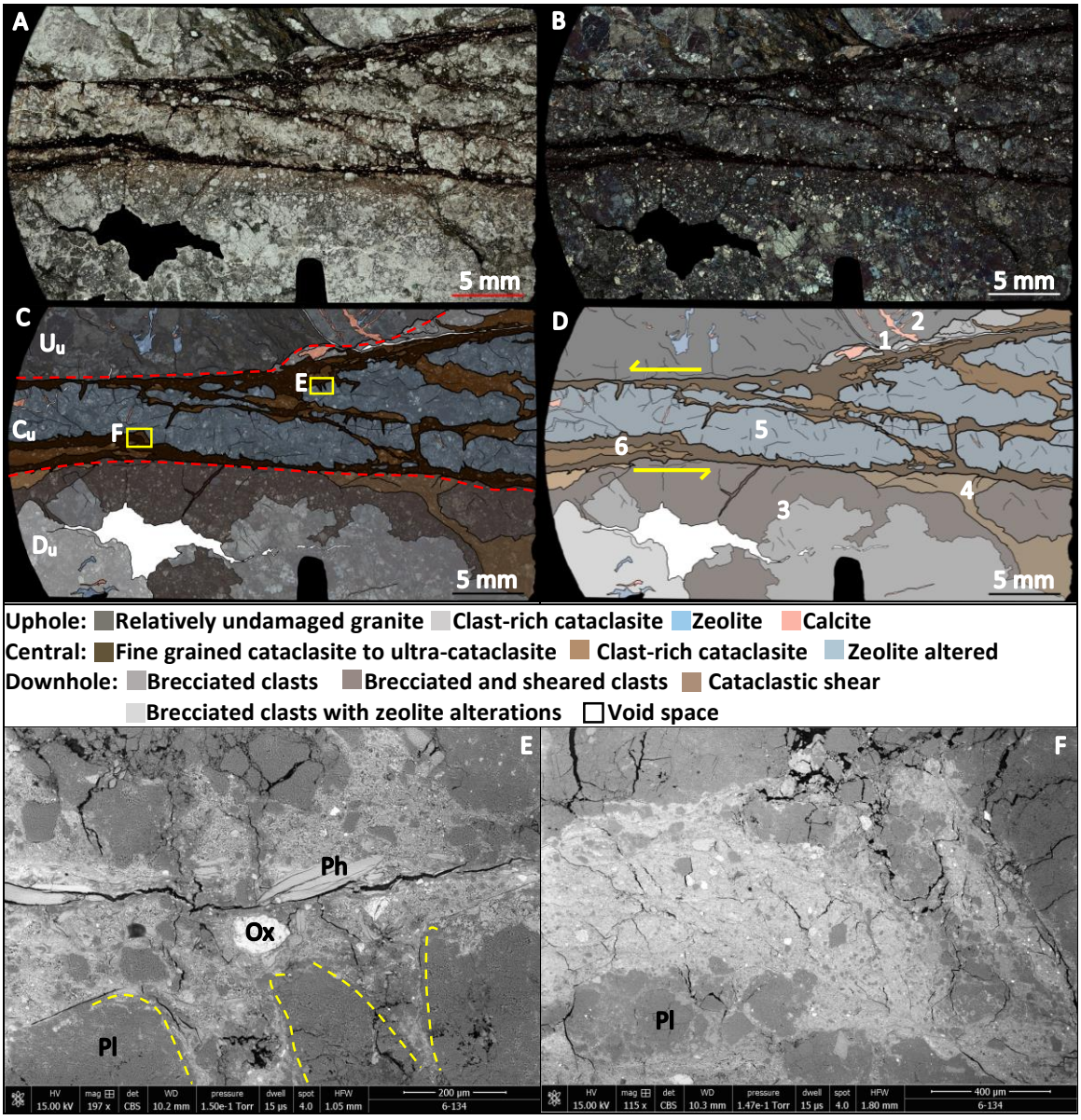

Figure 32. Cross cutting relationships in foliated cataclasite with injection veins. A) Plane polarized optical image of thin section. B) Cross polarized optical image of thin section. C) Zoned and colored map of thin section with yellow boxes denoting SEM image locations for E, F. D) Mapped thin section. Yellow arrows indicate shear orientation. E) SEM imagery of injection veins outlined in yellow. Phyllosilicates = Ph, Iron-oxide = Ox, Plagioclase = Pl. F) SEM imagery highlighting the fine grained nature of the optically opaque gouge materials.

This sample is located ~48 m from the IPFS within the secondary damage zone on the N.A. plate side of the fault structure (Fig. 7). We observe evidence for variable slip velocities, mineral alterations and cementations, and multiple rupture events. Injection veins record

evidence for a coseismic slip event while the cataclastic and brecciation textures are indicative of non-specific slip velocities. The zeolite replacement and the calcite and zeolite veins provide evidence for multiple fluid-assisted alteration phases. These three units were likely formed relatively independently from one another and were juxtaposed through subsequent deformation and displacement.

Injection veins form as tensile, off-fault cracks during coseismic deformation events (Ngo et al., 2012; Rowe and Griffith, 2015). In order to achieve the tensile stresses required to propagate these fractures, the surrounding rocks must possess a certain amount of internal strength. If the wall rocks through which the rupture propagates are too weak, it is unlikely for injection veins to occur. In detailed microstructural analyses, the presence of injection veins within highly damaged or altered materials may be indicative of previous phases of healing.

5.1.3 Phyllosilicate Linkage

Phyllosilicates are often characterized by their weak strength and low-frictional behavior (Behnsen and Faulkner, 2012; Lockner et al., 2011) due to their sheeted crystal structure. Shear zones, which concentrate shear strain within foliations defined by the weakest mineralogies, can control the overall slip behavior (Behnsen and Faulkner, 2012; Colletini et al., 2009; Lockner et al., 2011). An aligned, interconnected system of phyllosilicate foliations can significantly weaken a fault zone (Neimeijer and Spiers, 2005), even at low abundances (Collettini et al., 2009) and thus change the slip behavior of the shear zone.

At the mesoscopic level, core sample 2_320.4 exhibits a highly damaged, fine-grained quartzo-feldspathic rock with oxide-lined webbed fractures (Fig. 33). The sample has an overall oriented fabric created by the high density of fractures. There is light iron-oxide alteration, but no other major indicators of alteration.

Figure 33. Core image for thin section 2_320.4. Thin section marked by yellow box.

Within this type sample, we identify the deformation textures associated with webbed fracturing – a very high density of small fractures which deform the rock over a volume of space but have distinct slip surfaces, as well as the apparent role of phyllosilicates within these shear zones. In thin section (Figs. 34A-C), the sample is composed of predominantly quartz, muscovite, and iron oxides with minor titanite and chlorite. The sheared fabrics in this rock are generally parallel at a high angle to the core axis (Figs. 34A-D) and often exhibit phyllosilicate lined shear surfaces (Fig. 34E). Relatively cohesive clasts (Figs. 34C-E), as compared to the remainder of the sample, contain intra-granular fractures oriented at a high angle to the shear direction which cuts roughly 20-30° off from parallel with the core axis (Figs. 34D and 34E). These larger, less damaged clasts are typically lined by relatively more intact phyllosilicate crystals and oxides (Figs. 34E and 34F). The high angle, intra-granular fractures within the larger clasts (Figs. 34E and 34F) are likely tensile cracks which propagated through the crystals during slip. The phyllosilicates lining the larger clasts are often oriented with the slip direction (Figs. 34E-H). Through SEM photography (Figs. 34F-H), we identify the deformation habits of fault bend propagation folds (F), kinks (H), and slip localization (G, H) within the phyllosilicate crystals.

There is evidence for at least 3 deformation events within this type sample. We interpret an early deformation event that formed the roughly core-parallel oriented fabric and created the high density of sheared surfaces (Fig. 34D, 1). A slip zone defined by oxide-rich shear surfaces (Fig. 34D, 2) lies within the oriented fabric of event 1 and may have occurred contemporaneously. We conservatively interpret this as port of event 1 as slip behavior may change over the course of one deformation event. The second definitive event is that of the cross cutting shear zone which lies at a high angle to the core fabric (Fig. 34D, 3) and appears to have dragged, offset, and reoriented some of the pre-existing foliation. A subsequent localized deformation event measuring ~250 μm in width (Fig. 34D, 4) offsets the core perpendicular shear and the larger clast identified in Fig. 34E. A second cross cutting shear, which is similar in orientation to event 4, is identified offsetting the oriented fabric of event 1, but appears to dissipate within the central mass of the thin section (Fig. 34D, 4a).

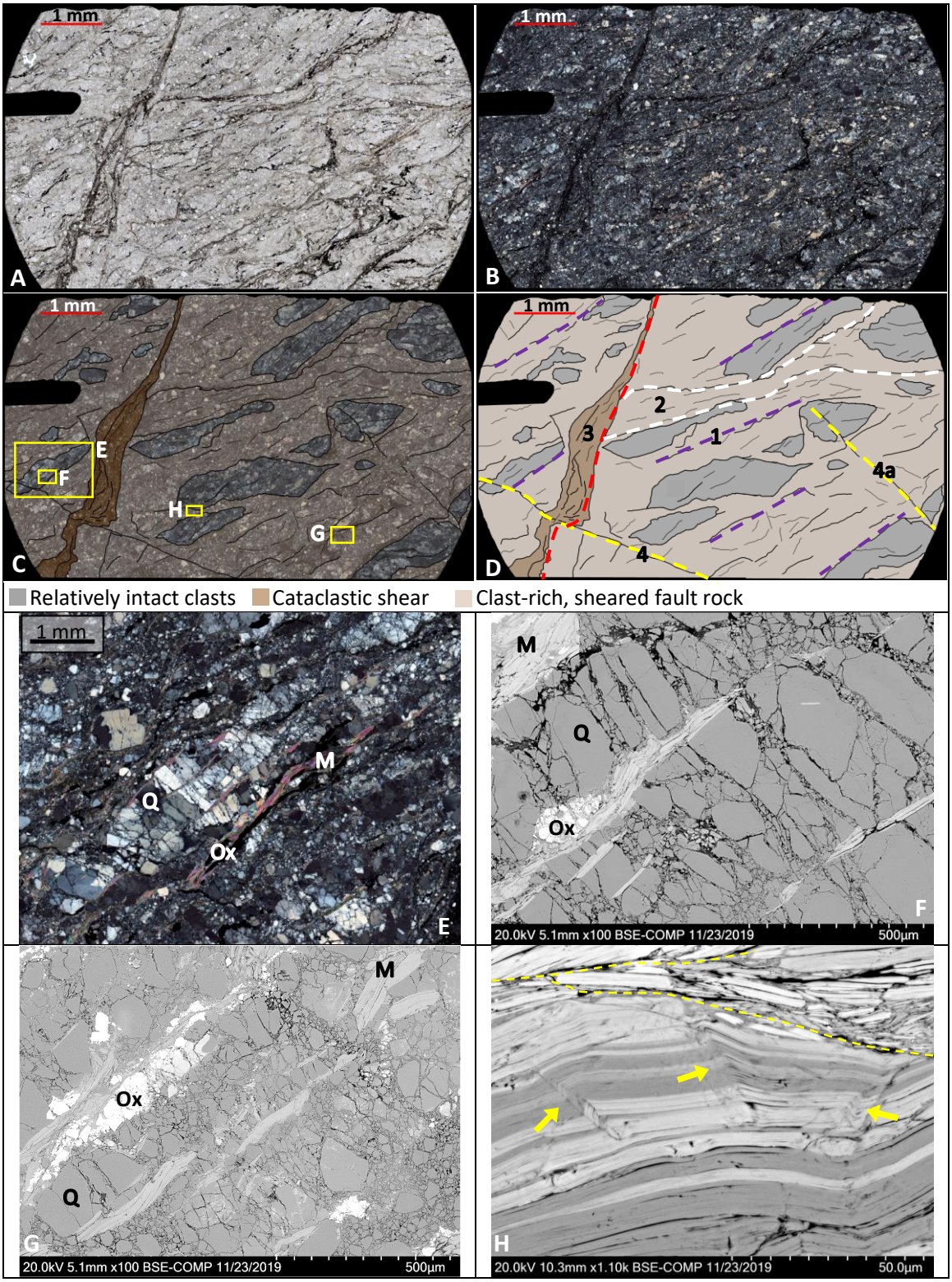

Figure 34. Type sample of webbed fractures at the optically microscopic scale. A) Plane polarized image of thin section 2_320.4. B) Cross polarized image of thin section 2_320.4. C) Mapped features of sample 2_320.4. Yellow boxes denote locations of images E-H. D) Mapped thin section

with shear events identified by dashed lines. Purple = High density oriented shears. White = Fine grained sheared rock volume with slight orientation change. Red = cross cutting vertical cataclastic shear. Yellow = Late stage shear cross cutting the oriented fabric and the vertical shear. E) Cross polarized image of a relatively cohesive clast lined by muscovite (M) and iron oxides (Ox). High angle intra-granular tension fractures can be seen within the quartz (Q) clast. Aligned phyllosilicates are visible in the sheared fault rock matrix. F) Scanning electron image (SEM) of high angle intra-granular tension fractures within quartz (Q). Phyllosilicate (M) crystals are identified lining the quartz and oxide (Ox) grains and contain textural evidence of kinks and fault propagation folds. G) SEM image of oriented phyllosilicate grains lining sheared quartz and oxide clasts. H) SEM image of kinked (yellow arrows) and altered phyllosilicates with a localized fracture across the top of the image (dashed yellow lines). The sheared crystals are bent, displaced, and aligned with the slip surface.

This sample is ~20 m from the inferred primary fault strand and is located at the edge of the interpreted primary damage zone on the N.A. plate side of the fault (Fig. 7) and records common deformation styles of phyllosilicates within the fault zone. The propagation of slip from multiple deformation events likely utilized the high density of weak, phyllosilicate-lined shear surfaces to distribute the off-fault deformation via coseismic and aseismic processes. The localized displacement along the phyllosilicate lined foliations likely created and may define the webbed/scaly texture observed in the core at the meter scale. The phyllosilicates aligned with the slip direction (Figs. 34E and 34F) may have facilitated a linking/localization of individual shear fractures over the volume of rock. A connected network of sheet silicates within cataclasites may weaken the rock-fabric under brittle deformation conditions (Colletini et al., 2009). Extensive linkages of this type could be capable of reducing the frictional resistance of the rocks and may have dispersed the total slip over a multitude of smaller, weaker network within the rock fabric. The lenses of larger, less deformed quartz clasts are bound by phyllosilicate lined shear surfaces (Fig. 34E) and may result in the localization of strain and slip accommodation within the phyllosilicate foliations.

5.1.4 Pseudotachylyte

Pseudotachylyte, when identified in a fault zone, is often referred to as a "fossil" earthquake (Cowan, 1999; Rowe and Griffith, 2015). It is generated coseismically when the frictional heating along the rupture surface overcomes the dissipation of the heat and locally melts the surrounding rock (Sibson, 1975; Rowe and Griffith, 2015). Pseudotachylyte is often identified by its melt/quench textures, dark color and aphanitic groundmass, the presence of spherulites, a devitrification texture in thin section, and sharp fracture boundaries (Rowe and Griffith, 2015). Contrary to popular belief, it is actually very uncommon for glass to be found in natural pseudotachylytes due to its poor potential for preservation (Phillips et al. 2019; Rowe and Griffith, 2015).

Sample 1-289.5 provides the type example of pseudotachylyte in the fault-related rocks. The quartzo-feldspathic gneissic protolith shows evidence of iron-oxide alteration, chloritization, and zeolite alteration coincident with fracturing. A macroscopic view of the pseudotachylyte vein indicates that this is an interclast vein within a fault wedge (Fig. 35) which is crosscut by later, cataclastic faults. The ~5 mm wide vein is pink and white in the core. In thin section, the pseudotachylyte vein appears tan to pink in plane polarized light (Figs. 36A and 36D), and tan to grey with opaque oxide clasts in cross polarized light (Fig. 36B). The SEM analyses show that the opaque clots within the vein are not single clasts but rather a higher concentration of opaque crystals measuring up to ~10 µm on average, entrained within the vein itself

Figure 35. Core image for thin section 1_289.5. Approximate location of thin section denoted by yellow box.

(Figs. 36E and 36F). Back-scattered SEM images show that the vein is comprised of anorthic-plagioclase lathes measuring on the tens of microns which vary slightly in their Al and Fe concentrations (Appendix 6). The crystal habits exhibit a quick-quench texture, similar to that of glassy volcanic rocks (Figs. 36E and 36F).

This type sample captures evidence for at least 8 deformation events, including one or more earthquakes (Fig. 36C). Several discrete cataclastic shear bands crosscut the background of fractured, altered rock, and crosscut the pseudotachylyte. Throughout the thin section and within the relatively lesser deformed wall rock zones, evidence for an initial deformation and hydrothermal alteration phase is supported by distributed microfracturing and the chloritization and sericitization of the quartzo-feldspathic protolith (Fig. 36C, 1). Within the central zone, we interpret a second deformation and alteration event through the identification of a localized zone of zeolite alteration which cuts perpendicular to the rock fabric (2). In cross polarized light (Fig. 36B), this alteration appears as a fine-grained black, white, and grey zone with entrained clasts of tan, lightly altered wall rock. The larger clasts may have been plucked from the surrounding wall rock during fracture propagation, or may be the result of dilatant vein growth which isolated the clasts within the vein. In the uphole corner of the thin section (Fig. 36), the pseudotachylyte (3) vein identified by the quench texture (Figs. 36E and 36F) represents one rupture event. The larger crystal morphology within the survivor clast and finer grained surrounding pseudotachylyte matrix (Fig. 36F) indicates that there may have been two melt events but more analysis is required in order to assert this with confidence. The fracturing and incorporation of pseudotachylyte clasts (3a) into the protocataclastic shear band (S1) represents a fourth event (4). The two roughly parallel shear surfaces (S1 and S2) do not exhibit cross-cutting relations to determine if they are contemporaneous and we therefore conservatively interpret them as representing a single deformation event. Surface S1 is characterized by a clast-

rich to proto-cataclastic matrix with the clast proportion increasing uphole. The second shear surface (S2) contains three distinct cataclastic bands organized by both mineralogic, and grain morphologic differences. The first band is a cemented phyllosilicate-rich band (5) identified by its oriented grains and light green appearance in plane polarized light (Fig. 36A). The second is a band of large, randomly distributed quartz and plagioclase grains with a sharp contact to the phyllosilicate band (6). The third is a clast-poor, fine-grained band (7) which is nearly optically opaque in cross polarized light. The S2 set of cataclastic bands conservatively indicates an additional two rupture events. The sharp contact between bands 5 and 6 may indicate that a healing phase occurred between slip on the rupture surfaces and can be interpreted as two separate events. The more gradational nature of the contact between bands 6 and 7 do not provide good evidence for a temporal relationship and are therefore conservatively interpreted as a single event. A final fracture on the uphole side of the thin section cuts perpendicular to S1 and S2 and through both the central fault rock wedge and the pseudotachylyte clasts incorporated into S1 (8).

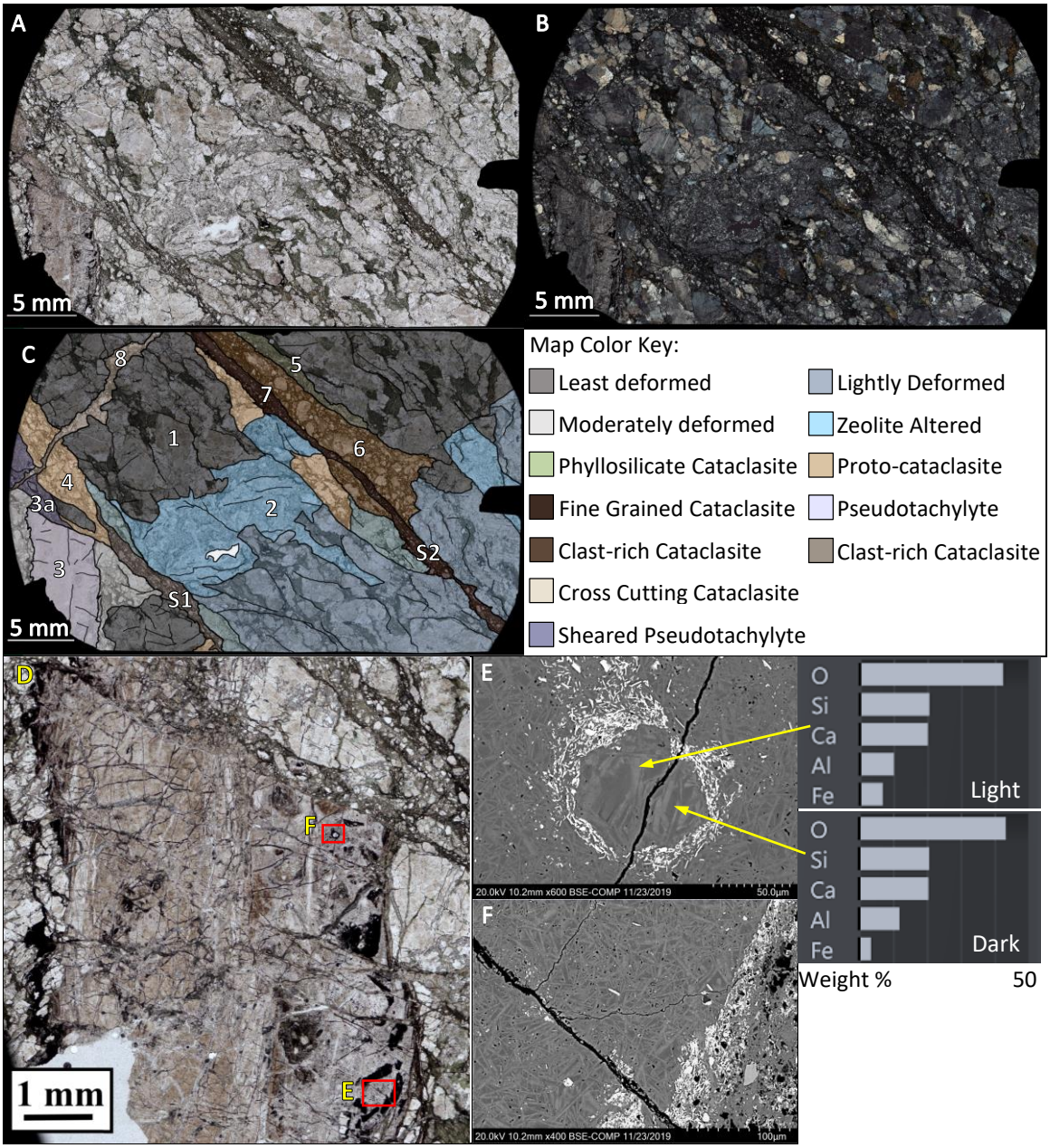

Figure 36. Pseudotachylyte vein in altered and sheared granodiorite. A) Plane polarized light image of full thin section. B) Cross polarized light image of full thin section. C) Cartoonized thin section showing major zones and features of the sample. Protolith is phyllosilicate rich granodiorite with chlorite and zeolite alteration. D) Plane polar zoomed image of pseudotachylyte showing SEM images E and F locations in red boxes. E) Quench texture of pseudotachylyte vein and clustered, disaggregated oxide grains. Charts show representative, non-stoichiometric mineralogy of the crystal lathes. F) Possible suvivor clast identified by the change in crystal habit and the oxide rim.

This sample is located ~7.5 m from the IPFS within the primary fault damage zone on the Pacific plate side of the fault structure (Fig. 7). The deformation and alteration textures identified record at least one earthquake, multiple other rupture events, and phases of healing. The pseudotachylyte is evidence of a coseismic slip event that has been incorporated into the cataclasite of a subsequent deformation event. The banded cataclasite records a single slip zone which has been reactivated at least twice and the zeolite and chlorite alterations provide evidence of fluid-assisted fault healing phases. This is the only pseudotachylyte observed in our samples. We believe this may be in part due to the unstable nature of pseudotachylyte in the shallow crust (Kirkpatrick et al., 2009) as well as the constraints on pseudotachylyte formation (Kirkpatrick et al., 2012). The mesoscopic setting of the pseudotachylyte is that of an intra-clast vein which may have allowed for increased vertical displacement due to intra-fault exhumation.

5.1.5 Pulverized Rock

Pulverized rocks can be formed through rapid isotropic tensile loading associated with the tip of a supershear rupture (Ben Zion and Shi, 2005; Dor et al., 2006; Doan and Gary, 2009; Sullivan and Peterman, 2017). Pulverized rocks are identified by their incredibly high density of randomly oriented, open-mode fractures (Dor et al., 2006; Rempe et al., 2013). Pulverized rocks are differentiated from other granular fault rocks by their: 1) preservation of primary grain shapes, 2) evidence of little to no grain shear or rotation, 3) presence of pervasive fractures which show little to no preferred orientations, and 4) grain size reduction to the micron scale (Mitchell et al., 2011; Wechsler et al., 2011; Rempe et al., 2013; Sullivan and Peterman, 2017). Typically, pulverized rocks are expressed in outcrops as white, highly friable rocks with no fabric (Dor et al., 2006)

Pulverized rocks are common in the drill core. Mesoscopically, these are rocks which maintain their original protolithic texture but have intra-granular fractures which break the grains into sub-millimeter clasts (Dor et al., 2006) resulting in a powdery consistency upon touch. In the core, the pulverized rocks are structurally overprinted by later shear on fractures, and distributed granular flow and disaggregation (Fig. 37). The shear surfaces are characterized by two orientated sets which lie nearly perpendicular to each other and are decorated with oxide minerals. Microscopic expressions of pulverized rocks in plane polarized light show that these rocks are fine-grained white to tan quartzo-feldspathic fault rocks (Fig. 38A). In thin section, a pulverized clast measuring ~5 mm in width is identified by its spearhead shape, high fracture density, and lack of grain boundary displacement or rotation (Fig. 38B). Smaller clasts of pulverized rock and sheared pulverized rock are present throughout the sample (Figs. 38C and 38D). The mineralogy is predominantly quartz, biotite, opaque minerals - likely pyrite and ilmenite, and calcite with minor feldspar and titanite.

Figure 37. Core image for thin section 2_285.5. Approximate location of thin section marked by yellow box.

In our type sample of this texture, we establish an order of deformation events (Fig. 38D) in which the evidence indicates the pulverization occurred early, followed by phases of healing and cataclastic shearing. The evidence of deformation and alteration within this sample supports up to at least 5 deformation events, some of which were likely due to fast seismic slip rates. The presence of pulverized clasts (1) indicates that a seismic rupture event is recorded here. The post-pulverization shearing of the pulverized rock (1a) could indicate two separate slip events or be the result of displacement during the co-seismic rupture, which caused the initial

pulverization. The calcite cement (1b), identified in SEM (Fig. 38E), is constrained within the spearhead shaped pulverized clast (1) indicating a possible healing phase of hydrothermal-aided precipitation before subsequent deformation. Mechanical twinning of the calcite cement within the sheared pulverized rock grains indicates that plastic deformation in the calcite followed the creation of the pulverized rock. Sheared pulverized rock is evidenced by the oriented, matrix-rich cataclastic shear surfaces on the left side of the thin section which we interpret as a second rupture event (2). These shear surfaces were then cut off by a subsequent rupture event (3) which realigned the clast orientations within a phyllosilicate and pyrite rich matrix. This event may have also aligned the phyllosilicates identified in SEM (Fig. 38F). Evidence for a fourth deformation event lies in the offset of the near vertical oriented shear surfaces by fracture set 4. This offset is marked by its displacement of the phyllosilicate rich central region and the presence of aligned pyrite crystals within the cataclasite. Shear surface 4 also creates a clear boundary between the calcite cemented materials of 1b and the cataclastic shear bands. A final event (5), which cuts the cataclastic shear in the lower right hand corner of the thin section, is oriented at approximately 80° to 4 and displaces the calcite-cemented clasts which formed the stair-step geometry of the cemented pulverized clast.

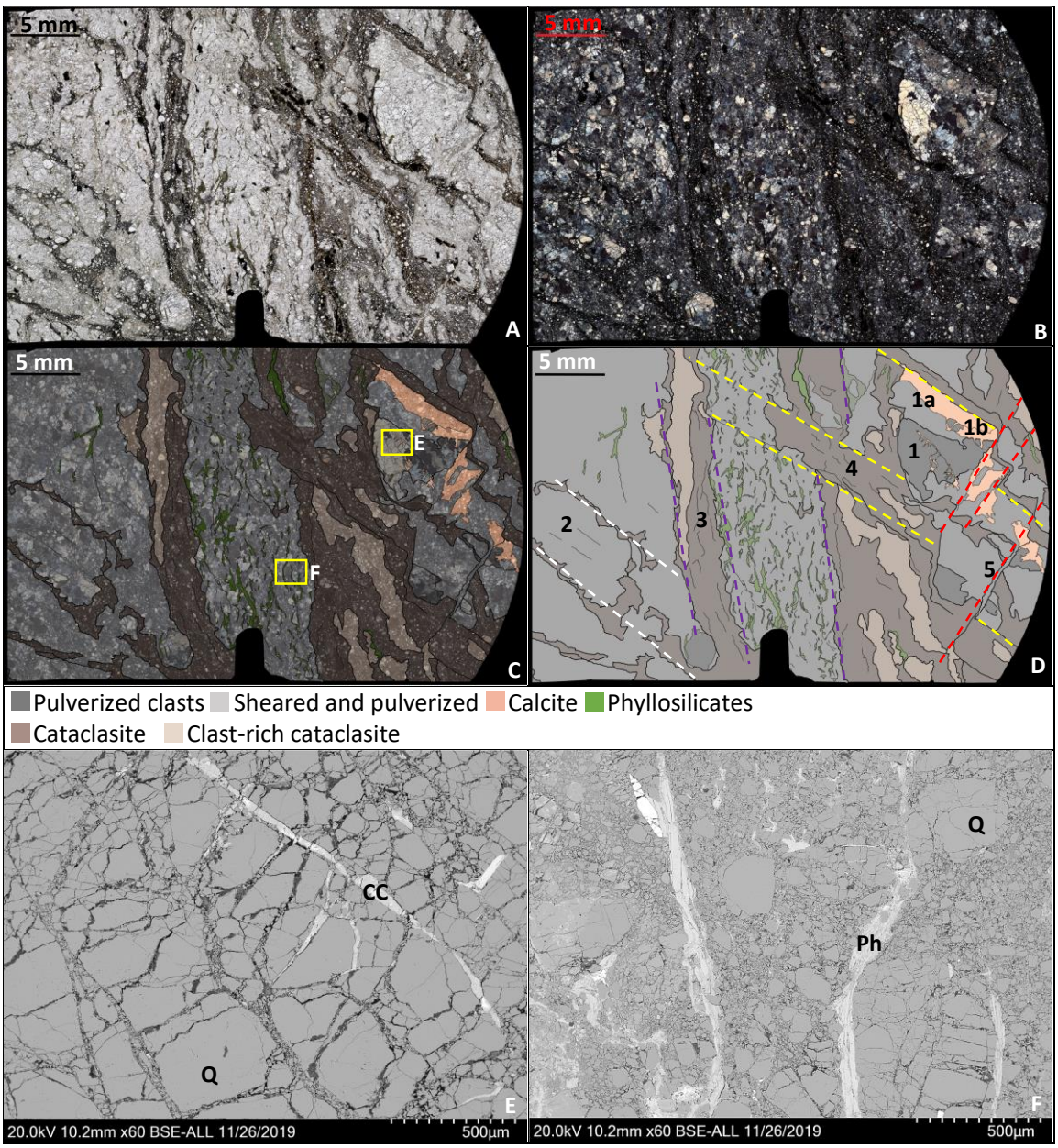

Figure 38. Characterization of a sheared pulverized rock. A) Plane-polarized light image of pulverized rock. B) Cross-polarized light image of pulverized rock. C) Thin section map with yellow boxes denoting the SEM image locations for E, F. D) Pulverized clast = 1, Pulverized and sheared clast = 1a, Calcite cement = 1b, White dashed lines = 2, Purple dashed lines = 3, Yellow dashed lines = 4, red dashed lines = 5. E) Backscatter electron microscopic image of calcite cement (CC) within pulverized quartz (Q) clast. F) Backscatter electron microscopic image of phyllosilicates (Ph) aligned with shear direction and lining fractured quartz (Q) and clasts.

This sample is located on the N.A. plate side of the fault and is within the primary fault damage zone ~12 m from the IPFS (Fig. 7). This sample records deformation textures indicative of coseismic slip and crystal plasticity as well as evidence for post-seismic healing through mineral precipitation and cementation. The formation of pulverized rock occurs over a volume of space and has been identified up to 100 m from the fault core (Dor et al., 2006). Although the pulverization process greatly reduces the strength of the host rock, subsequent phases of shear displacement and mineral cementation may recover some of the lost strength. Large volumes of disaggregated, sheared pulverized rocks may impact the distribution of slip within the fault zone and by changing the rheologic properties of the fault-related rocks, impart some control on the deformation mechanisms that occur and are recorded in the fault damage zone.

5.2 Characterization of Fault Processes within the Elizabeth Lake Damage Zone

We address three overarching questions for the shallow San Andreas Fault at the Elizabeth Lake site: 1. What is the style and nature of deformation and alteration in the fault zone and fault-related rocks? 2. What evidence exists for coseismic and aseismic slip mechanisms? and 3. How do our observations of the damage zone constrain the fault zone processes and properties? We focus on the roles of heat, fluids, and time, which are both complementary and counteractive agents of fault zone deformation processes over the course of multiple earthquake cycles. We discuss how the fault zone evolves to accommodate the absorption and distribution of earthquake-related energy and slip propagation.

We recognize the importance and complexity of the interconnected relationships between fault zone processes and resultant deformation and alteration textures. In order to constrain the scope of this project, we focus on the broader implications of the data presented

here. This project provides an opportunity to characterize the shallow fault zone processes which occur within the uppermost ~100 m to 3 km of the earth's crust. The shallow depth range poses some challenges as a majority of studies focus on fault zone processes that are concentrated within the deeper fault core (Niemeijer and Spiers, 2005; Schleicher et al., 2010; Carpenter et al., 2012; Proctor et al., 2014; Richard et al., 2014), and so extrapolation of results from these types of studies is conceptual until more direct work in shallow rocks is completed.

5.2.1 Damage Zone Distributions of Deformation and Alteration Textures

We document the nature of deformation mechanisms, and evidence for mineral alteration fluid-rock interactions, and their distribution throughout the fault zone as sampled by the seven inclined boreholes. We classify these deformation microstructures and alteration textures according to their primary formative processes as well as their occurrence in space and time (Fig. 39). To discuss our wide array of observations, we relate each feature to four framework categories: 1. Primary texture, 2. Earthquake cycle phase, 3. Relative volume of affected rock, and 4. Distribution throughout the fault zone (Table 1). Many of these may be categorized into more than one "bin" and our groupings are based on our primary observations of the feature's interpreted function.

Primary texture (Table 1) refers to the whether the observation made is identified as a deformation microstructure or as an alteration texture. Calcite is categorized as both deformation and alteration as its characteristics are related to both classifications. Cataclasite on the other hand, is a deformation related microstructure (Sibson, 1977).

Our classification of earthquake cycle phases (Table 1) refer to the time at which we expect the deformation or alteration event occurred; during coseismic rupture, aseismic slip, or

locked healing, which we use to represent an almost static, or locked state within the interseismic period. For example, pulverized rocks are formed during coseismic slip (Doan and Gary, 2009), cataclasites may be formed through coseismic or aseismic slip (Rowe and Griffith, 2015), and mineral precipitations such as vuggy zeolites are formed in a near static environment.

The volume of affected rock (Table 1) refers to how localized or distributed these processes were at the time of formation. Clay-clast aggregates require highly localized slip to induce thermal pressurization and therefore are formed within a very limited area (Boutareaud et al., 2008; Rice, 2006). Pulverized rocks form in a large volume of rock and are distributed over the fault damage zone (Mitchell et al., 2011; Rempe et al., 2013). Mineral alteration, such as chlorite formation, depends partially on the permeability structure of the fault zone and is considered distributed as the process does not require a specific area interface.

Distribution throughout the fault zone refers to where we identified these features in the ~170 m wide zone we sampled. From our observations, most of the deformation and alteration processes are distributed throughout the width of fault damage zone examined here. The structures and textures identified as distributed are common and our petrographic work indicate that more than one deformation structure and alteration texture co-occur within the resolution of single, standard thin sections. The localized structures, i.e. pseudotachylyte and vugs (Table 1), were not common within our samples. This may be a function of sampling and not necessarily represent processes which are constrained within certain regions of the fault zone.

FEATURE	PRIMARY TEXTURE	EARTHQUAKE CYCLE PHASE	VOLUME OF ROCK	FAULT ZONE DISTRIBUTION
Clays	Alteration	Healing phase	More work	Localized*
Calcite	Deformation and Alteration	Aseismic/Healing	Distributed	Distributed
Cataclasite	Deformation	Coseismic/Aseismic	Localized	Distributed
Chlorite	Alteration	Healing phase	??	Distributed
Clay Clast Aggregate	Deformation	Coseismic	Localized	Distributed
Fe-Ox Alteration	Alteration	Healing phase	Distributed	Distributed
Injection Veins	Deformation	Coseismic	Localized	Distributed
Geochemical Alterations	Alteration	Healing??	Distributed	Distributed
Gouge	Deformation and Alteration	Coseismic/Aseismic	Distributed	Localized
Phyllosilicates	Deformation and Alteration	Coseismic/Aseismic	Localized	Distributed
Pseudotachylyte	Deformation	Coseismic	Localized	Localized*
Pulverized Rocks	Deformation	Coseismic	Distributed	Distributed
Vugs	Alteration	Healing phase	Localized	Localized*
Webbed Fractures	Deformation	Coseismic/Aseismic	Distributed	Distributed
Zeolite	Alteration	Healing phase	Distributed	Distributed

Table 1. Deformation textures, structures, or mineralization categorization identified at this site. Overarching characterizations of our identified deformation and alteration textures. * indicates a limited observation due to sample contents.

Within the shallow SAF damage zone at Elizabeth Lake, brittle deformation is the predominant deformation mechanism. This deformation was accompanied by fluid-assisted alteration, which changed the rheological properties of the fault damaged rocks over time and space (Fig. 39). Heat within a fault zone is generated rapidly through frictional heating (Lachenbruch, 1986; Rice, 2006; Ault et al 2015; McDermott et al., 2017) and transported within the fault zone over longer timescales through advective fluid transport. The heat dissipates into the fault complex, which we document by the presence and distribution of alteration products that formed at temperatures likely above the ambient geothermal values. For example, the expected ambient geothermal temperature is ~60^{o}C at 2 km depth and we document fault-related mineralogic alteration assemblages indicative of temperatures over 200^{o}C. This mature and complex fault damage zone shows evidence of very localized slip as identified by banded

gouges ~ 10's of cm thick along several fault branches, as well as deformation mechanisms including the pulverized rocks and common cataclasite-filled shear zones distributed throughout the sampled area. Slip accommodation appears not to have been localized on only one fault core as documented by the presence of multiple slip events identified throughout the fault damage zone (Table 1) and the presence of several cataclasite and clay gouge zones.

The deformation and alteration mechanisms interacted over multiple cycles to create the mature damage zone we see today. Each seismic event changes the rheologic context within which subsequent processes must operate. For example, two processes which may counteract each other are pulverization and injection veins. Both are constrained to coseismic slip rates and occur over a matter of seconds (Doan and Gary, 2009; Rowe and Griffith, 2015). Pulverization creates a very high damage density over a volume of rock resulting in a decrease in rheologic strength. Pulverization may prevent injection veins from forming as the off-fault stress required to initiate tensile crack propagation may not be attainable. Some processes require previous deformation or alteration to prepare or prime the surrounding rocks. For example, aligned phyllosilicates along shear surfaces at fracture contacts and within gouge zones decrease the permeability of the fault damage zone (Collettini et al., 2009; Ikari et al., 2009) and may encourage thermal pressurization (Ikari et al, 2009). Thermal pressurization dilates the fault and is required for the formation of clay-clast aggregates (Boutareaud et al., 2010). The alteration to clays and the formation of oriented clay gouge are common processes within the SAF damage zone, but these processes likely require multiple earthquake cycles to form (Fig. 37) (Jacobs et al., 2006). It is important to recognize that the presence or absence of a specific feature does not preclude other processes from occurring, but the changes in the state of the fault zone over multiple earthquake cycles will exert controls on which features are formed and preserved.

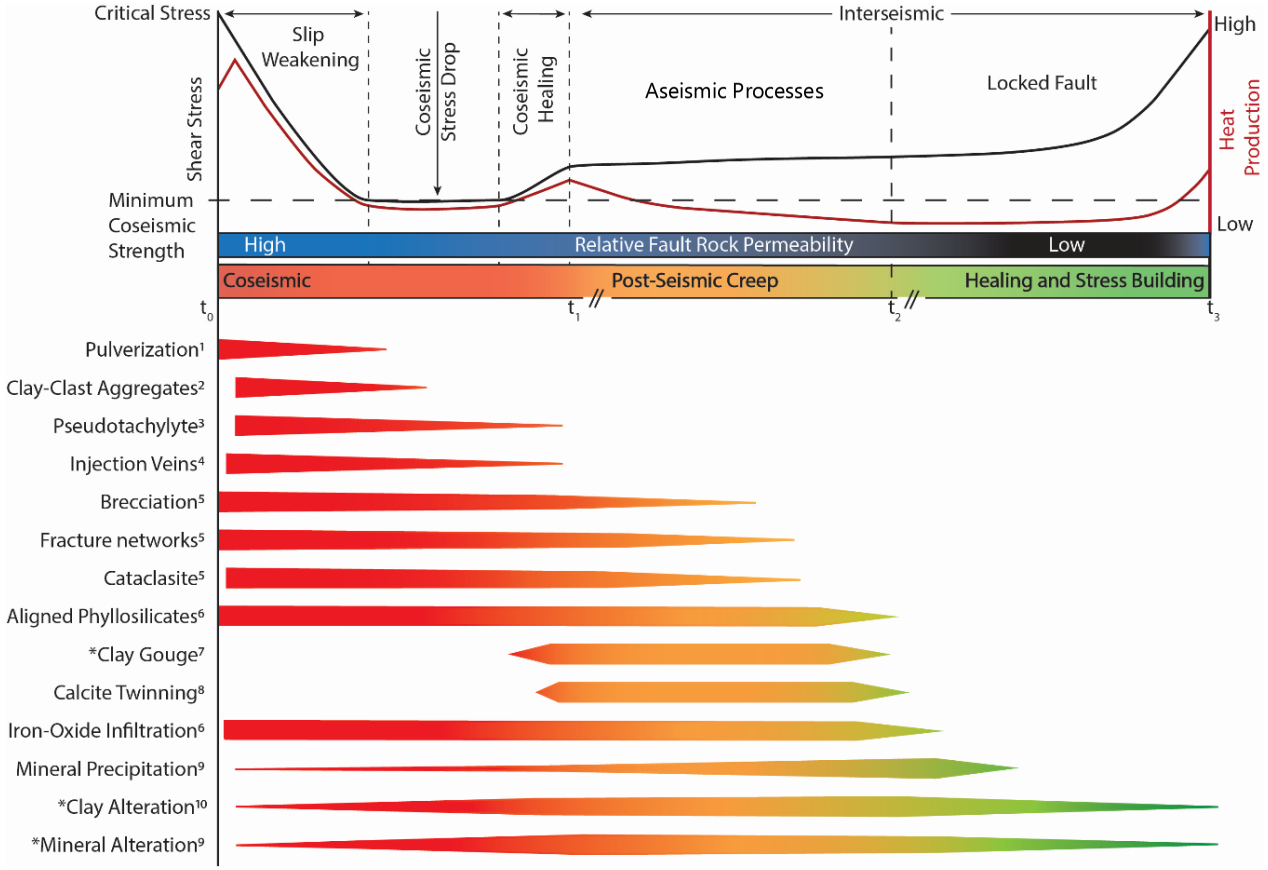

* indicate features which likely take more than one earthquake cycle to form.

Figure 39. Fault zone processes and associated fault-related rocks or alteration products documented in this study. The upper half of the figure depicts the expected fault zone processes over one earthquake cycle and does not include aftershocks. Time is on a relative scale with t_0 = fault rupture, t_1 = post seismic recovery, t_2 = locked fault, t_3 = immediately prior to the next event. The bottom half of the figure lists the features identified through this work with bars indicating the features' formative phase range. Variable bar thickness indicates increased or decreased likelihood of formation. Image partially adapted from Niemeijer et al., 2012. [1]Doan and Gary, 2009; [2]Boutareaud et al., 2010; [3]Sibson 1973, 1975; [4]Rowe et al., 2012; [5]Sibson 1977; [6]Evans 1990; [7]Vrolijk and Van der Pluijm, 1999; [8]Sibson 1986; [9] Richard et al.. 2014: [10]Jacobs et al.. 2006.

5.2.2 Deformation Mechanisms

Within the San Andreas fault at Elizabeth Lake we document evidence for elastic-brittle to plastic deformation processes in the same rock volume and in some cases, which overlapped in time (Fig. 39). All samples collected from the Elizabeth Lake core exhibit some range of fractures, cataclasite-filled shear zones, zones of oriented fault gouge, pulverized rocks, and/or displaced brecciated clasts. These structures occur throughout the entirety of the drill-core with the largest, most developed gouge zones, low single-point resistivities, and low V_p values being used to interpret the main fault strands and associated damage zones (LADWP Final Report 2019).

Microscopically, fracture systems filled with cataclasite, gouge, precipitated minerals, and/or mineral alteration are identified in nearly all samples. Fractures exhibit a variety of geometries and densities, which range from sharp discrete slip surfaces to dispersed shear zones. Cataclasite and fractures are the most common evidence of brittle failure within our samples. Multiple generations of cataclasite, reworked cemented clasts, and cross-cutting relationships indicate repeated damage accrued and slip surface reactivation occurred within the fault zone over multiple earthquake cycles.

The distribution of the coseismic features within the fault zone – injection veins, pulverized rocks, pseudotachylyte, and clay clast aggregates (Table 1), indicate that fast slip and significant displacement has occurred throughout the damage zone. The abundance of calcite twinning, phyllosilicate deformation, and dilatant vein textures indicate that some slow slip occurs as the stress regime changes over the earthquake cycle.

Microscopically observable phyllosilicate linkage was identified in the form of fine-grained crystals aligned along slip surfaces in gouge, as sheared and kinked bands within

brecciated fault rocks, and as shear surface boundaries between damaged rocks and cataclasites or gouge. Networks of interconnected, aligned phyllosilicate grains creates and promotes the possibility of frictionally reduced aseismic slip and significantly weakens a fault zone (Neimeijer and Spiers, 2005; Collettini et al., 2009). The phyllosilicates along and within discrete slip zones may suggest two mechanisms regarding their response and influence on fault development. The first interpretation is that the slip event itself prioritized the weak crystal structures by creating connected pathways to and near the low frictional strength phyllosilicates (Borg and Handin, 1966; Evans, 1988; Colletini et al., 2009). In our samples, the phyllosilicates identified as aligned with shear surfaces are interpreted as the result of plucking and sheared-entrainment of the protolith micas. The second interpretation is that slip along the shear surface creates a connected fracture network which creates permeability and may precipitate phyllosilicates. In our samples this may be evidenced by the authigenic clay growth within fine-grained, optically opaque shear matrix.

5.2.3 Alteration

Mineral alteration within fault zones is related to the fault structure, permeability, hydrogeologic setting (Caine et al., 1996; Faulkner et al., 2010), temperature regime, and mineral and fluid compositions (Simpson, 1986; Janëcke and Evans, 1988; Wintsch et al., 1995). Mesoscopically, iron-oxide and chlorite alteration, and calcite and zeolite veins are common. Microscopically, some form of alteration, including plagioclase sericitization, sausseritization, and zeolitization, the formation of calcite or zeolite veins and cements, and the chloritization of biotite and amphiboles is present in every sample we observed. Zeolite (laumontite) and calcite are the most common alteration minerals and are found in veins, cements, and mineral

replacements. These minerals stem from the decomposition/alteration of plagioclase and feldspar grains releasing Ca, Na and K into the fault zone. The distribution of calcite and zeolite in veins and cements throughout the fault zone suggests that the fault zone regains some strength between rupture events. The decomposition of plagioclase into pseudomorphs and into altered materials changes the rheologic properties of the original protolith. This alteration indicates that the background strength of even the more intact fault rocks decreases over time.

Shortly after the coseismic rupture propagates through the rock, post-seismic healing likely begins as rapid healing via the quenching of pseudotachylyte veins (Kirkpatrick et. al, 2013; Rowe and Griffith, 2015), the formation of fault mirrors (Ault et. al, 2019), or silica gels (Kirkpatrick and Rowe, 2013; Rowe and Griffith, 2015). Over longer periods of time, fault healing may be linked to alteration processes including mineral precipitations as vein fill and cements, the formation of stylolites, and as mineral alterations and replacements (Fig. 39).

Swelling clays identified mesoscopically in core are classified as fine-grained gouge. These were imaged through SEM as likely smectite clays that appear amorphous within sheared zones. Preliminary XRD analysis identified these clays as illite-smectite, and chlorite-serpentine, which agrees with other geochemical and grain size analyses for rocks here (Studnicky et al., 2019; Williams et al., in prep). Authigenic and altered clays within the gouge decrease fault zone permeability, which may promote fault-zone compaction, higher pore fluid pressures, fault-zone compaction, and thermal pressurization (Ikari et al., 2009). Increases in pore fluids and pore-fluid pressures can create saturated phyllosilicates that may decrease the frictional strength of the slip zone by up to 60% (Ikari et al., 2009). Within our samples, we identified chlorite and biotite in both the fault damaged rocks and sheared zones, and muscovite within the fault damaged rocks.

Fluids and temperature. The general trend of increased alteration in the more deformed fault-rocks leads us to infer that fluid-rock interactions facilitated the majority of the observed alteration processes in the fault zone. Wide-spread calcite, zeolite, and iron-oxide alteration provides evidence of increased permeability in proximity to slip surfaces and fractures as well as fluid-assisted element mobility within the fault system. The presence of calcite and laumontite alterations indicate temperatures ≤ 250°C (Utada, 2001; Ferrill et al., 2004). The observed quartz recrystallization is likely the result of deformation before the onset of seismicity related to the SAF, as quartz dislocation creep becomes active at temperatures ≥ 280° ± 30°C (Stipp et. al., 2002), higher than the temperatures expected within the shallow (~ 2-3 km) fault zone. The distribution of alteration products throughout the fault zone indicates that the increased temperature, above the inferred ~30°C/km geothermal gradient for the area (Lachenbruch, 1986), is not confined to only the discrete slip surfaces and dissipates into the surrounding fault rocks.

Temperatures above the expected geothermal gradient within the fault damage zone may be generated via short term pulses of frictional, coseismic heat or from hydrothermal advective fluid flow within the fault-zone's permeable structure (Fig. 40). It is unlikely that the frictionally generated heat, i.e. thermal pressurization or flash heating at asperity contacts (Rice, 2006), resulted in wide-spread mineral alterations due to the very short time period over which these processes function (Lachenbruch, 1986; Rice, 2006). We interpret, based on the positive relationship between the degree of damage and the degree of alteration that the main source of elevated temperatures results primarily from advective fluid flow with pulses of frictionally generated heat working constructively to influence the thermal regime of the fault damage zone. This is compatible with observations at Cajon Pass where longer periods of flow are

interpreted to be interrupted by mechanically or tectonically driven periods of rapid flow (Torgersen and Clarke, 1992).

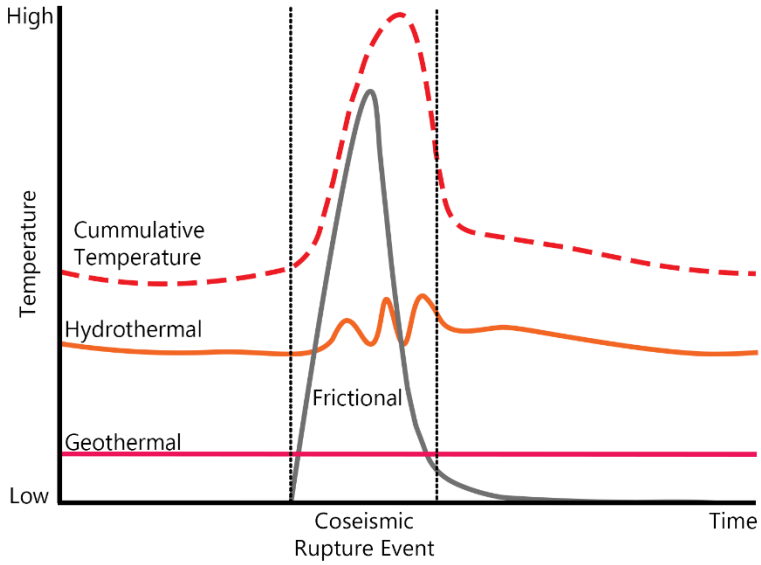

Figure 40. Schematic representation of interpreted heat sources within the fault damage zone. Hydrothermal fluid flow provides a majority of the above expected geothermal temperatures. Changes in fluid pathways and stress regimes may change the hydrothermal source and create variation in the temperature of the advective fluids. Hydro- and geothermal sources provide more sustained heat (Forster and Smith, 1989). Pulses of frictionally generated heat are short lived and accent the cumulative temperature of the damage zone (Lachenbruch, 1986).

Laumontite, one of the most common alteration minerals documented in the drill core, is a hydrous, low-grade metamorphic alteration product within plagioclase-rich rocks exposed to fluids (Utada, 2001; Deer et al., 2004). Laumontite is a common alteration mineral along and within the San Andreas Fault and is stable within the temperature range of ~50 – 230°C (James and Silver, 1988; Vincent and Ghlig, 1988; Blenkinsop and Sibson, 1992; Weschler et al., 2011, Forand et al., 2014). The alteration of plagioclase to laumontite may result in up to a 60% molar volume increase (Boles and Coombs, 1977; Blenkinsop and Sibson, 1992). There is a close relationship of zeolites to the bleaching of highly damaged rocks in other parts of the San

Andreas system (James and Silver 1988; Vincent and Ghlig, 1988; Weisenberger and Bucher, 2010) and zeolite veins often coincide with calcite. As a cement within sandstone reservoirs, laumontite has been shown to decrease porosity by up to 5-20% (Jove and Hacker, 1997) and as an alteration product, laumontite-rich sandstones have a low elastic modulus and low mechanical strength (Chen et al., 2020). Laumontite alteration and precipitation may assist in increasing pore fluid pressures as it decreases overall permeability and porosity (Morrow and Byerlee, 1988), and high concentrations of zeolite may weaken the overall fault rock strength (Morrow and Byerlee, 1991) and promote non-elastic behavior within the fault zone (Vernik and Nur, 1992). A high concentration of zeolite alteration has been shown to significantly decrease the seismic velocities of rocks (Vernik and Nur, 1992; Julia et al., 2014). Widespread laumontization of plagioclase and its precipitation as dilatant vein fill and cement may facilitate post-seismic recovery and background fault zone weakening as well as contribute to the low seismic velocities of the fault damage zone (Blenkinsop and Sibson, 1992).

Calcite is common within the fault-related rocks and forms over a wide range of temperatures. Calcite vein fill and cement are evidence of fluid-assisted healing within the fault damage zone. Twinned calcite cement was identified in pulverized rocks, in which intra-granular fractured rocks recover some of the lost strength of the damaged grains via cementation. Almost all calcite crystals exhibit mechanical twinning, which is evidence of plastic deformation and can function as low as ~20°C (De Bresser and Spiers, 1997; Ferrill et al., 2004). Following Ferrill et al., (2004), we use the thick-twinning habit of the calcite crystals to infer a formative temperature (Fig. 28). In our samples, we identified twinned (i.e., aseismic processes occurred) calcite veins which were subsequently cut by brittle fractures filled with precipitated zeolite. We did not find ample evidence of dynamic recrystallization which is expected to occur at ~250°C (Ferrill et al., 2004). The calcite grains with optically measurable twins indicate a temperature

range of ≥20°C to ≤ 250°C with the high density and morphology of the twinning likely indicating temperatures closer to ~170°C - 200°C (Ferrill et al., 2004). The mechanical twinning and subsequent brittle fracturing provide evidence for aseismic to brittle transitions as well as alternating fluid flow events.

Taken as a whole, the fault-related alteration within the damage zone indicate a temperature regime of up to ~250°C, a fault zone of reduced strength, an open, permeable fracture system facilitating fluid flow and element mobility, reduced permeability within gouge, and a relatively high concentration of low seismic velocity minerals. The ample zeolite and calcite alteration in the fault-related rocks change the host rock rheologic properties, the permeability and porosity of the damaged rocks, and through cementation, recover some rheologic strength lost in previous rupture events.

5.3 Fault Zone Evolution

Fault zone development is not a unidirectional process (Faulkner et al., 2010). Core recovery during drilling was nearly 96% (LADWP Final Report, 2019) indicating that while these rocks are pervasively damaged and altered, they are also remarkably indurated. This induration may be attributed to the common and widely distributed occurrence of calcite and zeolite cements and veins, and the fine-grained clay and oxide-rich sealed fractures which are facilitated by the damage structure and fluid pathways of the fault zone.

The brittle deformation led to decreases in the strength of a fault zone; brittle deformation also increases the surface area of minerals available to mobile fluids and therefore encourages alteration processes such as the decomposition of feldspars. The fresh, reactive mineral surfaces may be altered and their leached elements allow for the precipitation of other

minerals, like calcite and zeolites, within the system. Although these mechanisms lead to fault weakening, the subsequent precipitation of veins and cements decreases the fault zone permeability (Fig. 39) and increases its strength.

Pseudotachylyte and CCA formation require large, short term increases in heat generated from frictional sliding whereas pulverization and injection veins form independently of frictionally generated heat within the fault zone (Fig. 39). Mineral alteration occurs independent of slip rate and is controlled by the available heat and fluid compositions within the fault zone (Fig. 39). Alteration varies in the temporal requirements for formation but is expected to be most prevalent as the heat generated from the frictional sliding of rupture events dissipates into the fault zone and while there are permeable fluid pathways, which may also facilitate heat transfer (Fig. 39; Jacobs et al., 2006; Shipton et al., 2006). Within the mature SAF damage zone, cycles of sustained damage, alteration, and partial strength recovery have created an interconnected network of slip surfaces and cross cutting relations over which the processes identified in this project occur.

We propose that the shallow fault zone at Elizabeth Lake is a distributed zone in which accommodation occurred via coseismic and aseismic processes. Our data and the observations in the tunnel during its construction (Mulholland, 1918; Sutherland et al., 2014) indicate that while localized slip occurred within the fault damage zone, fault slip might have occurred throughout the damage zone complex, and perhaps in adjacent strands of the fault (Sharp, 1954). The majority of the damage observed in the drill core recovered from the shallow SAF represent brittle deformation mechanisms that likely function over the coseismic and interseismic periods of the earthquake cycle. Post-seismic creep and recovery of the shallow slip deficit may occur during the first part of the interseismic period before the fault becomes

locked. This slip recovery may be facilitated by plastic deformation within weak minerals such as calcite and/or zeolite, as volume changes due to dilatant vein fill and mineral precipitation, or as slip along the oriented and aligned weak basal cleavages of phyllosilicates. We propose these mechanisms as possibilities of aseismic slip within the shallow crust based on their observed microscopic textural characteristics, their distributions throughout the fault zone, and their observed common occurrence.

6. DISCUSSION

6.1 Fault Zone Structure

The structure of fault zones has been discussed at length (Chester and Logan, 1986; Chester et al., 1993, Caine et al., 1996; Faulkner et al., 2010; Holdsworth et al., 2011) and can generally be conceptualized by three zones; the fault core, the damage zone, and the lesser damaged host rock. Some workers (Kim and Sanderson, 2004; Townend et al., 2017) suggest that the damage zone be separated into an inner, highly damaged fault linking zone and outer less damaged wall rock zone. The proportion of how much of each of these exist in or along a given fault can vary as a function of continued deformation and rock properties.

The distribution of these fault components likely impart controls on earthquake rupture behaviors including slip localization, seismic wave radiation, and energy dispersal as the earthquake rupture propagates to the surface. In many cases, fault cores accommodate the majority of earthquake related slip and are often characterized by narrow slip surfaces and clay gouge (Chester and Logan, 1986; Caine et al., 1996; Holdsworth, 2004; Shipton et al; 2006). The width of a fault core depends on the maturity of a fault as repeated slip events progressively damage and alter the host rocks (Shipton et al., 2006; Savage and Brodsky, 2011). Damage zones are mechanically related to the fault core as seismic energy radiates out of the localized slip zone and deforms the surrounding rock (Caine et al., 1996, Cochran et al., 2009, Zoback et al., 2010). These damage zones can be characterized by a high proportion of small faults, fractures, veins and folds (Chester and Logan, 1986; Caine et al., 1996; Faulkner et al., 2003, 2011; Kim and Sanderson, 2004; Mitchell and Faulkner, 2009; Savage and Brodsky, 2011), which decrease in density away from the fault core. The undamaged protolith is encountered when the damage recorded in the host rocks falls to a background level and is unlikely to be a result of fault-

related seismicity. The fault zone architecture may be composed of a singular main fault strand which accommodates the majority of earthquake related deformation and slip (Caine et al., 1996), or as an anastomosing, linked complex of fault cores and distributed damage zones (Faulkner et al., 2003).

A positive relationship tends to exists between the degree of fault maturity and the degree of slip localization. The SAF at Elizabeth Lake is a mature fault with a primary damage zone with at least two main faults, each with subsidiary branches, and two secondary damage zones with multiple inferred smaller faults on either side of the primary fault (Fig. 3; Mullholland, 1918; Sutherland et al., 2013). Based on the shallow structure (Fig. 3) and terrestrial laser scanning of the tunnel (Tayyebi et al., 2017), proximal strands identified in the geotechnical study (Fig. 3) (Appendix 1), the distribution of oriented gouge, highly damaged rocks, alteration throughout the fault zone, and fracture distribution determined from acoustic televiewer logging (LADWP Final Report, 2019), the structure of the SAF at the Elizabeth Lake site is an intermediary between a highly localized and anastomosing fault complex. Throughout the 6 My history of seismic activity along the Mojave Segment of the SAF, slip has likely migrated between the identified strands and created a network of intra-fault wedges each containing variable deformation and alteration characteristics. We suggest that a majority of displacement may be localized along the primary strands, but evidence of reactivated slip surfaces throughout the damage zone and subsidiary faults indicate that displacement has been distributed throughout the fault zone complex.

6.1.1 Deformation Distribution and Accommodation

The distribution of slip within and between the primary and secondary fault strands and associated damage zones has implications for the accommodation of the earthquake energy within the shallow crust. Fault-related damage and fault zone thickness can be fit to a decay curve with superimposed secondary faults possibly functioning as damage localizing mechanisms (Savage and Brodsky, 2011). Applying the Elizabeth Lake SAF structure to their model, we infer the energy budget is distributed over multiple subsidiary fault strands and entrained fault blocks within the shallow crust. The energy budget relates the total potential strain energy that loads a fault before rupture to the work done to overcome resistance to frictional slip (Kanamori, 1994) and the work to drives the subsequent rupture. This work is consumed and partitioned into three categories; 1) the seismically radiated energy, 2) the fracture energy, and 3) the thermal energy (Kanamori and Rivera, 2006). In general, overcoming the resistance to slip consumes as much as ~90% of the energy produced (Scholz, 2019; Rowe and Griffith, 2015).

The earthquake and fault-related rock products at the Elizabeth Lake site - the gouge zones, cataclasites, and altered mineral assemblages, are evidence for the consumption of much of the energy within the fault damage zone (Fig. 39). These may provide a possible explanation for how the dynamic portion of the energy is distributed as the rupture propagates through the fault zone. The anastomosing structure of the fault cores, with a superimposed matrix of previously produced damage and healing, facilitates the absorption of rupture generated energy. Distributed shaking may lead to deformation microstructures such as brittle flow or the reactivation of small slip surfaces in the damage zone. It has been estimated that shear heating resulting from the pulverization of rocks in the shallow crust may lead to an ~100°C temperature

rise (Ben-Zion and Sammis, 2013). This could create a volume of rock within which the dissipation of frictionally generated heat induces fault zone weakening through mineral alterations and increased permeability. We see evidence that may support this in the distributed CCAs, the commonality of the pulverized rocks, the pervasive zeolite and calcite alteration/cementation, and the aligned and altered phyllosilicates. Based on the data presented here, we could envision that there are a multitude of potential slip surfaces that plausibly accommodate slip over the width of the fault zone.

6.2 Low Velocity Zone and Shallow Slip Deficit

6.2.1 Evidence of Post-Seismic Slip

Direct mesoscopic observations constrain the dimensions and nature of the SAF at the Elizabeth Lake site. Historical documents recorded during the construction of the Elizabeth Lake Tunnel indicate that

"[the granite across the entire valley, ~3/4 mi, was]… sheared with fair regularity into vertical leaves of variable thickness, with the fractures showing some slight degree of openness" (Mullholland, 1918).

A recent interpretation of the as-built tunnel descriptions indicates the presence of a zone ~900 m wide of pervasively altered and damaged rocks, and open fluid pathways, which we correlate to our rocks as the down-dip equivalent of the primary fault strand (Sutherland et al., 2014). A terrestrial laser scan study of the Elizabeth Lake Tunnel and a study of post 1857-seismic slip (Tayyebi et al., 2017) indicates a right lateral horizontal offset of ~14 cm (~1.4 mm/yr) near the projected intersection of the SAF and the tunnel. The accommodation of this post-seismic slip may have occurred in a relatively short time period after the 1857 Fort Tejon

earthquake, or as steady-state creep over the past ~100 years (Tayyebi et al., 2017). The textural characteristics of our rocks, while not constrained to the last earthquake cycle, are compatible with a component of aseismic slip accommodation, such as the aligned phyllosilicates within damaged rocks, cataclasites, gouge zones, and the abundance of slip surfaces observed in the core. The mineralogic banding within mechanically sheared cataclasites allows for co/post-seismic relaxation and grain shifting in the form of brittle flow. Our data span ~170 m and characterize the rocks within the highly damaged and altered zone in the historical documents (Mullholland 1918; Sutherland et al., 2014). The deformation and alteration features documented in this project may reasonably describe the fault processes functioning within a zone ~900 m wide across the valley.

6.2.2 Low Seismic Velocities

A low seismic velocity zone (LVZ) has been observed as enveloping fault zones (Li et al., 2003, 2007; Unsworth and Bedrosian, 2004; Cochran et al., 2009; Zoback et al., 2010; Jeppson et al., 2010; Allam and Ben Zion, 2012). These zones may comprise zones up to 1-2 km thick around the principal fault surface(s) (Spudich and Olsen, 2001; Cochran et al., 2009) and to 7 km deep (Li et al., 2007) with the effects diminishing with greater distance and depth. The sustained damage of faults may produce the low velocity zones through a variety of processes including increasing the fracture density, inducing mineral alterations, and increasing the pore fluid pressures (Schulz and Evans, 1998; Unsworth and Bedrosian, 2004; Isaacs et al., 2008; Zoback et al., 2010; Jeppson and Tobin, 2015) which can reduce seismic velocities by up to 40 to 60% (Cochran et al., 2009, Allam and Ben Zion 2012). The fault damage zone at Elizabeth Lake exhibits low seismic velocities throughout the fault zone complex with V_p values in the 2.7 – 3.5

km/sec range (LADWP Final Report 2019), well below the 3.5 – 4.0 km/sec values observed in the rocks adjacent to the SAF (Moos and Zoback, 1983) and the 5.0 – 5.5 km/sec values of protolith in the area (Hickman et al., 1988). Our observations of low velocity mineral replacements, the high density of sustained damage through wide spread fractures and shear zones, and the observed fluid-flow in the Elizabeth Lake Tunnel compliment these geophysical data acquired and provide reasonable sources for the seismic velocity reductions. The presence of LVZs may significantly affect the amount of seismic energy that is constrained within the fault zone (Harris and Day, 1997) or radiated into the far-field (Roten et al., 2017) and thus may change the dynamics of stress building and slip propagation and accommodation through the crust. The lower velocity minerals and deformation textures identified in this work comprise a pervasive and distributed damage zone that could generate the commonly observed low velocity zone in the shallow crust.

6.2.3 Shallow Slip Deficit

The shallow slip deficits postulated in strike slip faults (Dolan and Haravitch, 2014 and references therein) coincide with low velocity zones as both features are recognized as most prominent in the ~3-5 km depth range (Fialko et al., 2005; Allam and Ben Zion, 2012; Scott et al., 2019). We suggest that the geochemical signatures, deformation microstructures, and alteration textures we document here lead to the development of a fault low velocity zone and could also be used to make inferences about the observed shallow slip deficit. At the Elizabeth Lake site, the regional exhumation is estimated around ~2 km in the past 40 Ma (Spotila et al., 2002) and the rocks in this study may reasonably describe some of the microstructural characteristics and processes which contribute to the low velocity zone and the formation and recovery of the

shallow slip deficit. The shallow slip deficit has been attributed to plastic deformation near the surface (Kaneko and Fialko, 2011; Roten et al., 2017) and may be facilitated by the increased proportion of fractures, voids, and pores, the lower coefficient of friction (Dolan and Haravitch, 2014) and the prevalence of velocity strengthening behaviors in the upper crust (Kaneko and Fialko, 2011; Roten et al., 2017). Seismic waves travel slower in more damaged rocks and while estimates of slip deficits along mature faults are scarce, the presence of pre-existing damage zones are expected to increase the slip deficit (Kaneko and Fialko, 2011). If increasingly damaged rocks increase the slip deficit, then without post-seismic recovery and fault zone healing processes, the uppermost 3-5 km would become uncoupled from the seismogenic zone over multiple earthquake cycles. This slip must be accounted for over the course of seismic activity as shallow aseismic processes. At the Elizabeth Lake site, we propose that some of the post-seismic recovery may be facilitated through aseismic slip along the weak basal cleavages of aligned phyllosilicates, as volumetric changes resulting from mineral alterations and precipitations, or as shallow plasticity within weak mineral structures.

Some workers (Xu et al., 2016; Marchandon et al., 2021) indicate that shallow slip deficits may be artefacts of the data distribution and inversion schemes used to determine how slip is distributed with depth, and that many aspects of resolving the issues regarding shallow slip deficits can only be resolved with better understanding of processes within fault zones. Future work could investigate the relationship between healed damaged rocks and their relationship to the formation and accommodation of the slip deficit. An analysis of the authigenic clays within the gouge would help us understand more about the heat generated within the shallow fault zone, as well as better constrain some of the permeability and mechanical properties of the gouge.

The shallow San Andreas Fault at the Elizabeth Lake site is a zone of distributed deformation. Our work establishes a baseline of rock characteristics for the next deformation event. We identified geochemical and deformational processes which we interpret as having been active throughout the onset of seismic activity to the present. We infer that these processes characterize the low velocity zone enveloping the SAF here and contain within the rocks evidence for post-seismic slip recovery and for processes active throughout the seismic cycle and seismic history.

6.3 Conclusions

In this project, we identified the style and nature of the deformation and alteration active within the shallow San Andreas Fault at the Elizabeth Lake site through a range of mesoscopic, microscopic and geochemical methods. We show that the fault zone consists of a complex of superimposed fault strands which recycle and rework fault-related products and likely distribute the seismically generated energy throughout the fault damage zone. Earthquake related energy is distributed predominantly through brittle, and partially through plastic deformation processes and fluid-assisted mineral alteration. We found evidence of coseismic processes in the form of pseudotachylyte, clay-clast aggregates, and injection veins. We identified microstructures and petrographic relationships which may be the result of aseismic processes in the shallow crust including mechanically twined calcite veins, volumetric changes in mineral precipitations, and aligned phyllosilicates. Our microstructural and geochemical analyses support a model for the fault zone of distributed volume of deformation facilitated by a network of interlinked primary, secondary, and subsidiary faults within the shallow crust at the Elizabeth Lake site.

The deformation mechanisms and alteration textures documented in this project depict a complex interplay of brittle and semi-brittle processes and geochemical alterations active within the shallow crust. Their impact upon the fault zone properties include: 1) Decreasing the seismic velocities through the increased proportion of faults, fractures, pores, and lower velocity minerals; 2) Reducing the overall strength of the fault-related rocks through deformation-related decreases in cohesion and the alteration and replacement of stronger minerals; and 3) Distributing the earthquake-related energy over the volume of the fault damage zone rocks. We conclude that these observations of fault zone processes within the uppermost 2-3 km of the crust may contribute to both the formation, and the recovery of the hypothesized shallow slip deficit. Distributing the proportion of coseismic slip across a multitude of smaller fractures could disperse or fractionate the rupture-generated slip as it propagates to the surface and lead to an evidenced slip deficit if the off-fault volume of deformation is not adequately accounted for. The slip recovery may then also be accounted for through volumetric changes during mineral alteration, replacement, and precipitation or through semi-plastic to plastic mineral deformations within this same volume of rock. The deformation mechanisms and alteration textures we document here directly describe the shallow ~170 m wide inner damage zone of the SAF main fault strand within the ~900 m deformed and altered fault-related valley. These processes and observations illustrate the microstructural and geochemical properties of the SAF at Elizabeth Lake and are critical to the accuracy of seismic modelling of faults within the crust.

7. REFERENCES

Allam, A.A., and Ben-Zion, Y., 2012, Seismic velocity structures in the southern California plate-boundary environment from double-difference tomography: Geophysical Journal International, v. 190, p. 1181–1196, doi:10.1111/j.1365-246X.2012.05544.x.

Ault, A.K., Jensen, J.L., McDermott, R.G., Shen, F.A., and Van Devener, B.R., 2019, Nanoscale evidence for temperature-induced transient rheology and postseismic fault healing: Geology, v. 47, p. 1203–1207, doi:10.1130/G46317.1.

Ault, A.K., Reiners, P.W., Evans, J.P., and Thomson, S.N., 2015, Linking hematite (U-Th)/He dating with the microtextural record of seismicity in the Wasatch fault damage zone, Utah: Geology, v. 43, p. 771-774, doi: 10.1130/G36897.1.

Behnsen, J., and Faulkner, D.R., 2012, The effect of mineralogy and effective normal stress on frictional strength of sheet silicates: Journal of Structural Geology, v. 42, p. 49–61, doi:10.1016/j.jsg.2012.06.015.

Bemis, S.P., Scharer, K., and Dolan, J.F., 2021, The San Andreas Fault paleoseismic record at Elizabeth Lake: Why are there fewer surface-rupturing earthquakes on the Mojave Section?: Bulletin of the Seismological Society of America, p. 1-24, doi:10.1785/0120200218.

Ben-Zion, Y., and Sammis, C.G., 2013, Shear heating during distributed fracturing and pulverization of rocks: Geology, v. 41, p. 139–142, doi:10.1130/G33665.1.

Ben-Zion, Y., and Sammis, C.G., 2003, Characterization of Fault Zones: Pure and Applied Geophysics, v. 160, p. 677–715, papers2://publication/uuid/B5D8E702-ED12-48C9-8586-FCDDE3DC3A6C.

Ben-Zion, Y., and Shi, Z., 2005, Dynamic rupture on a material interface with spontaneous generation of plastic strain in the bulk: Earth and Planetary Science Letters, v. 236, p. 486–496, doi:10.1016/j.epsl.2005.03.025.

Blenkinsop, T.G., and Sibson, R.H., 1992, Aseismic fracturing and cataclasis involving reaction softening within core material from the Cajon Pass drill hole: Journal of Geophysical Research, v. 97, p. 5135–5144, doi:10.1029/90JB02285.

Boles, J.R., Coombs, D.S., 1977, Zeolite facies alteration of sandstones in the Southland Syncline, New Zealand: American Journal of Science, v. 277, p. 982-1012, doi:10.2475/ajs.277.8.982.

Bons, P.D., Elburg, M.A., and Gomez-Rivas, E., 2012, A review of the formation of tectonic veins and their microstructures: Journal of Structural Geology, v. 43, p. 33–62, doi:10.1016/j.jsg.2012.07.005.

Borg, I., and Handin, J., 1966, Experimental deformation of crystalline rocks: Tectonophysics, v. 3, p. 249–367, doi:10.1016/0040-1951(66)90019-9.

Boutareaud, S., Boullier, A.-M., Andréani, M., Calugaru, D.-G., Beck, P., Song, S.-R., and Shimamoto, T., 2010, Clay clast aggregates in gouges: New textural evidence for seismic faulting: Journal of Geophysical Research, v. 115, p. 1–15, doi:10.1029/2008jb006254.

Boutareaud, S., Calugaru, D.G., Han, R., Fabbri, O., Mizoguchi, K., Tsutsumi, A., and Shimamoto, T., 2008, Clay-clast aggregates: A new textural evidence for seismic fault sliding? Geophysical Research Letters, v. 35, p. 1–5, doi:10.1029/2007GL032554.

Bürgmann, R., 2018, The geophysics, geology and mechanics of slow fault slip: Earth and Planetary Science Letters, v. 495, p. 112–134, doi:10.1016/j.epsl.2018.04.062.

Buscher, J.T., and Spotila, J.A., 2007, Near-field response to transpression along the southern San Andreas fault, based on exhumation of the northern San Gabriel Mountains, southern California: Tectonics, v. 26, p. 1–15, doi:10.1029/2006TC002017.

Caine, J.S., Evans, J.P., and Forster, C.B., 1996, Fault zone architecture and permeability structure: Geology, v. 24, p. 1025–1028, https://pubs.geoscienceworld.org/gsa/geology/article-pdf/24/11/1025/3516124/i0091-7613-24-11-1025.pdf.

Carpenter, B.M., Saffer, D.M., and Marone, C., 2012, Frictional properties and sliding stability of the San Andreas fault from deep drill core: Geology, v. 40, p. 759–762, doi:10.1130/G33007.1.

Chen, B., Xu, B., Li, B., Kong, M., Wang, W., and Chen, H., 2020, Understanding the performance of hydraulically fractured wells in the laumontite-rich tight glutenite formation: Journal of Petroleum Science and Engineering, v. 185, p. 106600, doi:10.1016/j.petrol.2019.106600.

Chester, F.M., Evans, J.P., and Biegel, R.L., 1993, Internal structure and weakening mechanisms of the San Andreas Fault: Journal of Geophysical Research, v. 98, p. 771–786, doi:10.1029/92JB01866.

Chester, F.M., and Logan, J.M., 1986, Implications for mechanical properties of brittle faults from observations of the punchbowl fault zone, California.: Pure and Applied Geophysics, v. 124, p. 79–106, doi:https://doi.org/10.1007/BF00875720.

Cochran, E.S., Li, Y.-G., Shearer, P.M., Barbot, S., Fialko, Y., and Vidale, J.E., 2009, Seismic and geodetic evidence for extensive, long-lived fault damage zones: Geology, v. 37, p. 315–318, doi:10.1130/g25306a.1.

Collettini, C., Tesei, T., Scuderi, M.M., Carpenter, B.M., and Viti, C., 2019, Beyond Byerlee friction, weak faults and implications for slip behavior: Earth and Planetary Science Letters, v. 519, p. 245–263, doi:10.1016/j.epsl.2019.05.011.

Collettini, C., Niemeijer, A., Viti, C., and Marone, C., 2009, Fault zone fabric and fault weakness: Nature, v. 462, p. 907–910, doi:10.1038/nature08585.

Cowan, D.S., 1999, Do faults preserve a record of seismic slip? A field geologist's opinion: Journal of Structural Geology, v. 21, p. 995–1001.

Crouch, K., Evans, J.P., Studnicky, C., 2019, Fault core anlaysis of the upper seismic-aseismic transition zone in the western San Grabriel Fault, California: Abstract 554092 presented at 2019 Fall Meeting, AGU, San Francisco, California, 9-13 December.

De Bresser, J.H.P., and Spiers, C.J., 1997, Strength characteristics of the r, f, and c slip systems in calcite: Tectonophysics, v. 272, p. 1–23, doi:10.1016/S0040-1951(96)00273-9.

Deer, R.A., Howie, W.A., Wise, W.S. and Zussman, J., 2004, Framework silicates: Silica Minerals, Feldspathoids and the Zeolites: in Rock Forming Minerals, Volume 4B, eds. 2. The Geological Society, London.

Demets, C., Gordon, R.G., Argus, D.F., and Stein, S., 1994, Effect of Recent Revisions to the Geomagnetic Reversal Time-Scale on Estimates of Current Plate Motions: Geophysical Research Letters, v. 21, p. 2191–2194. https://doi.org/10.1029/94GL02118.

Dibblee, T. W., & Minch, J., 2002, Geologic map of the Valyermo quadrangle, Los Angeles County, California. Dibblee Geological Foundation. Retrieved from https://ngmdb.usgs.gov/Prodesc/proddesc_71715.htm

Doan, M.L., and Gary, G., 2009, Rock pulverization at high strain rate near the San Andreas Fault: Nature Geoscience, v. 2, p. 709–712, doi:10.1038/NGEO640==.

Dolan, J.F., and Haravitch, B.D., 2014, How well do surface slip measurements track slip at depth in large strike-slip earthquakes? The importance of fault structural maturity in controlling on-fault slip versus off-fault surface deformation: Earth and Planetary Science Letters, v. 388, p. 38–47, doi:10.1016/j.epsl.2013.11.043.

Dor, O., Ben-Zion, Y., Rockwell, T.K., and Brune, J., 2006, Pulverized rocks in the Mojave section of the San Andreas Fault Zone: Earth and Planetary Science Letters, v. 245, p. 642–654, doi:10.1016/j.epsl.2006.03.034.

Evans, J.P., 1988, Deformation mechanisms in granitic rocks at shallow crustal levels: Journal of Structural Geology, v. 1o, p. 437–443.

Evans, J.P., 1990, Textures, deformation mechanisms, and the role of fluids in the cataclastic deformation of granitic rocks: Geological Society Special Publication, v. 54, p. 29–39, doi:10.1144/GSL.SP.1990.054.01.03.

Faulkner, D.R., Jackson, C.A.L., Lunn, R.J., Schlische, R.W., Shipton, Z.K., Wibberley, C.A.J., and Withjack, M.O., 2010, A review of recent developments concerning the structure, mechanics and fluid flow properties of fault zones: Journal of Structural Geology, v. 32, p. 1557–1575, doi:10.1016/j.jsg.2010.06.009.

Faulkner, D.R., Lewis, A.C., and Rutter, E.H., 2003, On the internal structure and mechanics of large strike-slip fault zones: Field observations of the Carboneras fault in southeastern Spain: Tectonophysics, v. 367, p. 235–251, doi:10.1016/S0040-1951(03)00134-3.

Faulkner, D.R., Mitchell, T.M., Jensen, E., and Cembrano, J., 2011, Scaling of fault damage zones with displacement and the implications for fault growth processes: Journal of Geophysical Research: Solid Earth, v. 116, p. 1–11, doi:10.1029/2010JB007788.

Ferrill, D.A., Morris, A.P., Evans, M.A., Burkhard, M., Groshong, R.H., and Onasch, C.M., 2004, Calcite twin morphology: A low-temperature deformation geothermometer: Journal of Structural Geology, v. 26, p. 1521–1529, doi:10.1016/j.jsg.2003.11.028.

Fialko, Y., Sandwell, D., Simons, M., and Rosen, P., 2005, Three-dimensional deformation caused by the Bam, Iran, earthquake and the origin of shallow slip deficit: Nature, v. 435, p. 295–299, doi:10.1038/nature03425.

Forand, D., Evans, J.P., Janecke, S.U., and Jacobs, J., 2017, Insights into fault processes and the geometry of the San Andreas fault system: Analysis of core from the deep drill hole at

Cajon Pass, California: Bulletin of the Geological Society of America, v. 130, p. 64–92, doi:10.1130/B31681.1.

Forster, C., and Smith, L., 1989, The influence of groundwater flow on thermal regimes in mountainous terrain: a model study: Journal of Geophysical Research, v. 94, p. 9439–9451, doi:10.1029/JB094iB07p09439.

Fuis, G.S. et al., 2017, Subsurface geometry of the San Andreas Fault in southern California: Results from the salton seismic imaging project (SSIP) and strong ground motion expectations: Bulletin of the Seismological Society of America, v. 107, p. 1642–1662, doi:10.1785/0120160309.

Fuis, G.S., Scheirer, D.S., Langenheim, V.E., and Kohler, M.D., 2012, A new perspective on the Geometry of the San Andreas fault in southern California and its relationship to Lithospheric structure: Bulletin of the Seismological Society of America, v. 102, p. 236–251, doi:10.1785/0120110041.

Griffith, W.A., Mitchell, T.M., Renner, J., and Di Toro, G., 2012, Coseismic damage and softening of fault rocks at seismogenic depths: Earth and Planetary Science Letters, v. 353–354, p. 219–230, doi:10.1016/j.epsl.2012.08.013.

Han, R., and Hirose, T., 2012, Clay-clast aggregates in fault gouge: An unequivocal indicator of seismic faulting at shallow depths? Journal of Structural Geology, v. 43, p. 92–99, doi:10.1016/j.jsg.2012.07.008.

Harris, R.A., and Abrahamson, N.A., 2014, Strong ground motions generated by earthquakes on creeping faults: Geophysical Research Letters, p. 3870–3875, doi:10.1002/2014GL060228.

Harris, R.A., and Day, S.M., 1977, Effects of a low-velocity zone on a dynamic rupture, bulletin of the Seismological Society of America, 87, p. 1267-1280.

Hauksson, E., and Meier, M.A., 2019, Applying depth distribution of seismicity to determine thermo-mechanical properties of the seismogenic crust in southern California: Comparing Lithotectonic Blocks: Pure and Applied Geophysics, v. 176, p. 1061–1081, doi:10.1007/s00024-018-1981-z.

Hernandez, J.L., 2011, Preliminary Geologic Map of the Lake Hughes 7.5’ Quadrangle, Los Angeles County, California. California Geologic Survey.

Hickman, H., Zoback, M.D., and Healy, J.H., 1988, Continuation of a deep borehole stress measurement profile near the San Andreas Fault 1. Hydraulic fracturing stress measurements at Hi vista Mojave Desert, California: Journal of Geodynamics, v. 93, p. 15,183-15,195, doi:10.1029/JB093iB12p15183.

Holdsworth, R.E., van Diggelen, E.W.E., Spiers, C.J., de Bresser, J.H.P., Walker, R.J., and Bowen, L., 2011, Fault rocks from the SAFOD core samples: Implications for weakening at shallow depths along the San Andreas Fault, California: Journal of Structural Geology, v. 33, p. 132–144, doi:10.1016/j.jsg.2010.11.010.

Holdsworth, R.E., 2004, Weak Faults - Rotten Cores: Science, v. 303, p. 181–182, doi:10.1126/science.1092491.

Ikari, M.J., Saffer, D.M., and Marone, C., 2009, Frictional and hydrologic properties of clay-rich fault gouge: Journal of Geophysical Research: Solid Earth, v. 114, p. 1–18, doi:10.1029/2008JB006089.

Isaacs, A.J., Evans, J.P., Kolesar, P.T., and Nohara, T., 2008, Composition, microstructures, and petrophysics of the Mozumi fault, Japan: In situ analyses of fault zone properties and structure in sedimentary rocks from shallow crustal levels: Journal of Geophysical Research: Solid Earth, v. 113, p. 1–17, doi:10.1029/2007JB005314.

Jacobs, J.R., Evans, J.P, and Kolesar, P.T., 2006, Chemical alteration in fault zones as sinks for "missing" earthquake energy: in R. Abercrombie, H. Kanamori, and G. di Toro, eds., AGU Monograph on Earthquake Energy, p. 181-192. doi:10.1029/170GM18.

James, E.W., and Silver, L.T., 1988, Implications of Zeolites and Their Zonation in the Cajon Pass Deep Drillhole: Geophysical Research Letters, v. 15, p. 973–976.

Janecke, S.U., and Evans, J.P., 1988, Feldspar-influenced rock rheologies: Geology, v. 16, p. 1064–1067, doi:10.1130/0091-7613.

Jeppson, T.N., Bradbury, K.K., and Evans, J.P., 2010, Geophysical properties within the San Andreas Fault Zone at the San Andreas Fault Observatory at Depth and their relationships to rock properties and fault zone structure: Journal of Geophysical Research, v. 115, p. 1–20, doi:10.1029/2010JB007563.

Jeppson, T.N., and Tobin, H.J., 2015, San Andres fault zone velocity structure at SAFOD at core, log and seismic scales: Journal of Geophysical Research, v. 120, p. 4983–4997, doi:10.1002/2015JB012043.

Jolivet, R., and Frank, W.B., 2020, The transient and intermittent nature of slow slip: AGU Advances, v. 1, doi:10.1029/2019av000126.

Jones, L.M., Bernknopf, R., Cox, D., Goltz, J., Hudnut, K., Mileti, D., Perry, S., Ponti, D., Porter, K., Reichle, M., Seligson, H., Shoaf, K., Treiman, J., and Wein, A., 2008, The ShakeOut Scenario: U.S. Geological Survey Open- File Report 2008-1150 and California Geological Survey Preliminary Report 25 [http://pubs.usgs.gov/of/2008/1150/].

Jové, C., and Hacker, B.R., 1997, Experimental investigation of laumontite → wairakite + H_2O: A model diagenetic reaction: American Mineralogist, v. 82, p. 781–789, doi:10.2138/am-1997-7-817.

Julia, F., Vladimir, L., Sergey, R., and David, Z., 2014, Effects of hydrothermal alterations on physical and mechanical properties of rocks in the Kuril-Kamchatka island arc: Engineering Geology, v. 183, p. 80–95, doi:10.1016/j.enggeo.2014.10.011.

Kamei, R., Nakata, N., and Lumley, D., 2015, Introduction to microseismic source mechanisms: The Leading Edge, v. 34, p. 876–880, doi:10.1190/tle34080876.1.

Kanamori, H., and Rivera, L., 2006, Energy partitioning during an earthquake: Geophysical Monograph Series, v. 170, p. 3–13, doi:10.1029/170GM03.

Kanamori, H., 1994, Mechanics of Earthquakes: Annual Review of Earth and Planetary Science, 22, p. 207-237, https://doi.org/10.1146/annurev.ea.22.050194.001231

Kaneko, Y., and Fialko, Y., 2011, Shallow slip deficit due to large strike-slip earthquakes in dynamic rupture simulations with elasto-plastic off-fault response: Geophysical Journal International, v. 186, p. 1389–1403, doi:10.1111/j.1365-246X.2011.05117.x.

Kim, Y.S., Peacock, D.C.P., and Sanderson, D.J., 2004, Fault damage zones: Journal of Structural Geology, v. 26, p. 503–517, doi:10.1016/j.jsg.2003.08.002.

Kirkpatrick, J.D., Dobson, K.J., Mark, D.F., Shipton, Z.K., Brodsky, E.E., and Stuart, F.M., 2012, The depth of pseudotachylyte formation from detailed thermochronology and constraints on coseismic stress drop variability: Journal of Geophysical Research: Solid Earth, v. 117, p. 1–13, doi:10.1029/2011JB008846.

Kirkpatrick, J.D., Rowe, C.D., White, J.C., and Brodsky, E.E., 2013, Silica gel formation during fault slip: Evidence from the rock record: Geology, v. 41, p. 1015–1018, doi:10.1130/G34483.1.

Kirkpatrick, J.D., and Rowe, C.D., 2013, Disappearing ink: How pseudotachylytes are lost from the rock record: Journal of Structural Geology, v. 52, p. 183–198, doi:10.1016/j.jsg.2013.03.003.

Kirkpatrick, J.D., Shipton, Z.K., and Persano, C., 2009, Pseudotachylytes: Rarely generated, rarely preserved, or rarely reported? Bulletin of the Seismological Society of America, v. 99, p. 382–388, doi:10.1785/0120080114.

Knipe, R.J., 1980, Distribution of impurities in deformed quartz and its implications for deformation studies: Tectonophysics, v. 64, doi:10.1016/0040-1951(80)90255-3.

Lachenbruch, A.H., Sass, J.H., and Galanis, S.P., 1985, Heat flow in southernmost California and the origin of the Salton Trough: Journal of Geophysical Research, v. 90, p. 6709–2736, doi:10.1029/jb090ib08p06709.

Lachenbruch, A.H., 1986, Simple models for the estimation and measurement of frictional heating by an earthquake: doi:https://doi.org/10.3133/ofr86508.

LADWP, 2019, San Andreas Fault characterization (phase 2): Technical report, Los Angeles Department of Water and Power, https://doi.org/10.17605/OSF.IO/2VN6X.

Li, H., Zhu, L., and Yang, H., 2007, High-resolution structures of the Landers fault zone inferred from aftershock waveform data: Geophysical Journal International, v. 171, p. 1295–1307, doi:10.1111/j.1365-246X.2007.03608.x.

Li, Y., Vidale, J.E., Day, S.M., Oglesby, D.D., and Cochran, E., 2003, Postseismic fault healing on the rupture zone of the 1999 M 7.1 Hector Mine, California Earthquake: Bulletin of the Geological Society of America, v. 93, p. 854–869.

Lin, A., 1996, Injection veins of crushing-originated pseudotachylyte and fault gouge formed during seismic faulting: Engineering Geology, p. 213–224, doi:10.1016/S0165-1250(97)80012-0.

Lockner, D.A., Morrow, C., Moore, D., and Hickman, S., 2011, Low strength of deep San Andreas Fault gouge from SAFOD core: Nature, v. 472, p. 82–86, doi:10.1038/nature09927.

Marchandon, M., Hollingsworth, J., and Radiguet, M., 2021, Origin of the shallow slip deficit on a strike slip fault: Influence of elastic structure, topography, data coverage, and noise: Earth and Planetary Science Letters, v. 554, p. 116696, doi:10.1016/j.epsl.2020.116696.

Marone, C.J., Scholtz, C.., and Bilham, R., 1991, On the mechanics of earthquake afterslip: Journal of Geophysical Research, v. 96, p. 8441–8452.

Marone, C., and Saffer, D.M., 2007, Fault friction and the upper transition from seismic to aseismic faulting, in Dixon, T.H., and Moore, J.C., eds., The seismogenic zone of subduction thrust faults: New York, Columbia University Press, p. 346–369.

McDermott, R.G., Ault, A.K., Evans, J.P., and Reiners, P.W., 2017, Thermochronometric and textural evidence for seismicity via asperity flash heating on exhumed hematite fault mirrors, Wasatch fault zone, UT, USA: Earth and Planetary Science Letters, v. 471, p. 85–93, doi:10.1016/j.epsl.2017.04.020.

Minghe, J., Jianchun, L., Xiaofeng, L., and Jian, Z., 2019, Fracture surface morphology of brittle geomaterials influenced by loading rate and grain size: International Journal of Impact Engineering, v. 133, doi:10.1016/j.ijimpeng.2019.103363.

Mitchell, T.M., Ben-Zion, Y., and Shimamoto, T., 2011, Pulverized fault rocks and damage asymmetry along the Arima-Takatsuki Tectonic Line, Japan: Earth and Planetary Science Letters, v. 308, p. 284–297, doi:10.1016/j.epsl.2011.04.023.

Mitchell, T.M., and Faulkner, D.R., 2009, The nature and origin of off-fault damage surrounding strike-slip fault zones with a wide range of displacements: A field study from the Atacama fault system, northern Chile: Journal of Structural Geology, v. 31, p. 802–816, doi:10.1016/j.jsg.2009.05.002.

Moos, D., and Zoback, M.D., 1983, In situ studies of velocity in fractured crystalline rocks.: Journal of Geophysical Research, v. 88, p. 2345–2358, doi:10.1029/JB088iB03p02345.

Morrow, C.A., and Byerlee, J.D., 1991, A note on the frictional strength of laumontite from Cajon Pass, California: Geophysical Research Letters, v. 18, p. 211–214.

Morrow, C., and Byerlee, J., 1988, Permeability of Rock Samples for Cajon Pass, California: Geophysical Research Letters, v. 15, p. 1033–1036.

Mulholland, W., 1918, Earthquakes in their relation to the Los Angeles Aqueduct: Bulletin Seismological Society of America, v. 8, p. 13-19.

Ngo, D., Huang, Y., Rosakis, A., Griffith, W.A., and Pollard, D., 2012, Off-fault tensile cracks: A link between geological fault observations, lab experiments, and dynamic rupture models: Journal of Geophysical Research: Solid Earth, v. 117, p. 1–19, doi:10.1029/2011JB008577.

Niemeijer, A.R., and Spiers, C.J., 2005, Influence of phyllosilicates on fault strength in the brittle-ductile transition: Insights from rock analogue experiments: Geological Society Special Publication, v. 245, p. 303–327, doi:10.1144/GSL.SP.2005.245.01.15.

Niemeijer, A., Di Toro, G., Griffith, A.W., Bistacchi, A., Smith, S.A.F., and Nielsen, S., 2012, Inferring earthquake physics and chemistry using an integrated field and laboratory approach: Journal of Structural Geology, v. 39, p. 2–36, doi:10.1016/j.jsg.2012.02.018.

Phillips, N.J., Rowe, C.D., and Ujiie, K., 2019, For how long are pseudotachylytes strong? Rapid alteration of basalt-hosted pseudotachylytes from a shallow subduction complex: Earth and Planetary Science Letters, v. 518, p. 108–115, doi:10.1016/j.epsl.2019.04.033.

Poley, C.M., Lindh, A.G., Bakun, W.H., and Schulz, S.S., 1987, Temporal changes in microseismicity and creep near Parkfield, California: Nature, v. 327, p. 134–137, doi:10.1038/327134a0.

Proctor, B.P., Mitchell, T.M., Hirth, G., Goldsby, D., Zorzi, F., Platt, J.D., and Toro, G. Di, 2014, Dynamic weakening of serpentinite gouges and bare surfaces at seismic slip rates: Journal of Geophysical Research: Solid Earth, p. 8107–8131, doi:10.1002/2014JB011057.

Rempe, M., Mitchell, T., Renner, J., Nippress, S., Ben-Zion, Y., and Rockwell, T., 2013, Damage and seismic velocity structure of pulverized rocks near the San Andreas Fault: Journal of Geophysical Research: Solid Earth, v. 118, p. 2813–2831, doi:10.1002/jgrb.50184.

Rempel, A.W., and Rice, J.R., 2006, Thermal pressurization and onset of melting in fault zones: Journal of Geophysical Research, v. 111, p. 1–18, doi:10.1029/2006JB004314.

Rice, J.R., 1993, Spatio-temporal complexity of slip on a fault rate: Journal of Geophysical Research, v. 98, p. 9885–9907.

Rice, J.R., 2006, Heating and weakening of faults during earthquake slip: Journal of Geophysical Research, v. 111, p. 1–29, doi:10.1029/2005JB004006.

Richard, J., Gratier, J.-P., Doan, M.L., Boullier, A.-M., and Renard, F., 2014, Rock and mineral transformations in a fault zone leading to permanent creep: Interactions between brittle and viscous mechanisms in the San Andreas Fault: Journal of Geophysical Research, Solid Earth, v. 119, p. 8132–8153, doi:10.1002/2014JB011489.

Ross, D. C., 1984 Possible Correlations of basement rocks across the San Andreas, San Gregorio-Hosgri, and Rinconada-Reliz-King City Faults, California: U.S. Geological Survey Professional Paper 1317.

Roten, D., Olsen, K.B., and Day, S.M., 2017, Off-fault deformations and shallow slip deficit from dynamic rupture simulations with fault zone plasticity: Geophysical Research Letters, v. 44, p. 7733–7742, doi:10.1002/2017GL074323.

Rowe, C.D., and Griffith, W.A., 2015, Do faults preserve a record of seismic slip: A second opinion: Journal of Structural Geology, v. 78, p. 1–26, doi:10.1016/j.jsg.2015.06.006.

Rowe, C.D., Kirkpatrick, J.D., and Brodsky, E.E., 2012, Fault rock injections record paleo-earthquakes: Earth and Planetary Science Letters, v. 335–336, p. 154–166, doi:10.1016/j.epsl.2012.04.015.

Ryder, I., and Bürgmann, R., 2008, Spatial variations in slip deficit on the central San Andreas Fault from InSAR: Geophysical Journal International, v. 175, p. 837–852, doi:10.1111/j.1365-246X.2008.03938.x.

Savage, H.M., and Brodsky, E.E., 2011, Collateral damage: Evolution with displacement of fracture distribution and secondary fault strands in fault damage zones: Journal of Geophysical Research, v. 116, doi:10.1029/2010JB007665.

Schleicher, A.M., van der Pluijm, B.A., and Warr, L.N., 2012, Chlorite-smectite clay minerals and fault behavior: New evidence from the San Andreas Fault Observatory at Depth (SAFOD) core: Lithosphere, v. 4, p. 209–220, doi:10.1130/L158.1.

Schleicher, A.M., van der Pluijm, B.A., and Warr, L.N., 2010, Nanocoatings of clay and creep of the San Andreas fault at Parkfield, California: Geology, v. 38, p. 667–670, doi:10.1130/G31091.1.

Schleicher, A.M., Van Der Pluijm, B.A., Solum, J.G., and Warr, L.N., 2006, Origin and significance of clay-coated fractures in mudrock fragments of the SAFOD borehole (Parkfield, California): Geophysical Research Letters, v. 33, p. 1–5, doi:10.1029/2006GL026505.

Scholz, C.H., 2019, The mechanics of earthquakes and faulting: Cambridge, Cambridge University Press, doi:10.1017/9781316681473.

Schulz, S.E., and Evans, J.P., 1998, Spatial variability in microscopic deformation and composition of the Punchbowl fault, southern California: Implications for mechanisms, fluid-rock interaction, and fault morphology: Tectonophysics, v. 295, p. 223–244, doi:10.1016/S0040-1951(98)00122-X.

Scott, C., Champenois, J., Klinger, Y., Nissen, E., Maruyama, T., Chiba, T., and Arrowsmith, R., 2019, The 2016 M7 Kumamoto, Japan, earthquake slip field derived from a joint inversion of differential Lidar topography, optical correlation, and InSAR surface displacements: Geophysical Research Letters, v. 46, p. 6341–6351, doi:10.1029/2019GL082202.

Scharer, K., and Streig, A., 2019, The San Andreas Fault system: Complexities along a major transform fault system and relation to earthquake hazards, in Duarte, J.C., ed., Transform Plate Boundaries and Fracture Zone: Elsevier, p. 249–269, https://doi.org/10.1016/B978-0-12-812064-4.00010-4.

Scharer, K.M., and Yule, D., 2020, A maximum rupture model for the southern San Andreas and San Jacinto Faults, California, derived from paleoseismic earthquake ages: observations and limitations: Geophysical Research Letters, v. 47, doi:10.1029/2020GL088532.

Sharp, R.P., 1952, Physiographic features of faulting in southern California: California Division of Mines Geology, Bulletin 170, pp 21-28.

Shipton, Z.K., Soden, A.M., Kirkpatrick, J.D., Bright, A.M., and Lunn, R.J., 2006, How thick is a fault? Fault displacement-thickness scaling revisited: Earthquakes, v. 170, p. 193–198, doi:10.1029/170GM19.

Sibson, R.H., 1977, Fault rocks and fault mechanisms: Journal of the Geological Society of London, v. 133, p. 191–213, doi:10.1144/gsjgs.133.3.0191.

Sibson, R.H., 1986, Earthquakes and rock deformation in crustal fault zones.: Annual Review of Earth and Planetary Sciences. Vol. 14, p. 149–175, doi:10.1146/annurev.earth.14.1.149.

Sibson, R.H., 1973, Interactions between temperature and pore-fluid pressure during earthquake faulting and a mechanism for partial or total stress relief: Nature Physical Science, v. 243, p. 66–68, doi:10.1038/physci243066a0.

Sibson, R.H., 1975, Generation of pseudotachylyte by ancient seismic faulting: Geophysical Journal of the Royal Astronomical Society, v. 43, p. 775–794, doi:10.1111/j.1365-246X.1975.tb06195.x.

Simpson, C., 1986, Fabric development in brittle-to-ductile shear zones: Pure and Applied Geophysics, v. 124, p. 269-288, https://doi.org/10.1007/BF00875728.

Sohn, R.A., and Menke, W., 2002, Application of maximum likelihood and bootstrap methods to nonlinear curve-fit problems in geochemistry: Geochemistry, Geophysics, Geosystems, v. 3, p. 1–17, doi:10.1029/2001gc000253.

Spotila, J.A., House, M.A., Blythe, A.E., Niemi, N.A., and Bank, G.C., 2002, Controls on the erosion and geomorphic evolution of the San Bernardino and San Gabriel Mountains, southern California: Special Paper 365: Contributions to Crustal Evolution of the Southwestern United States, p. 205–230, doi:10.1130/0-8137-2365-5.205.

Spudich, P., and Olsen, K., 2001, Fault zone amplified waves as a possible seismic hazard along the Calaveras fault in Central California: Geophysical Research Letters, v. 28, p. 2533–2536, doi: 10.1029/2000GL011902.

Steinbrugge, K. V, and Zacher, E.G., 1960, Fault creep and property damage: Bulletin of the Seismological Society of America, v. 50, p. 389–396.

Stipp, M., Stünitz, H., Heilbronner, R., and Schmid, S.M., 2002, The eastern Tonale fault zone: A "natural laboratory" for crystal plastic deformation of quartz over a temperature range from 250 to 700 °C: Journal of Structural Geology, v. 24, p. 1861–1884, doi:10.1016/S0191-8141(02)00035-4.

Studnicky, C., Evans, J.P., and Bradbury, K.K., 2019, Insights into the properties and structure if the upper portion of the San Andreas Fault as seen from core: Poster presentation at 2019 GSA Annual Meeting, Poster 207-6, Phoenix, Arizona, 22-25 September.

Sullivan, W.A., and Peterman, E.M., 2017, Pulverized granite at the brittle-ductile transition: An example from the Kellyland fault zone, eastern Maine, U.S.A.: Journal of Structural Geology, v. 101, p. 109–123, doi:10.1016/j.jsg.2017.07.002.

Sutherland, M., Keaton, J.R., Heron, C., 2013, Correlating surface geology with 1913-vintage as-built geology across the San Andreas fault for seismic enhancement of the Elizabeth Tunnel, Los Angeles Aqueduct, Geological Society of America Abstracts with Programs. Vol. 45, No. 6, p.23.

Sutherland, M., Keaton, J. R., Heron, C. and Kuganenthira, N., 2014, Seismic enhancements for delivering water to the City of Los Angeles across the San Andreas Fault in the Elizabeth Tunnel, Geo-Congress 2014 Technical Papers, GSP 234, p. 3779-3778.

Sylvester, A.G., 1988, Strike-slip faults: Geological Society of America Bulletin, v. 100, p. 1666–1703.

Tayyebi, A., Telling, J., Hudnut, K., Davis, C. Glennie, C., 2017, 100 Years of accumulated deformation at depth observed in the Elizabeth Lake Tunnel, southern San Andreas Fault: Presentation at 2017 AGU Fall Meeting, New Orleans, LA, 11-17 December.

Torgersen, T., and Clarke, W.B., 1992, Geochemical constraints on formation fluid ages, hydrothermal heat flux, and crustal mass transport mechanisms at Cajon Pass: Journal of Geophysical Research, v. 97, p. 5031–5038, doi:10.1029/91JB01505.

Townend, J. et al., 2017, Petrophysical, geochemical, and hydrological evidence for extensive fracture-mediated fluid and heat transport in the Alpine Fault's hanging-wall damage zone: Geochemistry, Geophysics, Geosystems, v. 18, p. 4709–4732, doi:10.1002/2017GC007202.

Unsworth, M., and Bedrosian, P.A., 2004, On the geoelectric structure of major strike-slip faults and shear zones: Earth, Planets and Space, v. 56, p. 1177–1184, doi:10.1186/BF03353337.

Utada, M., 2001, Zeolites in burial diagenesis and low-grade metamorphic rocks: Reviews in Mineralogy and Geochemistry, v. 45, p. 276–304, doi:10.2138/rmg.2001.45.9.

Vernik, L., and Nur, A., 1992, Petrophysical analysis of the Cajon Pass scientific well: implications for fluid flow and seismic studies in the continental crust: Journal of Geophysical Research, v. 97, p. 5121–5134, doi:10.1029/91JB01672.

Vincent, M.W., and Ghlig, P.L., 1988, Laumontite Mineralization in Rocks Exposed North of San Andreas Fault at Cajon Pass, Southern California: Geophysical Research Letters, v. 15, p. 977–980.

Vrolijk, P., and Van Der Pluijm, B.A., 1999, Clay gouge: Journal of Structural Geology, v. 21, p. 1039–1048, doi:10.1016/S0191-8141(99)00103-0.

Wallace, R.E., 1990, The San Andreas Fault System, California: U.S. Geological Society Professional Paper 1515.

Wechsler, N., Allen, E.E., Rockwell, T.K., Girty, G., Chester, J.S., and Ben-Zion, Y., 2011, Characterization of pulverized granitoids in a shallow core along the San Andreas Fault, Littlerock, CA: Geophysical Journal International, p. 401–417, doi:10.1111/j.1365-246X.2011.05059.x.

Weisenberger, T., and Bucher, K., 2010, Zeolites in fissures of granites and gneisses of the Central Alps: Journal of Metamorphic Geology, v. 28, p. 825–847, doi:10.1111/j.1525-1314.2010.00895.x.

Weldon, R.J., Biasi, G.P., Wills, C.J., and Dawson, T.E., 2008, Appendix E: Overview of the Southern San Andreas Fault Model: USGS Open File Report, p. 1–90, papers2://publication/uuid/2D31CE15-B238-4516-B0DE-6FD4E604A45E.

Weldon, R.J., Fumal, T.E., Powers, T.J., Pezzopane, S.K., Scharer, K.M., and Hamilton, J.C., 2002, Structure and earthquake offsets on the San Andreas fault at the Wrightwood, California paleoseismic site: Bulletin of the Seismological Society of America, v. 92, p. 2704–2725, doi:10.1785/0120000612.

Wintsch, R.P., Christoffersen, R., and Kronenberg, A.K., 1995, Fluid-rock reaction weakening of fault zones: Journal of Geophysical Research, v. 100, doi:10.1029/94jb02622.

Xu, X., Tong, X., Sandwell, D.T., Milliner, C.W.D., Dolan, J.F., Hollingsworth, J., Leprince, S., and Ayoub, F., 2016, Refining the shallow slip deficit: Geophysical Journal International, v. 204, p. 1867–1886, doi:10.1093/gji/ggv563.

Ye, J., and Liu, M., 2017, How fault evolution changes strain partitioning and fault slip rates in Southern California: Results from geodynamic modeling: Journal of Geophysical Research: Solid Earth, v. 122, p. 6893–6909, doi:10.1002/2017JB014325.

Young, E.K., Scharer, K.M., Keen-Zebert, A., Anderson-Merritt, E., Cowgill, E.S., and Weldon, R.J., 2019, New interpretations at the Ranch Center and Key Slide slip rate sites, Mojave

section of the San Andreas fault: Palm Springs, California, 2019 Southern California Earthquake Center Annual Meeting, Poster #130.

Zielke, O., Arrowsmith, J.R., Ludwig, L.G., and Akciz, S.O., 2010, Slip in the 1857 and Earlier Large Earthquakes Along the Carrizo Plain, San Andreas Fault: Science, v. 327, p. 1119–1122, doi:10.1126/science.1182781.

Zoback, M., Hickman, S., and Ellsworth, W., 2010, Scientific drilling into the San Andreas Fault zone: Eos, Tranactions, American Geophysical Union, v. 91, p. 197–199, doi:10.1029/2010EO220001.

8. APPENDICES

Appendices can be found via Utah State University's Digital Commons at (Hyperlink).